Calibration of the wire positions of the ATLAS Muon Chambers and studies of Neutralino decays at LHC

Dissertation der Fakultät für Physik

der

Ludwig-Maximilians-Universität München

vorgelegt von

Sofia Chouridou

aus

Thessaloniki, Griechenland

München, den 22. Februar 2002

1. Gutachter: Prof. Dr. D. Schaile
2. Gutachter: Prof. Dr. M. Faessler

Tag der mündlichen Prüfung: 22. Mai 2002

Calibration of the wire positions of the ATLAS Muon Chambers and studies of Neutralino decays at LHC

Dissertation der Fakultät für Physik

der

Ludwig-Maximilians-Universität München

vorgelegt von

Sofia Chouridou

aus

Thessaloniki, Griechenland

München, den 22. Februar 2002

$T\acute{\alpha}\quad \pi\grave{\alpha}\nu\tau\alpha\ \overset{c}{\varrho}\epsilon\tilde{\iota}.$

$^c H\varrho\acute{\alpha}\kappa\lambda\epsilon\iota\tau o\varsigma\ (535-475\ \pi.X).$

Everything is in an unceasing process of eternal flux.

Heraklitos (535-475 BC).

To my mother, Matenia
and the memory of my father, Themistoklis

Abstract

ATLAS is a general-purpose detector that is being built for the Large Hadron Collider (LHC) at CERN. The precision tracking devices of the ATLAS Muon Spectrometer are high pressure Monitored Drift Tube (MDT) chambers. The LHC physics discovery potential sets stringent requirements on the performance of these chambers. They should be able to achieve a momentum resolution of $\sim 10\%$ for muons with a transverse momentum of $p_T = 1$ TeV. In order to accomplish this goal, the MDT chambers should be constructed with 20 μm mechanical accuracy (r.m.s of the relative distance between the wires of the drift tubes).

The present work describes a wire calibration method for the MDT chambers, without the use of any external reference system. The success of the method in finding wire displacements in the direction perpendicular to the muon tracks was verified during two test beam periods: first the displacements of 12 tubes were measured while the chamber was filled with the old baseline gas $Ar/N_2/CH_4$ (91/4/5), and later while the new baseline gas was used (Ar/CO_2 (93/7)), wire displacements of 52 tubes were calculated. The results of the method were compared with those given by the X-ray tomograph at CERN, revealing an accuracy of the method better than 10 μm.

Simulation studies of the application of the method along the full width of a chamber, were performed and were focussed on its systematic and statistical effects. It turned out that even when Gaussian distributed time offsets of 200 and 300 ps are added to the drift time spectra of the tubes, the local uncertainty remains in the order of 10 μm. By combining the local information for the wire displacements the absolute wire positions within the whole chamber with respect to the first central wires within each multilayer are acquired. In this case, the global accuracy of the method is in the order of 20 μm. Moreover, considering random and uncorrelated wire displacements this accuracy improves to 10 μm.

This work also presents studies relevant to the ATLAS Supersymmetry (SUSY) discovery potential. SUSY is considered as a very motivated extension of the Standard Model by many theorists. If it exists it will lead to discoveries at LHC over most of its parameter space. Within the Minimal Supergravity Model (mSUGRA) of SUSY, five parameters are used in order to determine the masses and couplings of the particles. Six combinations of these parameters, selected by the LHC Committee and the ATLAS Collaboration for detailed studies, define representative points of the mSUGRA parameter space. The decay channel $\tilde{\chi}_2^0 \to \tilde{\chi}_1^0 l^+ l^-$ through a virtual Z* was studied at the fourth point of mSUGRA. Two versions of PYTHIA were compared by studying the differences in the invariant mass distributions of opposite-sign same-flavour lepton pairs. The newest version of the two, includes the spin-averaged matrix element in sparticle decays, thus taking into account the spin of the neutralinos and the propagator. The effect of this inclusion is profound in most of the cases while studying this specific channel in different points of the mSUGRA parameter space.

Zusammenfassung

ATLAS ist ein Universalexperiment, das für den Large Hadron Collider (LHC) am CERN gebaut wird. Hochdruckdriftrohr (MDT) Kammern werden im ATLAS Myonspektrometer zur Präzisionsmessung von Spuren verwendet. Das Entdeckungsvermögen des LHC für Physik setzt hohe Anforderungen an die Leistung dieser Kammern. Sie sollen fähig sein eine Impulsauflösung von 10% für Myonen zu erreichen, die einen Transversalimpuls von $p_T = 1$ TeV haben. Um dieses Ziel zu erreichen, sollten die MDT Kammern mit einer mechanischen Genauigkeit von 20 μm (die Standardabweichung des relativen Abstandes zwischen den Drähten der Driftrohre) gebaut werden.

Die vorliegende Arbeit beschreibt eine Kalibrationsmethode für die MDT Kammern, ohne Benutzung eines externen Referenzsystems. Der Erfolg dieser Methode im Auffinden der Drahtversetzung senkrecht zu den Myonspuren wurde während zweier Teststrahlperioden überprüft: zuerst wurden die Versetzungen von 12 Rohren gemessen während derer die Kammer mit dem alten baseline Gas $Ar/N_2/CH_4$ (91/4/5) und später mit dem neuen (Ar/CO_2 (93/7)) aufgefüllt war, die Drahtversetzungen von 52 Rohren wurden berechnet. Die Ergebnisse dieser Methode wurden mit denen des X-ray Tomograph am CERN verglichen und zeigten eine Genauigkeit besser als 10 μm.

Simulationsstudien für die Anwendung der Methode entlang der vollen Breite der Kammer wurden ausgeführt und konzentrierten sich auf die systematischen und statistischen Effekte. Es stellte sich heraus, daß auch bei Gaußisch verteilten Abweichungen des Driftzeitnullpunkts von 200 und 300 ps, die lokale Ungenauigkeit in der Größenordnung von 10 μm bleibt. Beim Vergleich der lokalen Information für die Drahtversetzungen werden die absoluten Drahtpositionen in der ganzen Kammer im Vergleich zu den ersten zentralen Drähten in jedem Multilayer benötigt. In diesem Fall ist die globale Genauigkeit der Methode in der Größenordnung vom 20 μm. Ferner, mit Rücksicht auf die zufälligen und unkorrelierten Drahtversetzungen verbessert sich die Genauigkeit zu 10 μm.

Die vorliegende Arbeit beinhaltet auch Studien zum ATLAS Supersymmetrie (SUSY) Entdeckungsvermögen. SUSY wird von vielen Theoretikern als gut motivierte Erweiterung des Standard Models angesehen. Falls SUSY existiert würde es bei LHC entdeckt werden für den größten Teil des möglichen Parameterbereichs. Im Minimalen Supergravitations Model (mSUGRA) von SUSY, werden 5 Parameter benutzt um die Massen und Kopplungen der Teilchen zu ermitteln. Sechs Kombinationen dieser Parameter definieren repräsentative Punkte des mSUGRA Parameter Raumes, die vom LHC Komitee und der ATLAS Kollaboration für detaillierte Studien ausgewählt wurden. Der Zerfallskanal $\tilde{\chi}_2^0 \rightarrow \tilde{\chi}_1^0 l^+ l^-$ durch den Austausch eines virtuellen Z* Bosons wurde untersucht am Punkt vier von mSUGRA. Zwei Versionen von PYTHIA wurden verglichen indem die Unterschiede in den invariante Masseverteilungen für Leptonpaare mit entgegengesetztem Vorzeichen und gleichem Flavour untersucht wurden. Die neuere Fassung der beiden Versionen erfasst die spin-averaged Matrixelemente in Zerfällen Supersymmetrischer Teilchen, indem der Spin des Neutralinos und des Propagators berücksichtigt wurde. In den meisten Fällen, in denen die spezifischen Kanäle in den verschiedenen Punkten des mSUGRA Parameter Raumes untersucht werden, ist ein klarer Unterschied zwischen den beiden Versionen.

Contents

Chapter 1

Introduction

For thousands of years the unceasing and curious human mind has been trying to explain the world we live in and define its basic underlying reality. The simple question 'what is the world made of?' has not been fully answered yet.

The notion that matter is made up of small, indivisible particles goes back to the ancient Greeks. The great philosopher and scientist Democritus of Abdera (460-370 BC) developed the atomic hypothesis and can be considered as the first particle physicist. According to him, the matter can be subdivided only to a certain point at which only atoms, whose tiny size can not be diminished, remain. This hypothesis is still valid but of course it has been revised and proven experimentally. It was then in 1897 when Thomson discovered the first tiny particles, the electrons, when modern particle physics was born. Since those days the particle physics domain experienced much more discoveries of new particles and their interactions. The tremendous success in science the last almost hundred years resulted in the formation of an effective theory that describes our world; the Standard Model (SM).

According to this theory the whole world is made up of three generations of elementary particles, each containing two leptons and two quarks, and twelve gauge bosons which mediate the electromagnetic, weak and strong forces. The SM has proven to be extraordinarily successful and its predictions have been tested and verified to an unprecedented precision. Nevertheless, it can not be considered to be the ultimate theory of Nature because it can not provide answers to many questions. Therefore it is a work in progress and will have to be extended to describe physics at arbitrarily high energies.

The so called Grand Unified Theories (GUT) set themselves the task to solve problems that the SM can not solve. A very motivated GUT theory is Supersymmetry (SUSY). It is a purely theoretical invention that generalizes the space-time symmetries of quantum field theory by transforming fermions into bosons and vice versa. That is, every known elementary particle has a supersymmetric partner, or superpartner, which

is like it in all respects except for its spin. Spin-$\frac{1}{2}$ fermions, leptons and quarks have spin-0 superpartners, while spin-1 bosons, like the photon, have spin-$\frac{1}{2}$ superpartners. But SUSY is not an exact symmetry of nature, otherwise the superpartners would have the same mass as their partners and they would have been detected easily long time ago. Thus, SUSY must be a broken symmetry. There are different theoretical models that describe the breaking of SUSY and one of them is the Minimal Supergravity model (mSUGRA).

Large international collaborations are dedicated to construct the next generation of particle detectors at the Large Hadron Collider (LHC) at the European laboratory for particle physics CERN, one of the world's leading laboratories. The goal of the two (ATLAS and CMS) out of the four experiments in total at the LHC, is not only to discover the Higgs particle (the only undiscovered particle of the SM) but also to prove if Supersymmetry exists or not. If Nature has really chosen to be supersymmetric, it will be relatively easy to verify it at LHC. The masses of the superpartners are expected to be in the order of 1 TeV, thus their discovery potential at LHC, where the center-of-mass energy in the particle collisions is 14 TeV, is very large.

The subject of the present thesis is relevant to the ATLAS Experiment and more specifically to the wire calibration of the Monitored Drift Tube (MDT) Chambers of the ATLAS Muon Spectrometer and to the potential of the ATLAS detector in detecting SUSY through the next-to lightest neutralino production and decay. The neutralinos are the superpartners of the SM gauge bosons.

The thesis is structured in the following way: after this introduction, chapter 2 describes briefly the Atlas detector at the LHC and presents its physics discovery potential, as well as its requirements. Chapter 3 focuses on the description of the ATLAS Muon Spectrometer and its MDT chambers. Chapter 4 presents the quality assurance of the MDT chambers. In chapter 5, a new wire calibration method for the MDT chambers, without the use of any external reference system is presented. Chapter 6 is devoted to the simulation studies of this calibration method and reveals its statistical and systematic effects. Chapter 7 provides a short introduction to SUSY and describes the simulation studies of the next-to lightest neutralino decay at different points of the mSUGRA parameter space at the LHC, using the ATLAS detector. The last chapter, chapter 8, provides a summary of the present thesis.

Chapter 2

The ATLAS Detector:
An Experiment at the LHC

In the year 2006 the operation of the Large Hadron Collider (LHC), a powerful particle accelerator is scheduled to start.

The LHC is the next step in a voyage of discovery which began a century ago. Back then, scientists had just discovered all kinds of mysterious rays, X-rays, cathode rays, alpha and beta rays. Many questions have been answered about the origin and properties of these rays giving us a much greater understanding of the Universe. At the dawn of the 21st century, we face new questions in elementary particle physics which LHC is designed to address.

In this chapter the physics potential of the collider as well as its impact on the design of the ATLAS experiment are briefly given.

2.1   The Large Hadron Collider

The LHC will be a proton-proton collider with a center-of-mass energy $\sqrt{s}$ of 2 $\times$ 7 = 14 TeV. It will be installed in the existing 27 km of circumference tunnel at CERN in Geneva which has housed till November of 2000 the Large Electron Positron Collider (LEP). The design luminosity of LHC is 10^{34} cm^{-2} s^{-1}. Two bunches of 10^{11} protons each, will collide every 25 ns. These protons will be prepared by CERN's existing accelerator chain (see Figure 2.1) before being injected into the two LHC separate beam lines that will host the two proton beams.

The high luminosity in combination with the very high center-of-mass energy of the accelerator will allow the exploration of particle physics up to energies that dominated the universe just 10^{-12} s after the 'Big Bang' when the temperature was about 10^{16} K.

At the interaction points (four in total along the tunnel) where the two proton beams meet, the transverse bunch radius will be 15 μm and the bunch length will be 30 cm. This means that the position of the vertex will have a rather large spread along the beam direction; the effective spread of the distribution of the vertex position is expected to be 5.5 cm (r.m.s) along the beam direction.
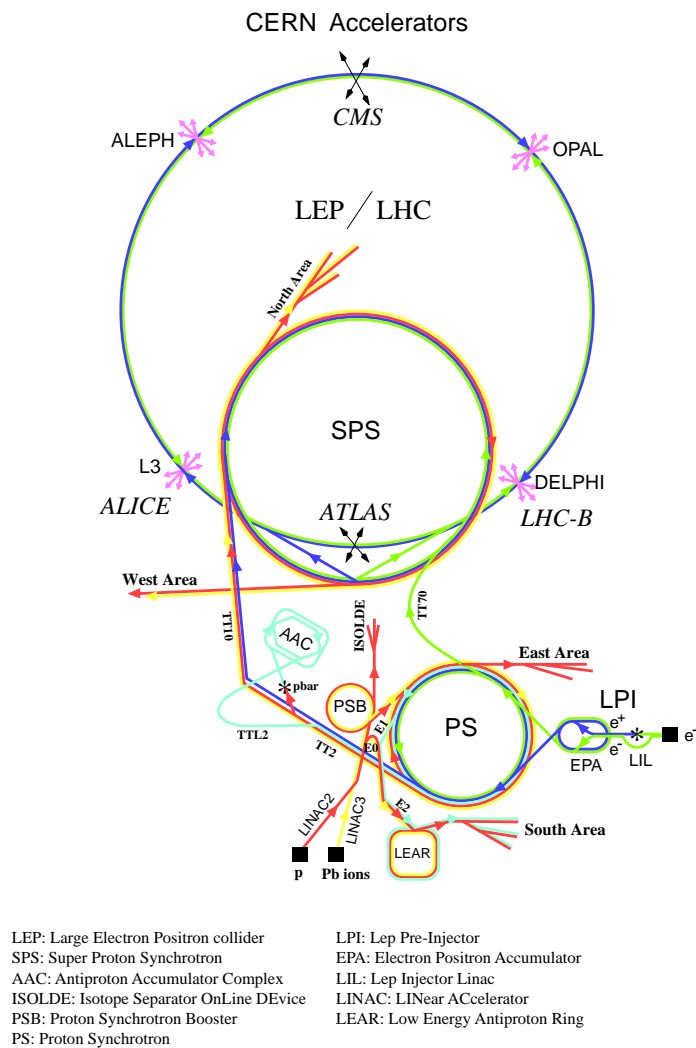
Figure 2.1: *Schematic view of the CERN accelerator complex.*

2.2 Particle Production rates

In Figure 2.2 the total proton-proton cross-section together with the production cross-sections for some characteristic processes as a function of the p-p centre-of-mass energy are shown. The total cross section is estimated to be between 90 and 130 mb. This will result in about 20 interactions per bunch crossing (i.e every 25 ns) at the design luminosity of 10^{34} cm^{-2} s^{-1}. At this luminosity the collision rate will be 10^{9} collisions per second and the total integrated luminosity is expected to be 10^{5} pb^{-1} per year.
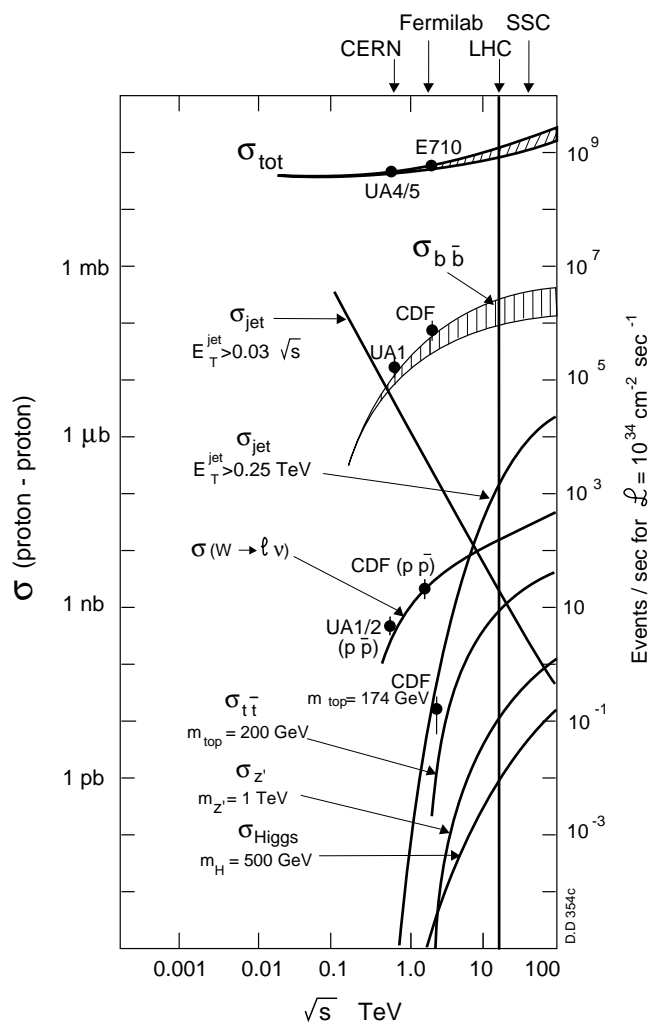
Figure 2.2: *The cross-section of some characteristic processes at LHC as a function of the p-p centre-of-mass energy [DEN90].*

2.3   Physics at LHC and Detector Requirements

One of the main goals of LHC is to study the actual mechanism of symmetry breaking in the electroweak sector ($SU(2) \times U(1)$) of the Standard Model (SM). This mechanism is associated with the Higgs Boson. Therefore the Higgs search is used as a benchmark for detector optimization.

The high energy and luminosity of the LHC offers a large range of physics opportunities, from the precise measurements of the properties of known objects to the exploration of the high energy frontier. Therefore besides the Higgs search, several other processes will be used as benchmarks for the detector design. All these examples of physics at LHC as well as the stringent detector requirements they set, are discussed in this section briefly.

2.3.1   Higgs Physics

The last unobserved particle from the Standard Model is the Higgs boson. Its discovery would allow one to complete the SM paradigm and confirm the mechanism of spontaneous symmetry breaking. On the contrary, the absence of the Higgs boson would awake doubts about the whole picture and would require new concepts. Therefore one of the main topics in LHC studies will be the search for the SM Higgs boson.

The total Higgs production cross section at LHC is predicted to range between 0.1 pb and 100 pb depending on the Higgs mass. The dominant production mechanisms are gluon-gluon fusion, WW fusion and ZZ fusion while less important production processes are $t\bar{t}$ fusion and Higgs bremsstrahlung from W or Z. Only a few decay channels of the Higgs boson are accessible to experimental observation at LHC because either the decay channels have small branching ratios or the decays are obscured by a large background of events that carry the signature of the Higgs. Hence the different Higgs decay channels, described below, for the Higgs mass ranging from 80 GeV to 1 TeV are the most prominent benchmark processes for the detectors design at LHC.

The current Higgs mass lower limit is set to 114.1 GeV. It has been derived by direct searches at LEP, which had to stop in November 2000 as the accelerator was switched off giving its place to the LHC [LEP01].

Figure 2.3 shows the branching ratios of Higgs decay channels depending on the Higgs mass:

- 80 GeV $< m_{\mathrm{H}} <$ 120 GeV:
  Below the WW or ZZ threshold the largest Higgs decay branching ratio will be H $\rightarrow$ b$\bar{\text{b}}$. Since this decay channel is obscured by QCD background, the reconstruction and tagging of b-jets with high efficiency is a crucial element in

the detector performance. Another promising channel in this mass range is H → $\gamma\gamma$ although it suffers from very large background. For such detections an electromagnetic calorimeter with high resolution and excellent photon/jet and photon/electron discrimination is required.

- 120 GeV $< m_\mathrm{H} <$ 180 GeV:
  In this mass region the decay H → ZZ* → $4l^\pm$ (where l = e, μ) provides a very clean signature. Very good lepton energy/momentum resolution is required (about 1%).

- 180 GeV $< m_\mathrm{H} <$ 800 GeV:
  The decay H → ZZ → $4l$ is considered to be the most reliable discovery channel since the expected signal rates are large and the background small.

- $m_\mathrm{H} >$ 800 GeV:
  For this heavy Higgs boson the decay H → ZZ → $l^+l^-\nu\nu$ is relevant and it is six times more frequent than the H → ZZ → $4l$. This signature is characterized by the high missing transverse energy due to the escaping neutrinos and by two charged high p_T leptons. Another promising channel in this mass range is H → W^+W^- → $l\nu jj$ (j denotes a jet).
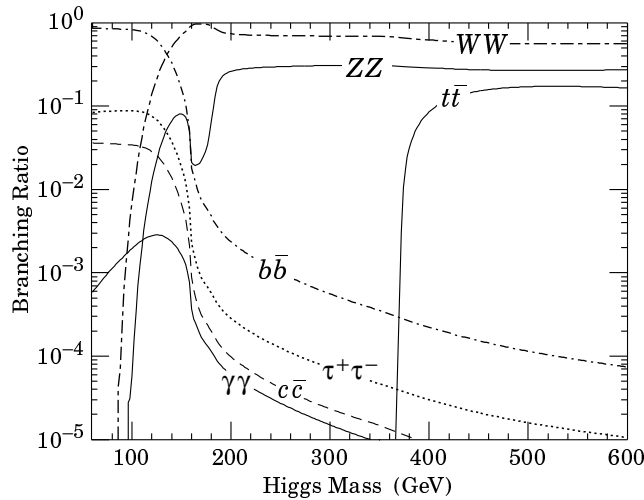

Figure 2.3: *Branching ratios of the Higgs.*

2.3.2 Super-Symmetric Particles

In the Minimal Supersymmetric extension of the SM (MSSM) there is a family of Higgs bosons: a charged boson pair($H^\pm$) and three neutral bosons (h, H^0, A). More

about this extension of the SM can be found in chapter 7. For the search of these bosons efficient secondary vertex detection for τ leptons and b quarks as well as high resolution calorimetry for jets and missing transverse energy are essential. The search of the lightest supersymmetric particle (LSP), which is stable (assuming R-parity conservation) and escapes detection, sets stringent requirements for the hermeticity and missing transverse energy of the detectors.

2.3.3   Heavy Quark Physics

An important chapter of LHC physics will be the study of heavy quark systems. Already at initial lower luminosity the LHC will be a high rate beauty and top quark factory. LHC has a great potential for performing high precision top physics measurements with about eight million $t\bar{t}$ pairs expected to be produced for an integrated luminosity of 10 fb^{-1}. It would allow not only for the precise measurement of the top quark mass (with precision of ~ 2 GeV) but also the detailed study of its properties. The main emphasis in B physics studies will be given to the precise measurement of CP-violation in the B_d^0 system and the determination of the angles in the Cabibbo-Kobayashi-Maskawa unitarity triangle. In addition, investigations of $B\bar{B}$ mixing in the B_s^0 system, rare B decays and general spectroscopy of states with b quarks will be of great interest.

Precise secondary vertex determination, full reconstruction of final states with relatively low-p_T particles and low-p_T lepton first level trigger as well as second level track triggering capability are necessary requirements for the LHC experiments.

2.3.4   Other Searches

Maybe Nature has not chosen the Higgs mechanism as the mechanism responsible for the electroweak symmetry breaking. Therefore at LHC searches for signatures of technicolor models, which could replace the Higgs bosons of the SM or MSSM, will be performed.

There are also other possibilities for new physics that are not necessarily related to the scale of electroweak symmetry breaking. There could be for example new neutral or charged gauge bosons with masses larger than those of the Z and W bosons. Several extensions of the Standard Model postulate the existence of such heavy gauge bosons (Z' and W'). They could be accessible at LHC for masses up to 5-6 TeV. Considering their leptonic decays, high resolution lepton measurements and charge identification are needed even in a p_T range up to a few TeV.

The LHC experiments finally will also be able to perform new physics searches for leptoquarks, quark and lepton compositeness, magnetic monopoles and massive neutrinos.

2.4 Detectors for the LHC

To exploit the full discovery potential of LHC two general-purpose proton-proton experiments (ATLAS and CMS) and two specialised experiments (ALICE and LHCb) will be installed at the beam crossings.

ATLAS

The ATLAS (**A T**oroidal **L**HC **A**pparatu**S**) detector has a characteristic magnet configuration: a) a super-conducting solenoid will be installed around the Inner Detector cavity and b) large super-conducting air-core toroids consisting of independent coils will be arranged outside the calorimetry. This concept offers almost no constrains on calorimetry and Inner Detector allowing non-compromised technological solutions, a high-resolution, large acceptance and robust Muon Spectrometer with excellent stand-alone capabilities. The ATLAS detector is going to be 22 m high, 44 m long and have a weight of about 6000 tons.

The subject of this thesis is focussed on this detector. In the next section a more detailed description of this experiment will be given.

CMS

The main difference between the CMS (**C**ompact **M**uon **S**olenoid) and the ATLAS detectors lies in their magnet configurations for muon spectroscopy. The CMS is based on a single, large and superconducting solenoidal magnet (14 m long and 3 m inner radius) generating a uniform magnetic field of 4 T. This detector is going to have a height of 14 m and a length of 20 m, whereas its weight is going to be about 12000 tons.

ALICE

ALICE (**A L**arge **I**on **C**ollider **E**xperiment) will convert the till recently existing L3 detector into a heavy-ion dedicated experiment that will investigate Pb-Pb collisions at centre-of-mass energies at the PeV scale. Its aim will be to create and study the so called Quark Gluon Plasma (QGP), the state of matter where quarks and gluons are deconfined. This state is believed to have existed shortly after the Big Bang when the temperature of the Universe was extremely high. In addition ALICE will search for qualitative and quantitative differences between proton-proton and nucleus-nucleus collisions.

LHCb

The LHCb will be dedicated to B physics and it is going to be built in the DELPHI pit. It is an open-geometry forward collider detector. The large Lorentz boost of the produced B mesons will allow precise decay time measurements, which are complemented by excellent particle identification and efficient muon triggers.

For more detailed information about the four detectors mentioned above, see the respective technical proposals of the experiments; [ATL94], [CMS94], [ALI95] and [LHCb98].

2.5   The ATLAS Detector

The ATLAS Collaboration proposes to built a general-purpose proton-proton detector which is designed to exploit the full discovery potential of the LHC. The Collaboration submitted a Letter of Intent in 1992, a Technical Proposal in 1994 and since then several Technical Design Reports (TDRs) for each subsystem including most of the final specifications have been published. The construction phase has already started for most of the detector components and the experiment is scheduled to be ready for the start of LHC in summer 2006. The overall layout of the ATLAS detector is shown in Figure 2.4.
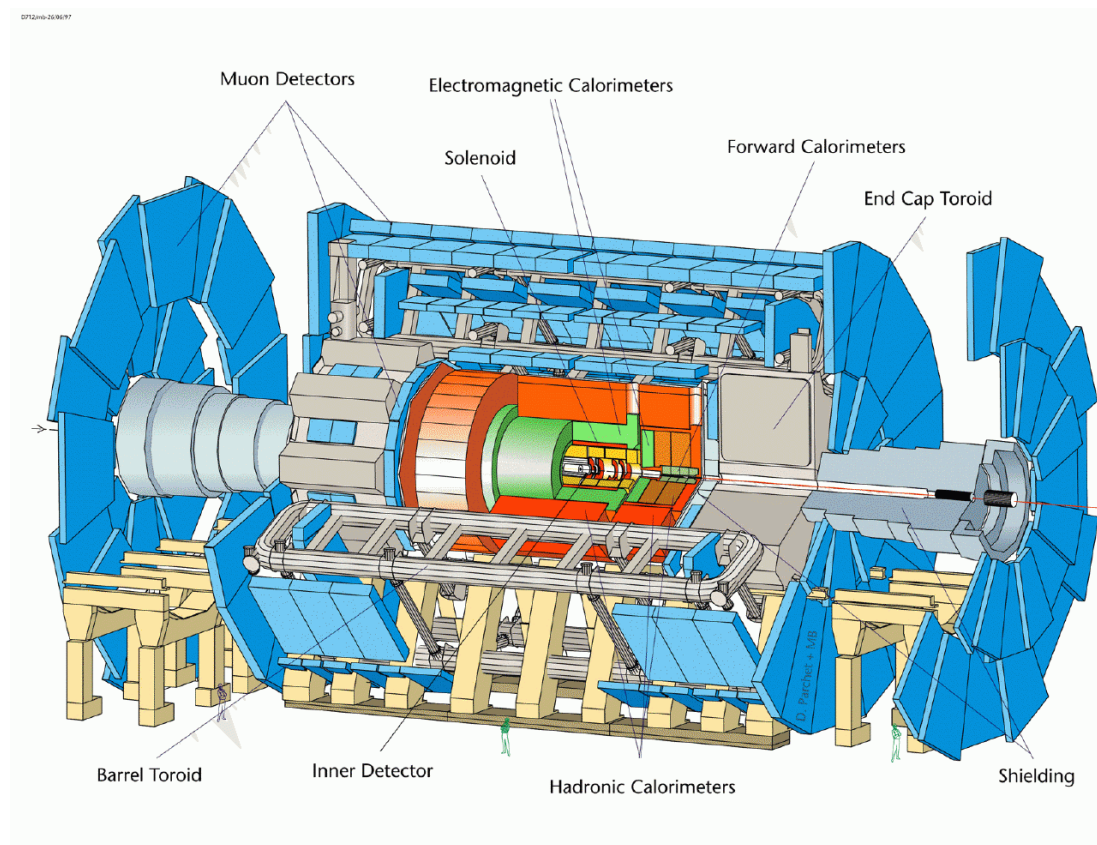

Figure 2.4: *Overall Layout of the ATLAS detector.*

The observable cross-sections for most of the processes are small over a large part of mass range. Therefore an important design consideration is to operate in high luminosity and to maximise the detectable rates above backgrounds by high-resolution measurements.

The basic design considerations are the following:

- Very good electromagnetic calorimetry for electron and photon identification and measurements, complemented by full-coverage hadronic calorimetry for accurate jet and missing transverse energy (E_T^{miss}) measurements.

- High-precision muon momentum measurements, with the capability to guarantee accurate measurements at the highest luminosity using the external muon spectrometer alone.

- Efficient tracking at high luminosity for high-p_T lepton-momentum measurements, electron and photon identification, τ-lepton and heavy-flavour identification and full event reconstruction capability at lower luminosity.

- Large acceptance in pseudorapidity (η) with almost full azimuthal angle (ϕ) coverage everywhere. The azimuthal angle is measured around the beam-axis, whereas pseudorapidity relates to the polar angle (θ) with $\eta = -\ln \tan(\theta/2)$ where θ is the angle from the z-direction (along the beam line).

- Triggering and measurements of particles at low-p_T thresholds, providing high efficiencies for most physics processes of interest at LHC.

2.5.1   The Magnet System

The ATLAS superconducting magnet system [ATLm97] is an arrangement of a central thin solenoid (CS) [ATLc97] providing the Inner Detector with magnetic field, surrounded by a system of three large air-core toroids consisting of independent coils arranged with an eight-fold symmetry that generate the magnetic field for the muon spectrometer. The overall dimensions of the magnet system are 26 m in diameter. The two end-cap toroids (ECT) [ATLe97] are inserted in the barrel toroid (BT) [ATLb97] at each end and line up with the CS. The CS provides a central field of 2 T while the three air-core toroids provide an average toroidal field of 0.5 T in the muon system. The magnets are indirectly cooled by forced flow of helium at 4.5 K through tubes welded on the casing of the windings.

2.5.2   The Inner Detector

The Inner Detector [ATLi97a] (see Figure 2.5) combines high-resolution detectors at the inner radii with continuous tracking elements at the outer radii, all contained in the Central Solenoid. The momentum and vertex resolution requirements from physics

call for high-precision measurements to be made with fine-granularity detectors, given the enormous track density expected at the LHC.
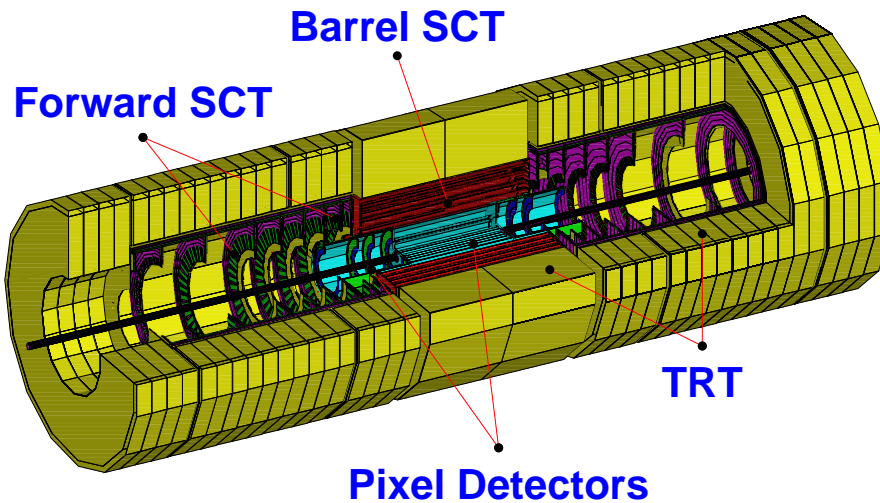
Figure 2.5: *Three-dimensional cutaway view of the ATLAS Inner Detector consisting of the Pixel Vertex Detector, the Semi Conductor Tracker (SCT) and the Transition Radiation Tracker (TRT).*

Therefore the Inner Detector consists of three parts:

- **The Pixel Vertex Detector** [ATLp98] which will provide a very high-granularity and high-precision set of measurements very close to the interaction point. The 140 millions of pixels form three barrels at average radii of 4, 10 and 13 cm and five disks on each side of the system between radii of 11 and 20 cm. The pixels should not only have tiny dimensions (50 μm $\times$ 300 μm) in order to fulfill the required task of pattern recognition in the crowded environment of the LHC but also should be radiation hardened to withstand over 300 kGy of ionising radiation and over 5 $\times$ 10^{14} neutrons per cm^2 over ten years of operation. The spatial resolution in the azimuthal direction Rϕ (the bending direction of the solenoid) will be 12 μm while along the z direction (the direction of the beam) will be 70 μm.

- **The Semi Conductor Tracker (SCT)** [ATLi97b] which will consist of silicon microstrip detectors forming four complete barrels at radial distances between 30 and 52 cm. Each silicon detector will be 6.36 $\times$ 6.40 cm^2 with 768 readout

strips of 80 μm pitch. The SCT system is designed to provide four precision measurements per track in the intermediate radial range contributing to the measurement of momentum, impact parameter and vertex position. The resolution will be 16 μm in Rϕ and 580 μm in z direction.

- **The Transition Radiation Tracker (TRT)** [ATLi97b] which will consist of straw detectors of 4 mm in diameter and equipped with a 30 μm diameter gold-plated W-Re wire. The straws will be filled with a $Xe/CF_4/CO_2$ gas mixture. The barrel region will contain about 50000 straws in axial orientation while the end-cap wheels will contain 320000 in radial orientation. Each straw channel provides a drift-time measurement (giving a resolution of 170 μm per straw) and two independent thresholds. In this way the discrimination between tracking hits, which pass the lower threshold, and transition-radiation hits, which pass also the higher one will be possible.

2.5.3 Calorimetry

The ATLAS calorimetry system [ATLcl96] is shown in Figure 2.6. It consists of an electromagnetic (EM) calorimeter covering the pseudorapidity region $|\eta| < 3.2$, a hadronic barrel calorimeter covering $|\eta| < 1.7$, hadronic end-cap calorimeters covering $1.5 < |\eta| < 3.2$ and forward calorimeters covering $3.1 < |\eta| < 4.9$.

The Electromagnetic Calorimeter (EM)

The EM Calorimeter [ATLl96] is a lead/liquid-argon (LAr) detector with accordion-shaped Kapton electrodes and lead absorber plates over its full coverage. The total thickness of the EM calorimeter is larger than 24 radiation lengths (X_0) in the barrel and larger than 26 X_0 in the end-caps. A granularity of $\Delta\eta \times \Delta\phi = 0.025 \times 0.025$ is aiming for an energy resolution of $\Delta E/E = 10\%\sqrt{E(GeV)}$ and an angular resolution of 50 mrad$\sqrt{E(GeV)}$.

The Hadronic Calorimeter

The barrel hadronic calorimeter [ATLl96, ATLt96] is a sampling calorimeter using iron as an absorber and scintillating tiles as the active material. It covers the pseudorapidity region $|\eta| < 1.7$ and extends radially from an inner radius of 2.28 m to an outer radius of 4.25 m. Over the range $1.5 < |\eta| < 4.9$, LAr calorimeters are used: the hadronic end-cap calorimeter extends to $|\eta| < 3.2$ and is a copper-LAr detector and the forward calorimeters that covers the region $3.2 < |\eta| < 4.9$ and are based on rods filled with LAr in a copper and tungsten matrix. The energy resolution of the hadronic calorimeter will be $\Delta E/E = 50\%\sqrt{E(GeV)}$ for $|\eta| < 3$ and $\Delta E/E = 100\%\sqrt{E(GeV)}$ for $3 < |\eta| < 4.9$.

ATLAS Calorimetry

EM Accordion
Calorimeters

Hadronic Tile
Calorimeters

Forward LAr
Calorimeters

Hadronic LAr End Cap
Calorimeters
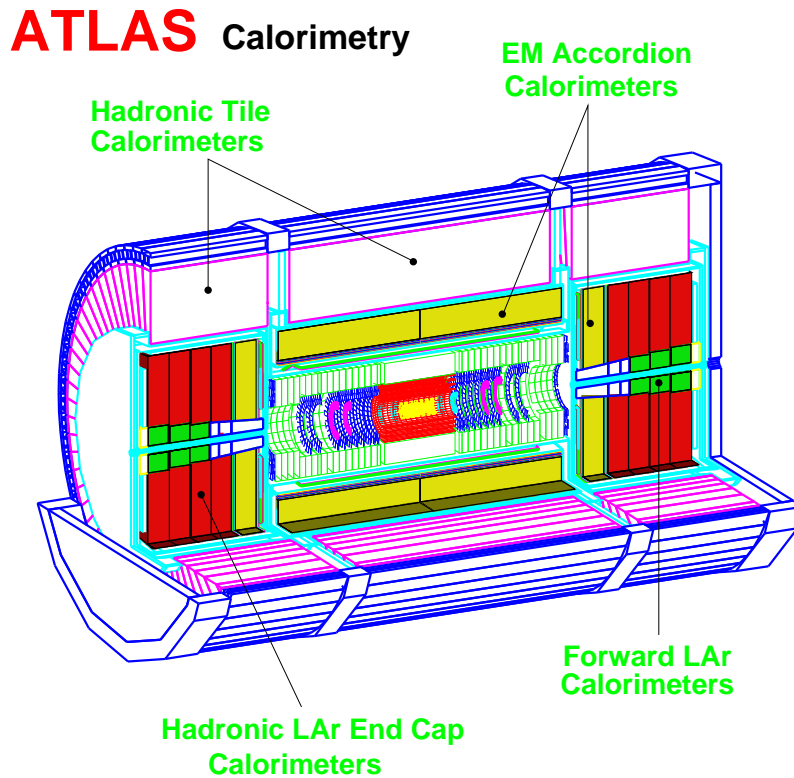
Figure 2.6: *Three-dimensional layout of the ATLAS calorimetry system.*

2.5.4   The Muon Spectrometer

The ATLAS Muon Spectrometer, the outer layer of the ATLAS detector will be described in more detail in the next chapter.

2.5.5   The ATLAS Trigger Scheme

The task of the trigger system is to identify bunch crossings that contain interesting physics events. Starting from an initial bunch-crossing rate of 40 MHz (corresponding to 10^9 collisions/s), the rate of selected events will be reduced to $\sim$ 100 Hz for permanent storage. The trigger scheme is based on three levels of online event selection:

- **The Level-1 trigger (LVL1)** makes the initial selection of interesting bunch-crossings using reduced-granularity information from a subset of detectors. The LVL1 latency (time taken to form and distribute the LVL1 decision) will be 2 μs. After the LVL1 the event rate will be reduced to 75 kHz (upgradable to 100 kHz).

- **The Level-2 trigger (LVL2)** is designed to reduce the LVL1 trigger rate to ~ 1 kHz by using full-granularity and full-precision data from most of the detectors. LVL2 processing is restricted to 'Regions of Interest'(RoI) provided by the LVL1 trigger. Its latency is variable from event to event and it is expected to be in the range 1-10 ms.

- **The Level-3 trigger (LVL3)** performs the last stage of the online selection using the full event data. Events that satisfy the final criteria are stored for off-line analysis. The output event rate is finally reduced to ~ 100 Hz.

Chapter 3

The ATLAS Muon Spectrometer

High-momentum final-state muons are amongst the most promising and robust sig-
natures of physics at the LHC. To exploit this potential, the ATLAS Collaboration has
designed a high-resolution muon spectrometer (Figure 3.1) with stand-alone triggering
and momentum measurement capability over a wide range of transverse momentum,
pseudorapidity and azimuthal angle.

The layout of the spectrometer is based on the magnetic deflection of muon tracks
in a system of three large superconducting air-core toroid magnets (Figure 3.2) (in
order to avoid resolution deterioration by multiple scattering in a massive core) instru-
mented with separate-function trigger and high-precision tracking chambers.
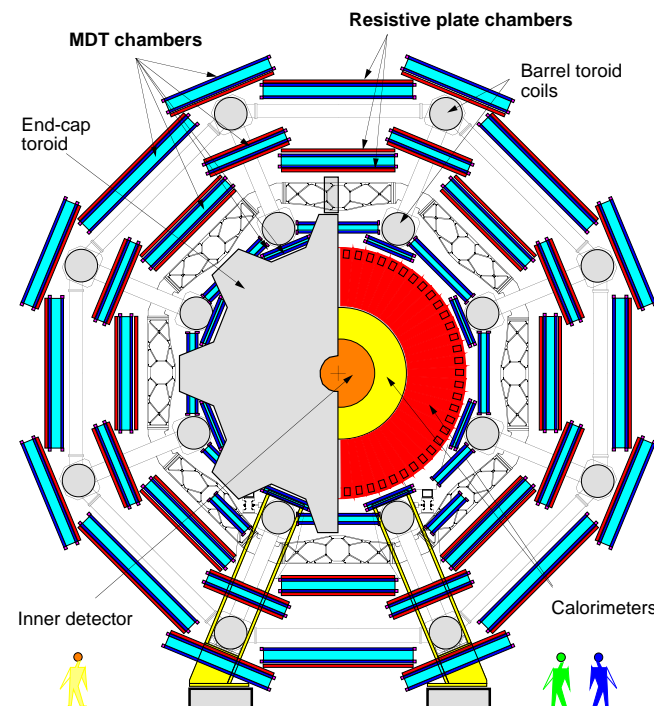
Figure 3.1: *Transverse view of the ATLAS Muon Spectrometer.*

17
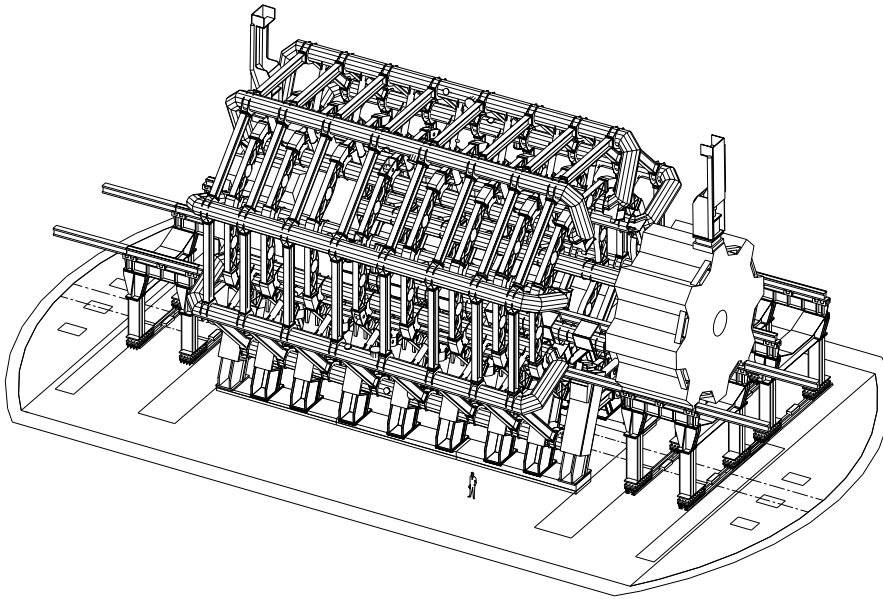
Figure 3.2: *Three-dimensional view of the superconducting air-core toroid magnet system (consisting of a barrel and two end-caps). The right-hand end-cap magnet is shown retracted from its operating position.*

In the pseudorapidity range $|\eta| \leq 1.0$, magnetic bending is provided by a large barrel magnet constructed from eight coils surrounding the hadron calorimeter. For $1.4 \leq |\eta| \leq 2.7$, muon tracks are bent in two smaller end-cap magnets inserted into both ends of the barrel toroid. In the interval $1.0 \leq |\eta| \leq 1.4$ referred to as transition region, magnetic deflection is provided by a combination of barrel and end-cap fields.

3.1 Muon Spectrometer layout

The layout of the muon chambers in the ATLAS detector can be seen in Figure 3.3 where the different regions covered by four different chamber technologies are shown. The chambers are arranged such that particles from the interaction point traverse three stations of chambers.

More specifically in the barrel region the chambers form three cylindrical layers ('stations') concentric with the beam axis. In this region the particles are measured near the inner and outer field boundaries and inside the field volume, in order to determine the momentum from the sagitta of the trajectory. The end-cap chambers are arranged

in four disks concentric with the beam axis. Over most of the pseudorapidity range, a precision measurement of the track coordinates in the principal bending direction of the magnetic field is performed by Monitored Drift Tube (MDT) chambers (see Section 3.3.2). At large pseudorapidities and close to the interaction point where the particle fluxes are very high, instead of MDTs, Cathode Strip Chambers (CSCs) are employed.
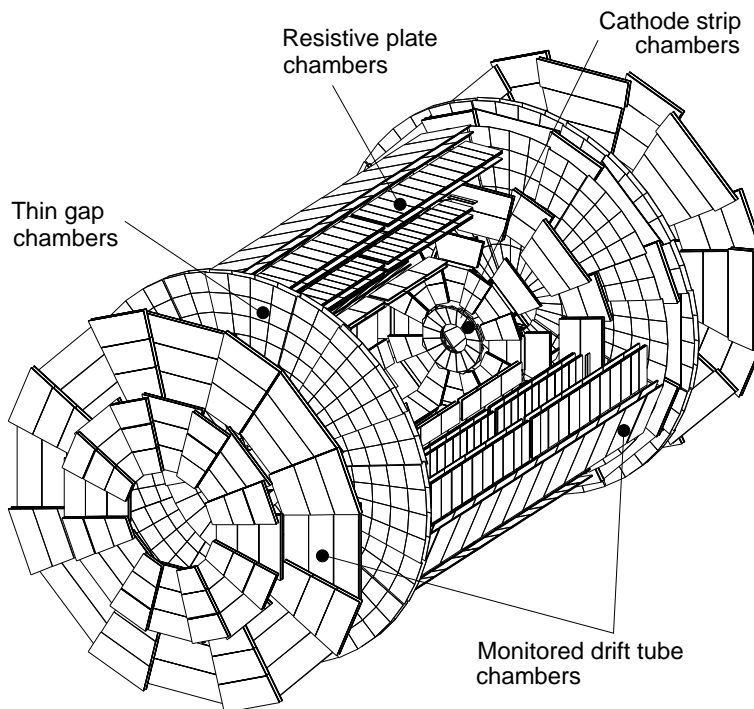
Figure 3.3: *Three-dimensional view of the muon spectrometer instrumentation indicating the areas covered by the four different chamber technologies.*

The trigger system covers the pseudorapidity range $|\eta| \leq 2.4$. In the barrel the trigger function is provided by three stations of Resistive Plate Chambers (RPCs). They are located on both sides of the middle MDT station and either directly above or directly below the outer MDT station. In the end-caps, the trigger is performed by three stations of Thin Gap Chambers (TGCs) located near the middle MDT station. Both of the RPCs and TGCs also provide the 'second coordinate' measurement of track coordinates orthogonal to the precision measurement, in a direction approximately parallel to the magnetic field lines.

3.2   Background conditions

While the particles in the Inner Detector come mainly from the primary proton-proton interaction, the particle flux in the muon spectrometer is the result from a chain of complex interactions in the calorimetry and shielding and is therefore affected by much larger uncertainties.

The high level of particle fluxes in the spectrometer plays an important role for the design of its instrumentation and defines the specifications for rate capability, granularity, ageing properties and finally radiation hardness. Trigger and reconstruction algorithms also must be carefully optimized to deal with the demanding background conditions.
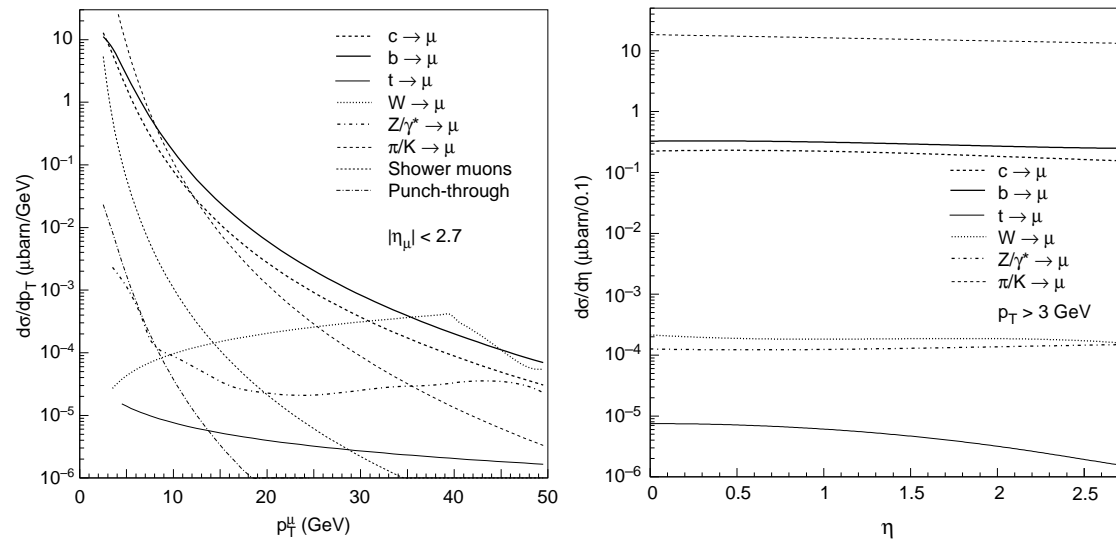
Figure 3.4: *Expected inclusive cross-section for primary collision products [CHE93]: (a) as a function of the transverse momentum p_T, integrated over $|\eta| < 2.7$ and (b) as a function of the rapidity, integrated over $3 < p_T < 50$ GeV.*

There are two categories of background sources:

1. **Primary collision products** that are correlated in time to the primary p-p collision and they penetrate into the muon spectrometer through the calorimeters. Sources of this kind of background are muons produced in the decays of:

   - heavy-flavour hadrons ($c, b, t \rightarrow \mu X$);
   - gauge bosons ($W, Z, \gamma^* \rightarrow \mu X$);
   - light hadrons in flight ($h \rightarrow \mu X$) in the inner tracker cavity;
   - hadronic debris produced in the calorimeter showers (shower muons),

and finally a small fraction of hadrons interacting late or not at all in the calorimeters and therefore penetrate into the muon spectrometer (hadron punch-through) (Figure 3.4a).

Muons with momentum less than about 3 GeV will not reach the muon chambers. For transverse momenta $p_T > 10$ GeV the inclusive muon cross-section is dominated by charm and beauty decays. At larger $p_T > 30$ GeV, top and Z decays also give a sizeable contribution. If we compare though the prompt-muon (i.e. correlated in time to the primary p-p collision) and hadronic components that reach the muon chambers, we reach the conclusion that the calorimeter system has enough absorptive power to suppress hadronic debris well below the irreducible level of the prompt muons. The total counting rate from primary collision products is dominated by low-p_T pion and kaon decays in the inner tracker cavity (Figure 3.4b)

2. **Radiation background**, which consists mostly of low-energy (1 MeV) neutrons and photons and is produced by secondary interactions in the forward calorimeter, shielding material, the beam pipe and machine elements (Figure 3.5a). This kind of background due to frequent rescattering is not any longer correlated in time to the primary p-p interaction. Although the photon and neutron sensitivities of the MDTs are only 0.45% and 0.1% respectively [BAR94, CHL93], counting rates up to 100 Hz/cm^2 are expected (Figure 3.5b).
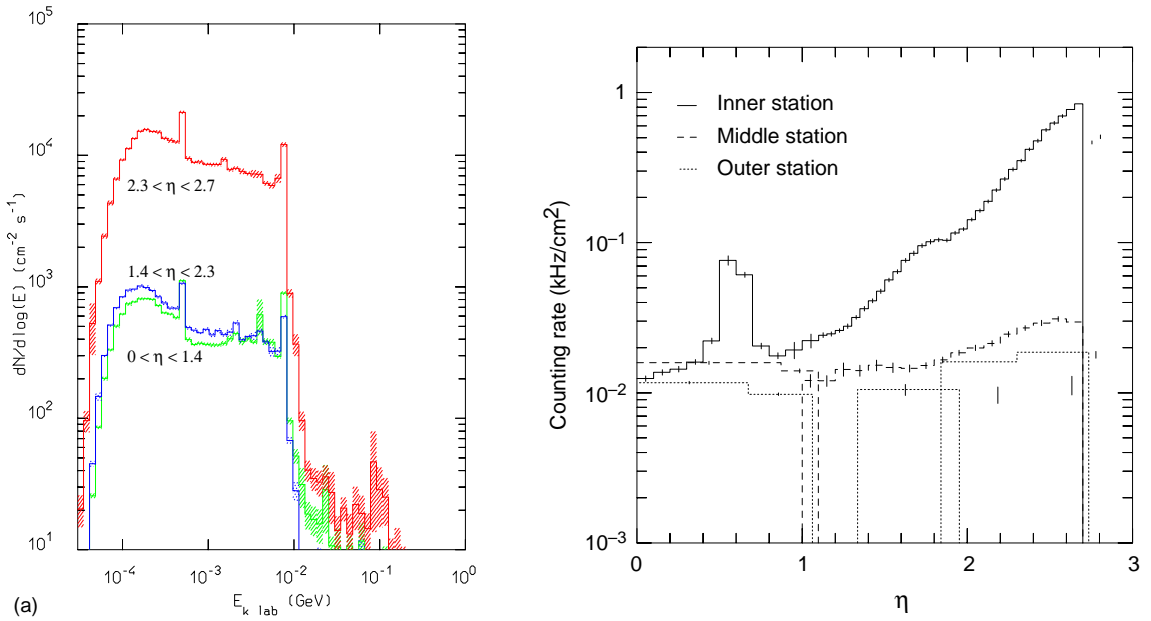

Figure 3.5: *(a) The expected photon flux as a function of photon energy in different pseudorapidity regions of the spectrometer, (b) pseudorapidity dependence of the total counting rate in the three precision chamber stations.*

The ATLAS collaboration decided to design the muon system for a five times higher background than expected as the background rates have an uncertainty of a factor five due to the superposition of different contributions: First there are the uncertainties of the total p-p cross-section and of the multiplicity produced in the primary collisions (factor 1.3). Furthermore the chamber sensitivities are uncertain by a factor up to 1.5. And lastly the limited knowledge of the showering processes in the absorber and of the (n, γ) cross-sections and the ensuing neutron and photon production has been assumed to contribute by a factor 2.5. However, recent work [GSC00] has shown that this uncertainty resulting from the shower processes can be reduced to a factor 1.2.

The effects of the high-rate radiation background on drift chamber operation were studied at a test-beam experiment with a strong gamma source [DEI00].

3.3   Muon Precision Drift Chambers

Over most of the pseudorapidity range of the muon spectrometer the technology of the Monitored Drift Tube Chambers (MDT) is used as precision chambers (see also [HES98]). The muon momenta in the spectrometer will be reconstructed from a measurement of the sagitta in three muon precision-chamber stations. To achieve the required momentum resolution at high momenta (the sagitta for a 1 TeV muon is about 500 μm) the muon instrumentation has to provide a position measurement accuracy of about 50 μm per station.

In this section we describe in some detail this kind of chambers starting with their constituents.

3.3.1   Description and Operation Principle of the Single Drift Tube

The basic detection elements of the MDT chambers are cylindrical aluminium drift tubes with a diameter of 3 cm and 400 μm wall thickness having a central W-Re sense wire of 50 μm diameter that is connected to positive high voltage. The tubes are operated with non-flammable gas mixture at 3 bar absolute pressure and are closed at both ends by end-plugs. These end-plugs provide the fixation of the central wire and its electrical contact. They also contain the gas seals for each tube as well as the gas connectors to the gas manifold. The tube lengths vary from 1 to 6 m.

The principle of operation is shown in Figure 3.6. When a muon traverses a drift tube, it interacts electromagnetically causing ionization of the detector gas and producing clusters of electrons along its track. Since the collisions with the gas atoms are random, the number of ionization clusters per unit of track length is Poisson distributed
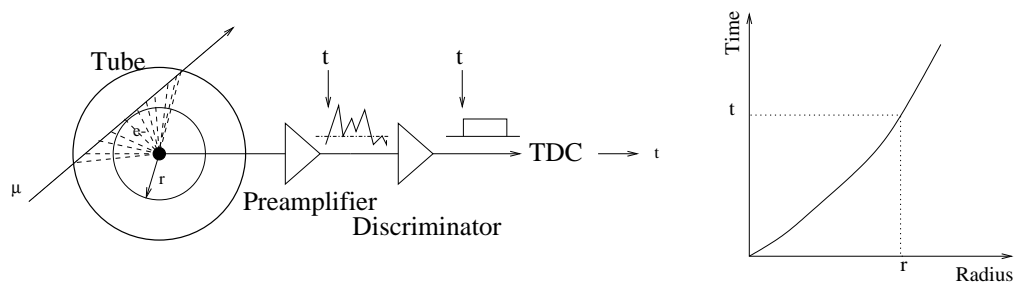
Figure 3.6: *Principle of the Single Tube Operation. The electron drift time is measured and converted to a distance via a space-time relationship (rt-relation).*

[BLU94]. An effective description of the ionization left by the charged particle along its trajectory is provided by the so called cluster-size distribution (the number of electrons in a ionization cluster). In Figure 3.7 the cluster-size distribution for $Ar/N_2/CH_4$ (91/4/5) simulated with HEED [SMI97] is presented [RIE97]. HEED is a program that computes in detail the energy loss of fast charged particles in gases. If we ignore clusters above 500 electrons the mean number of electrons per cluster is about 3.
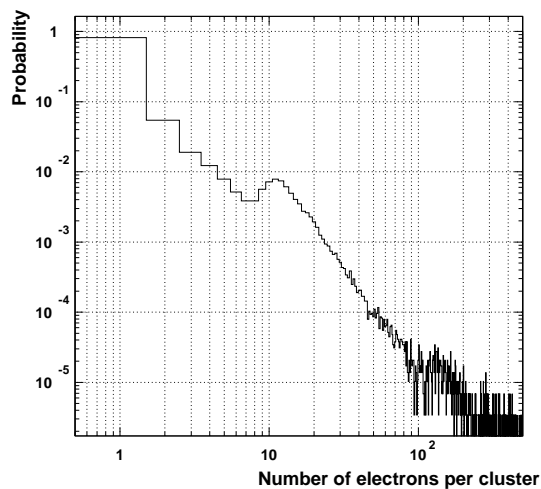
Figure 3.7: *Cluster-size distribution for $Ar/N_2/CH_4$ (91/4/5) at 3 bar absolute pressure simulated with HEED.*

The clusters of electrons produced along the trajectory of the muon, drift towards the anode wire guided by the radial electric field

$$E(r) = \frac{V}{r \, ln\frac{b}{a}} \quad , \tag{3.1}$$

where *a* is the wire radius, *b* the inner cathode radius and *V* the high voltage applied to the anode. As the charge approaches the wire, it is multiplied in an avalanche process creating new electron-ion pairs [SAU77]. The anode voltage is chosen such that the avalanche amplification factor (gas gain) is 2×10^4. Typically this voltage is about 3 kV. The positive ion cloud moves from the avalanche zone towards the cathode, inducing a current signal in the anode wire, which is read out on the side of the tube, amplified, shaped and presented finally to a discriminator. The drifting electrons also induce a signal which is though negligible compared to the ion signal. The logical output pulse of the discriminator is given to a Time-to-Digital-Converter (TDC) which measures the time difference between the muon pulse and a trigger signal. This time difference is the drift time of the electrons plus a constant offset due to the signal propagation time in the electronics. Subsequently the drift time is converted into the radius (r) of closest approach of the track using the space-time relationship (r-t relationship or rt relation) obtained by an autocalibration procedure [CRE97, DEI00, VIE96]. According to the ATLAS specifications the single-tube spatial resolution should be 80 μm or better. The detailed analysis of the contributions to the spatial resolution that can be obtained with such a drift tube is discussed in [RIE97].

3.3.2 Monitored Drift Tube Chambers (MDTs)

The MDT chambers consist of two multilayers of tubes glued on either side of a rigid spacer structure (Figure 3.8).
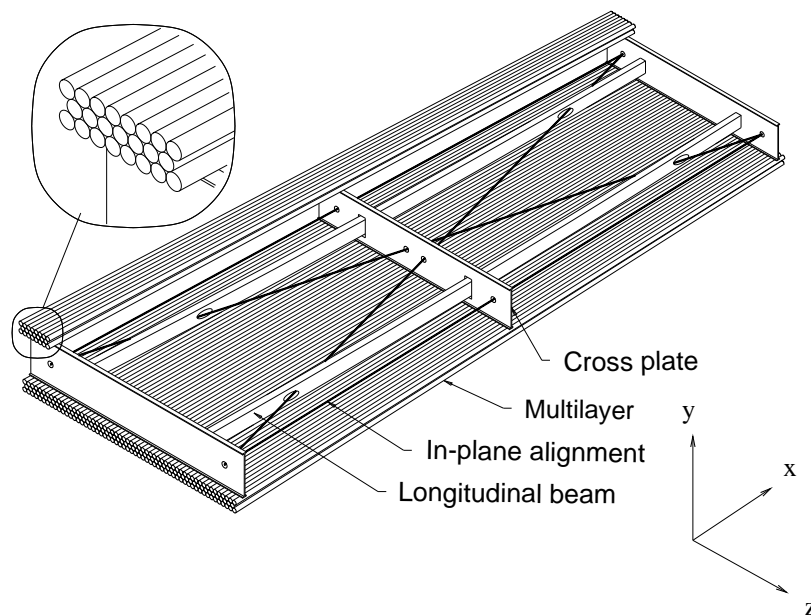

Figure 3.8: *An MDT chamber consists of three (as shown in the figure) or four layers of aluminum tubes which are glued on either side of the spacer structure.*

The multilayers of the chambers in the middle and outer station have three layers of tubes while those of the chambers in the inner station have four layers in order to make the pattern recognition in these high background regions more reliable. The support frame (consisted of three cross-plates and two long beams) provide the positioning of the two multilayers with respect to each other and mechanical integrity under effects of temperature change and gravity. It also supports most of the components of the alignment system (see section 3.5).

The accurate positioning of the drift tubes is provided by the assembly procedure. The tubes are glued together after positioning. This chamber assembly and construction design was chosen for guaranteeing the reliability and the stability of the construction and operation for the anticipated lifetime of the experiment in an irradiated environment: 5 years of storage followed by final assembly and 10 years of running.

Depending on their sizes and position in the muon spectrometer, there are several kinds of MDT Chambers such as BOS (Barrel Outer Small), BOL (Barrel Outer Large), BIS (Barrel Inner Small) etc.

The MDT project is on the scale of a very large industrial project. The task in numbers is impressive: the total number of MDTs is 1194 covering an area of 5500 m^2 while the total number of readout channels is 371488 and the total length of the tubes is 1141 km. The chambers will be built in 16 Institutes spread over the world with CERN coordination and control. A Quality Assurance Plan was established (see chapter 4).

3.4 Muon Spectrometer Performance Requirements

A comparison between most spectrometers in high energy physics experiments to date and the ATLAS muon spectrometer yields that the latter is unique in several aspects. It is designed to maintain high performance in terms of momentum resolution and reconstruction efficiency.

3.4.1 Momentum Resolution

The muon spectrometer instrumentation intends to achieve a momentum resolution of $\Delta p_T/p_T < 1 \times 10^{-4} \times p/\text{GeV}$ for $p_T > 300$ GeV. Therefore its resolution for the most energetic muons that are expected at LHC (1 TeV) will be about 10%. Figure 3.9 shows the individual contributions to the momentum resolution; single-wire resolution, chamber misalignment, multiple scattering and energy-loss fluctuations. It is obvious that for low energy muons the momentum resolution is limited by multiple scattering of the muons in the spectrometer material. For high energetic muons the momentum resolution is limited by alignment errors and MDT resolution which was assumed to be 80 μm for this simulation.
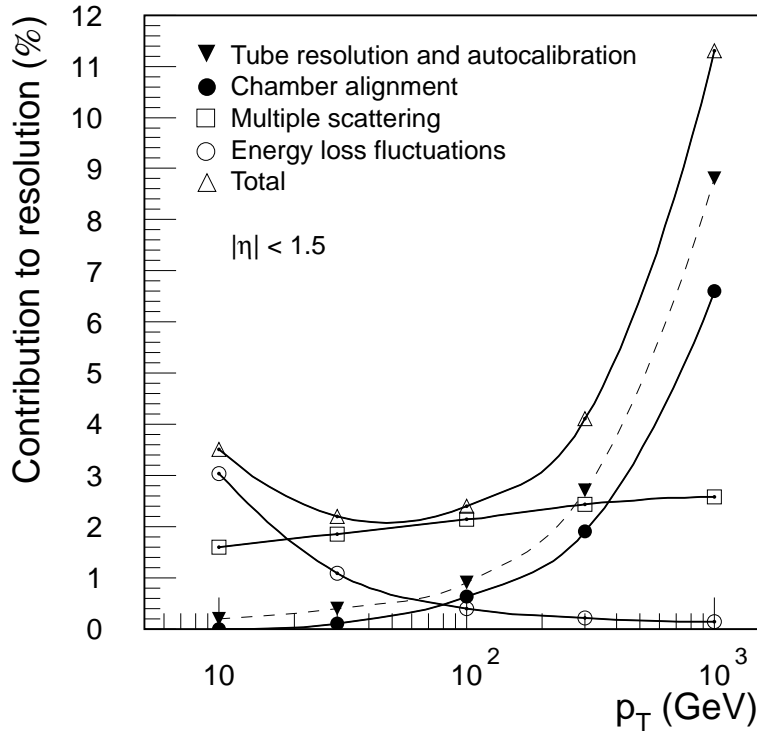
Figure 3.9: *Contributions to the momentum resolution as a function of p_T, averaged over $|\eta| < 1.5$.*

3.4.2   Reconstruction Efficiency

The reconstruction (or pattern-recognition) efficiency is defined as the efficiency to reconstruct muon tracks correctly. The high background levels result in large chamber occupancies (up to 20% for a maximum drift time of 700 ns) and hit rates (up to 300 kHz per tube) and put severe requirements on the single-tube efficiency and rate capability. The fraction of time where the MDT is occupied by an event i.e. the MDT is not able to measure a muon track is defined as occupancy. The fact that the occupancy influences the reconstruction efficiency consists the main argument for using a fast drift gas. In Figure 3.10 the reconstruction efficiency and the fake track rate (number of wrongly reconstructed tracks) for different background levels and layout schemes are shown [ATL94]. The results in this figure derived from a simulation where the maximum drift time was assumed to be 480 ns. The baseline gas Ar/CO_2 (93/7) has a longer maximum drift time (see section 5.2.1).
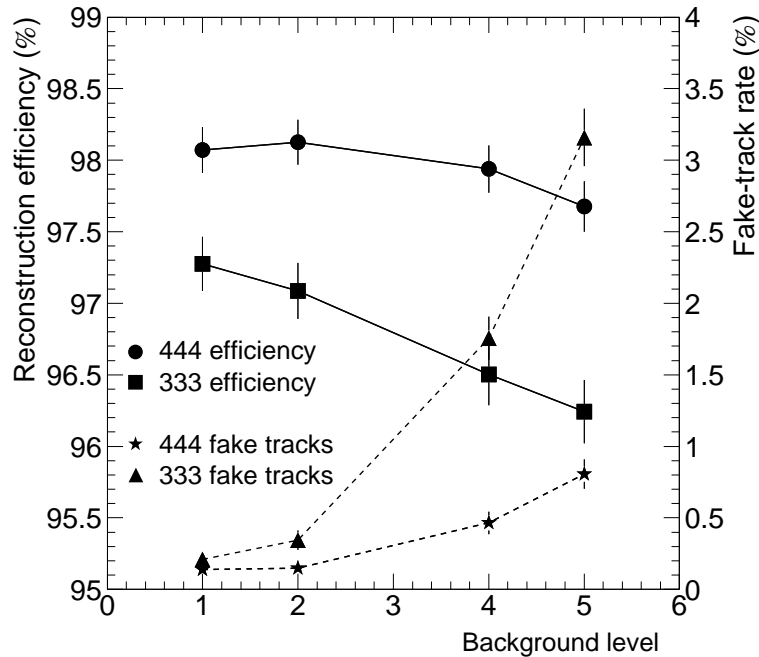
Figure 3.10: *Background level dependence of the reconstruction efficiency and the fake-track rate. A background level of five refers to a safety factor of five on top of the nominal background rate as has been derived from simulation. '444' indicates a chamber configuration with four layers of tubes per multilayer while '333' indicates a configuration with three layers.*

3.5   Alignment

A major challenge is the large active surface area (5500 m^2) covered by the 1194 MDT chambers together with the required measurement precision. This imposes stringent requirements on the precision of each individual drift tube, its alignment relative to the other tubes in the chamber and the alignment of chambers relative to each other. Due to the large scale of the spectrometer and the big number of chambers, it would be extremely difficult to keep the geometry of the chambers and their positions stable on the scale of the required tracking accuracy of 50 μm. Therefore a different approach was chosen for alignment; the chambers will be positioned only with a precision of the millimeter scale. Then the chamber movements and deformations will be controlled to a precision of better than 20 μm by an elaborated system of optical alignment beams which will be monitored constantly to apply the required corrections to the position measurement. This is the reason that the chambers are called 'Monitored Drift Tube Chambers' (MDT).

Owing to geometrical constraints, different alignment schemes are used to monitor chamber positions in the barrel (projective alignment), in the end-cap and the defor-

mations of large chambers (in-plane alignment). All alignment systems are based on optical straightness monitors. Optical beams, which traverse the active area of these optical monitors placed on their trajectories and mounted on the elements of the muon spectrometer, are used for the alignment monitoring.

A vital ingredient to reach the required precision for large detector surfaces is also the development of reliable online monitoring and calibration procedures. This aspect constitutes a major part of this thesis and it is described in subsequent chapters.

Chapter 4

Quality Assurance of the
MDT Chambers

The stringent requirements for the chamber construction are derived from the performance requirements discussed in the previous chapter (section 3.4). Here we are summarising the requirements for the production of the MDT precision chambers that are necessary to reach the desired precision of the momentum resolution:

- The wire of a single tube has to be positioned to 10 μm r.m.s (in projection) with respect to a reference surface on the endplug of the tube.

- The leak rate for a single tube must be $< 10^{-8}$ bar l/s.

- The wire tension (350 g) must have an r.m.s of < 7 g.

- The chambers must be constructed with 20 μm mechanical accuracy (r.m.s of the relative distance between the wires of the drift tubes).

- The maximum allowed dark current when the tube is operated at a gas gain of 2×10^4, should be 2 nA/m of tube length.

- The sag of the wires must be controllable within 10 μm up to a wire length of 4 m.

- The distance between the tube centre and the wire has to be less than 100 μm over the whole tube length to limit the deviations from the ideal rt-relation. Therefore the spacer structure of the chambers must guide the multilayers along the wires' length.

- The internal optical alignment system mounted on the spacer structure must monitor the displacement of the middle cross-plate due to temperature gradients at the few micron level.

Before the start of the series production of the MDT chambers in 2000, several MDT prototypes had been constructed by different ATLAS institutes. These prototypes were tested in dedicated test beams at CERN in order to assure the required performance. One of these prototypes (a BOS chamber) was built in 1998 at the Max Planck Institute in Munich as a common effort of several ATLAS muon institutes (MPI Munich, LMU Munich and Freiburg University). The chamber has a tube length of 3800 mm and a width of 2160 mm, the largest chamber width in the barrel part of the ATLAS muon spectrometer. It contains 432 drift tubes arranged in two triple layers (multilayers). Each layer contains 72 tubes.

In the following sections of this chapter we will introduce the quality assurance procedures and test facilities used for the evaluation of this prototype chamber. These same (with maybe minor variations) testing methods are currently used for the quality assurance of the MDT chambers.

4.1   Quality Control for the Single Drift Tubes

Before the assembly of the drift tubes in a chamber, extensive quality assurance tests of the tubes are required [ATL97]; once a drift tube is a part of an MDT chamber, a replacement becomes impossible. The quality of the individual tubes has a direct impact on the chamber performance. Therefore a careful validation of the tube performance is an integral part of the chamber construction. At the Ludwig-Maximilians University (LMU) in Munich we have developed a test facility which provides a fast response during drift tube fabrication whether each individual tube corresponds to the specifications concerning wire tension, leak rate, wire location, noise rate and signal response. In a first step this facility provided feed-back for a production of about 500 drift tubes, which were fabricated by the Max-Planck-Institute (MPI) in Munich, and for the development of tube mass production.

The most critical item of a drift tube are the end-plugs. They provide the electrical contact to the wire and hold the mechanical wire tension. The wire tension must be known in order to calculate the wire position in between the wire locator regions, as the wire has a sag along its length in the tube due to gravity effects. A conventional method verifying the wire tension (T) is to measure the oscillation frequency (f) of the ground mode wire vibration and to use the standard expression relating these two quantities to the wire density (ρ), the wire length (L) and the wire diameter (D) :

$$T \sim \rho \, D^2 L^2 f^2 \tag{4.1}$$

The wire tension was measured by using a commercial CAEN tension meter. It was found to be equal (~ 350 g) for all tubes within 1% rms.

The wire positions of the tubes have been measured using a pair of X-Ray sources and a pair CCDs for image recording. The tube is positioned rigidly into a V-groove being supported and sucked at 4 positions. The wire location can then be calculated from the projected wire images observed from two different angles, as illustrated in Figure 4.1, after the comparison between the shadows of the tube wire and those of the fiducials. During the first production phase, the measured positioning accuracy of this facility was better than 5 μm. Before absolute wire positions can be determined, the set-up was carefully calibrated with measurements on a drift tube mounted at several (8-16) equidistant azimuthal orientations into the V-groove.
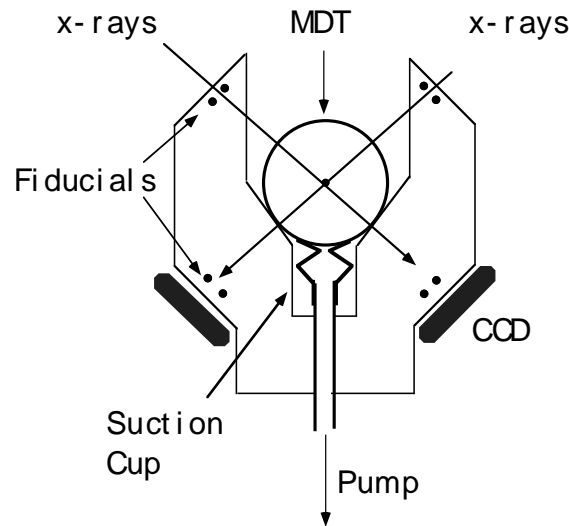
Figure 4.1: *Schematic illustration of the wire location measurement set-up.*

The measured displacements of the wires (Δy and Δx) are shown in Figure 4.2. The red circles have a radius of 10, 20, 30 , 40 and 50 μm. In Figure 4.3 the projections of the same results on the y and x axis of the reference frame are shown. Side A corresponds to the high voltage side of the tube and side B corresponds to its opposite side. The standard deviations of Gaussian fits to the wire coordinate distributions from these X-ray measurements are 10-12 μm, compatible with the specifications of Atlas.

The leak rate of the tubes was measured while they were filled with a gas mixture Ar/CH_4 (90/10) at 3 bar absolute pressure. A small vessel volume (0.1 l) was mounted around each tube endplug. This vessel volume was evacuated using a vacuum pump for about 30 - 40 minutes. Then after closing the valve between the pump and the vessel, the pressure increase as a function of time was recorded and the leakage rate was calculated. The maximum accepted leak rate according to the Atlas specifications is
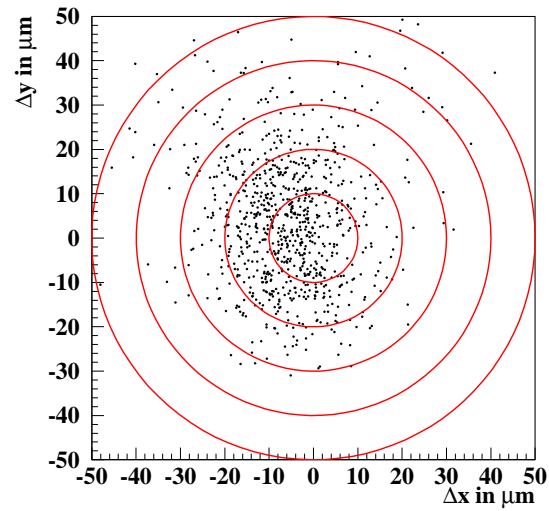
Figure 4.2: *Wire coordinates (Δx, Δy) for all tubes used for the construction of one of the first full size Atlas Prototype chamber.*

Figure 4.3: *Wire coordinates Δx and Δy for side A and B of the tubes.*

10^{-5} mbar l s^{-1} per tube. The signal response of the tubes was also tested. While the tube was filled with gas at 3 bar absolute pressure, the natural radiation background (cosmics) count rate as well as the count rate using a radioactive Americium source (10 μCi) were measured. During this test the leakage current (dark current) of the tube was less than 5 nA, compatible with the specifications.
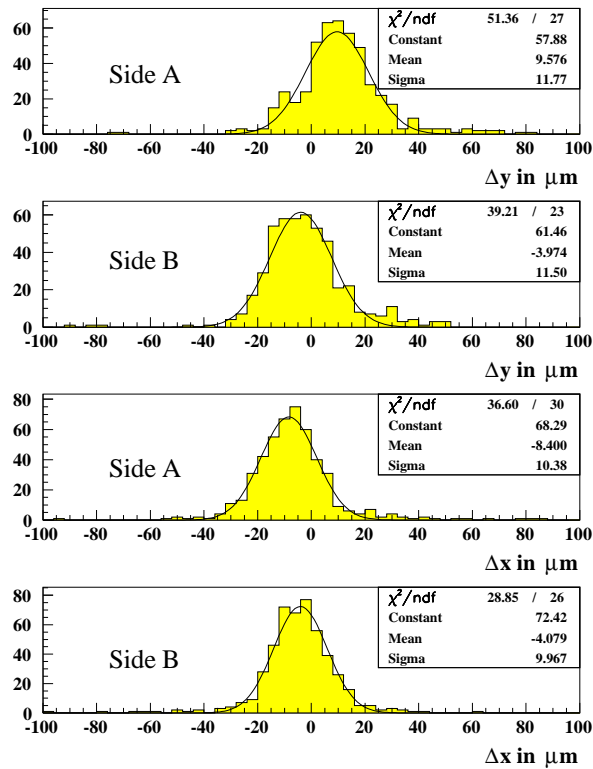
In the phase of final prototypes before the start-up of the chamber production, the test facility was also used for samples of tubes from other institutes participating in the production of MDT chambers (e.g. the MDT chamber from Frascati,Italy [CHO98]). Before the formal decision of the collaboration for the final end-plug design, mechanical acceptance tests with tubes that had different end-plugs were performed at this facility at LMU as the wire position measurement using the X-Ray set-up was the only facility of the collaboration in Europe. Besides the normal tests foreseen during the production stage, we also measured operational characteristics and the leakage tightness of each tube after repeated changes of the gas pressure and the environmental temperature of the tubes and after inducing vibrations on the wire, thus simulating conditions during the lifetime of a tube and during transports. The results of these tests were taken into account by the ATLAS Collaboration for the end-plug decision.

4.2   Quality assurance of the MDT chambers

A detailed description of the chamber construction is presented in [ATL97] and [BOS98]. After the assembly of a chamber extensive validation tests are performed to assure both its mechanical precision and its operational stability.

The chamber should be gas tight. Its leak rate is measured and it should be less or equal to 10^{-5} mbar l/s per tube. After the front-end electronics is mounted, high voltage is applied to verify the functionality of the electronics. At this phase the dark current is also measured. In addition the correct behaviour of the in-plane alignment system is assured.

As it has already been mentioned, the anode wires are placed very accurately within the chamber (20 μm r.m.s). This demanding precision is an essential ingredient of the MDT concept and needs to be continuously confirmed during the production phase after each chamber assembly. A very elegant way to verify wire positions inside an assembled chamber is the use of a large X-Ray tomograph placed at CERN. This high precision device (better than 5 μm) was specially designed, constructed and upgraded by the ATLAS Collaboration [BER98].
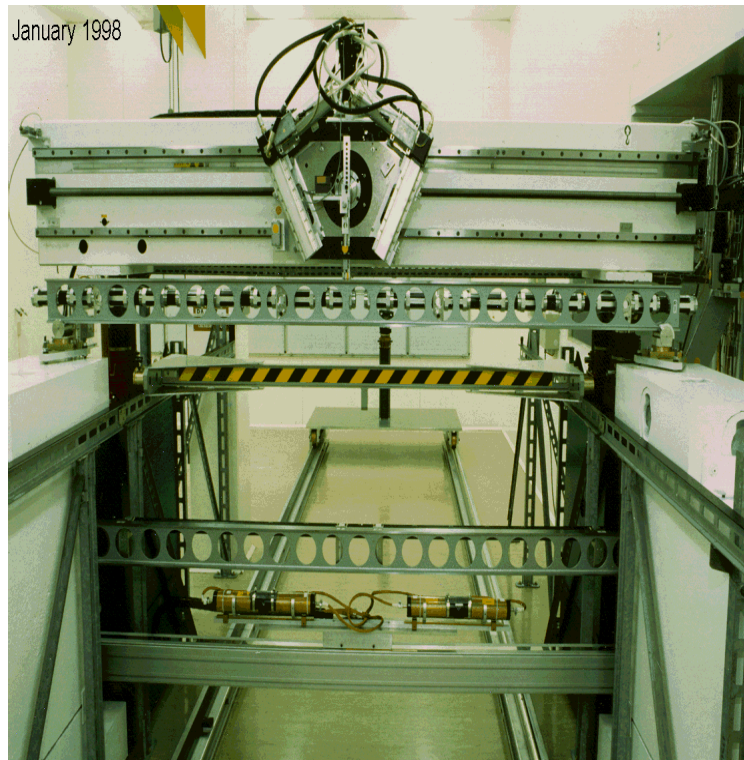
Figure 4.4: *Photograph of the large X-ray tomograph.*

Figure 4.4 shows the large X-Ray tomograph installed in a clean room, which provides high mechanical stability and well-controlled environment (see also [DRA97]). The X-ray tomograph consists of:

- A fixed 3.5 m long iron portico, equipped with a precise motorized cart rolling along the x-axis (along the direction of the wires).

- Two collimated X-Ray beams positioned firmly on the rolling cart at about $\pm 31^o$ with respect to the z-axis (the coordinate in the chamber plane, perpendicular to the wires). The two beams have a cross-section of about 30 μm $\times$ 8 mm and a divergence of about 60 μrad.

- Four high precision laser interferometers which monitor the movements of the X-Ray sources. They record the linear displacement along the z-axis, the vertical straightness in the y-axis (the coordinate perpendicular to the chamber plane), the pitch angle (rotation around the x-axis) and the roll angle (rotation around the z-axis).

- A reference frame made of two rulers installed above and under the chamber. The rulers are made of two layers of a precise pattern consisting of 60 $\times$ 30 μm

golden strips put on ceramic plates and mounted on a carbon fibre support.

- A rolling cart which supports and align the chamber to be measured.

- One small moving cart enslaved to the X-Ray cart, supporting two scintillators (NaI crystals) following the beams.

The precise synchronization of the different parts of the X-ray tomograph during scanning as well as the analysis of the results of the scans are performed in an automated way. Critical problems of automation (automatic alignment of the chamber, finding positions of the scans along the chamber, quality checking of the measurements etc) are still under development aiming in a fully robotized operation of the X-ray tomograph.

The operational principal of the tomograph is based on the enhanced absorption of a fine, collinear X-Ray beam in the tungsten wires as opposed to the aluminium of the tube walls and the gas. The chamber to be measured is placed between the X-ray sources and the X-Ray detector (scintillators) that records the absorption profile during scanning along the multilayer cross-section of the chamber. Scanning under two different beam angles with respect to the chamber plane (two X-ray sources) provides a stereo measurement such that a two-dimensional map of wire positions can be reconstructed (passive method). Every chamber is scanned in a few positions along the tube length. Using the external reference frame of the X-Ray tomograph, a three-dimensional map can finally be constructed allowing to measure the wire sag along the tubes. After the analysis, the results are stored in a database providing the full list of the wire position and accuracy.

Several MDT prototypes as well as chambers from the series production have been tested at the X-ray tomograph. One of them was the BOS prototype mentioned earlier in this chapter and the analysis of these data is described extensively in [KRO00]. It is planned that the X-ray tomograph will scan 10 - 15% of the ATLAS MDT chambers setting up a data-base with their wire positions.

At the production sites of the ATLAS collaboration, cosmic-ray set-ups offer the possibility of a full functionality test and calibration of the chambers using cosmic rays. Such a test stand was built in 2001 by the Ludwig-Maximilians University (LMU) in Munich. It is devoted to the quality control of 88 BOS chambers for the ATLAS muon spectrometer that are being built at MPI Munich.

The cosmic ray muon test stand consists of a permanent part and chambers to be tested. The permanent part consists of two MDT reference chambers, measured at the X-ray tomograph at CERN. Below the lower MDT reference chamber there is an absorber consisting of a layer of solid iron 34 cm thick. Below that iron absorber is

a hodoscope with a time resolution better than 800 ps with the counters oriented perpendicular to the MDT tubes. Below the hodoscope is one layer of streamer tubes, giving a spatial resolution of about 5 mm with tubes oriented parallel to the MDT tubes and placed about 1 m below the absorber. Above the top MDT reference chamber is another hodoscope made of scintillators that are oriented perpendicular to the MDT tubes. The chambers to be tested are positioned in between the two reference chambers. The set-up offers the following possibilities:

- Test of a single chamber with an angle 0[1](possibly also 22.5 or 67.5 degrees, i.e. in the position the BOS chambers will be mounted in ATLAS).

- Test of several chambers simultaneously at 0 degree.

Apart from the determination of gas leak rates and leakage currents, several very important performance parameters of the chambers will be tested such as efficiency, noise and drift-time spectra for each tube. It is furthermore planned to assure the mechanical precision of the chambers by measuring the position of their wires relative to those of the two reference chambers. The expected precision in the determination of wire positions, as derived from specially designed simulation programs [KOR00] is 10 - 15 μm in the z-coordinate for chambers lying flat. It is expected to measure the wire positions relative to the reference chambers in the y-coordinate, though with lower precision (50 μm) (see Figure 3.8 for the definition of the coordinate axes).

Moreover, much has been learned about the performance of chambers which have been operated in test beams at CERN. These activities have been focused on basic quality parameters such as reconstruction efficiency and spatial resolution of precision chambers, efficiency and timing of trigger chambers and the high-rate behaviour of all muon detectors. The experience and outcome obtained during these activities have directly influenced the chamber construction. The main ATLAS test beam facility is the CERN H8 beamline. At this test beam the BOS prototype was tested in summer of 1998 and autumn of 1999 (see chapter 5).

It is obvious that a lot of effort is being put from the ATLAS Collaboration into the assurance of the required mechanical accuracy of the MDT chambers. The present thesis contributes in this effort, as it will be described in the subsequent chapters.

---

[1]i.e. the tube layers of the chamber are placed parallel to the ground plane.

Chapter 5

Calibration of the wire positions of a BOS Chamber

The studies in this chapter refer to the data taken with the full scale prototype MDT chamber mentioned in chapter 4. The chamber has a length of 3800 mm, a width of 2160 mm and consists of two triple layers (multilayers) of drift tubes. It was transported to CERN and was scanned by the ATLAS X-ray tomograph (section 4.2). The results of the tomograph revealed that the chamber fulfills the specifications (mechanical accuracy of 20 μm). After the scan, careful evaluation of the chamber performance was carried out in August 1998 and September 1999 at a high energetic muon test beam at CERN. It is necessary to emphasize the fact that during the 1998 tests the chamber was filled with $Ar/N_2/CH_4$ (91/4/5) whereas during the 1999 tests it was filled with Ar/CO_2 (93/7). The reason for this change will be given in a following section. In this chapter the experimental set-ups used for this evaluation as well as a method to calibrate the positions of the wires of this BOS chamber without using any external reference frame are described. The correctness of our results has been verified by a comparison with the results given by the X-ray tomograph. This comparison is also presented in this chapter.

5.1   Set-up for the $Ar/N_2/CH_4$ Measurements

The first evaluation and extensive tests of the above mentioned first BOS prototype took place in August 1998 in the H8 muon test beam at CERN. The energy of the muon beam was 180 GeV. The experimental set-up is shown in Figure 5.1. The chamber was installed with the tubes in vertical position. A 10×10 cm^2 scintillator trigger, placed at the center of the beam profile, was used providing the reference time of the MDT tubes. 'ODYSSEUS' [DEI99], as shown in the same figure, is a Silicon Microstrip Tracker which was used as external reference system. It is a beam telescope that can perform reliable measurements of drift time tube resolution and efficiency and can verify unambiguously reconstructed tracks through chamber prototypes. The six

silicon microstrip detectors (5.1×5.1 cm^2) that consist ODYSSEUS have a resolution of 7 μm each. Four out of the six planes measure the precision coordinate perpendicular to the MDT wires, the other two detectors give us the 'second' coordinate parallel to the wires.

The chamber was filled with $Ar/N_2/CH_4$ (91/4/5) at 3 bar absolute pressure. Its tubes were operated in proportional mode at 3270 Volts in order to accomplish the required gas gain of 2×10^4. The read-out electronics used were BNL preamplifiers [BNL73], shapers (with a peaking time of 15 ns) and discriminators (with an effective threshold of 25 primary electrons) and TMC TDCs [KEK] with a bin width of 781 ps.
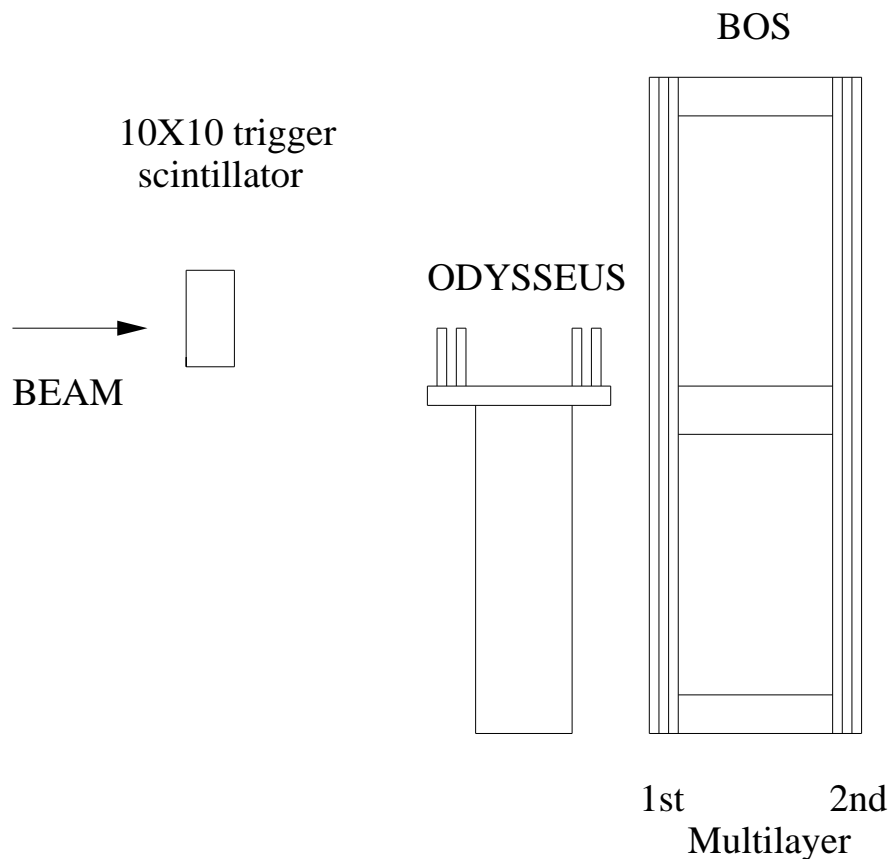

Figure 5.1: *Experimental set-up in August 1998 with* $Ar/N_2/CH_4$. *ODYSSEUS was placed at the position indicated only when it was used for the measurement of the chamber resolution and the rt-relation for the specific gas mixture.*

5.1.1 Aligning the Drift Time Spectra

A crucial parameter to determine the hit position in space from the time measured by the TDC is the offset t_0 of each individual tube, i.e. the TDC response for a null drift path. The time t_0 is different for each channel and is determined by the delays of the signal cables and the front-end electronics.

The time t_0 can be measured for each tube by analyzing the raw time distribution of the hits (drift time spectrum). In Figure5.2 a typical drift time spectrum while using the $\mathrm{Ar}/\mathrm{N_2}/\mathrm{CH_4}$ gas mixture is shown. The leading edge of such a distribution can be determined by fitting the whole spectrum with the following function [CRE97]:

$$N(t) = P_1 + \frac{P_2 \cdot [1 + P_3 \cdot \exp(\frac{P_6 - t}{P_5})]}{[1 + \exp(\frac{P_6 - t}{P_7})] \cdot [1 + \exp(\frac{t - P_4}{P_8})]} \tag{5.1}$$
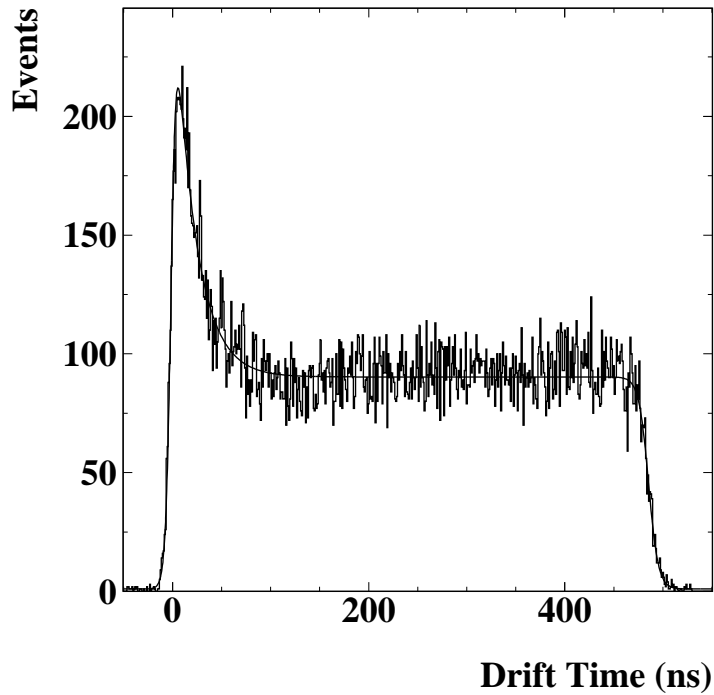
Figure 5.2: *The drift time spectrum for a typical tube for the* $\mathrm{Ar}/\mathrm{N_2}/\mathrm{CH_4}$ *(91/4/5) gas mixture. The fitted function curve is also visible.*

where $N(t)$ is the number of hits in each time interval and P_i (i=1,..,8) are the parameters that are fitted for each tube. P_1 and P_2 represent the amounts of the constant uncorrelated background coming mainly from the electronic noise and of the true hit

distribution. P_3 and P_5 describe the non-uniform peak of the distribution whereas P_6 and P_4 correspond to the minimum and maximum drift time respectively. Finally the parameters P_7 and P_8 describe the shape of the leading and trailing edges.

Once the parameters are obtained from the fit, the t_0 is defined as the value of the parameter P_6. This value corresponds to the point where the Fermi function of the numerator in (5.1), that is fitted at the leading edge, changes curvature. Finally this t_0 value is used as a correction for the drift time of each hit that the TDC gives.

5.1.2   The Least-Squares Track Reconstruction Technique

As it was described in Section 3.3.1, the drift time of the electrons from the track of the muon, which traverses the drift tube, to the wire is converted into a radius (r) of the impact circle using the space-time relationship (rt relation). A muon track can then be reconstructed through both multilayers of the MDT chamber by fitting a straight line to the impact circles. For our analysis this was done by minimization of the following function:

$$\chi^2 = \sum_{i=1}^{N_{hits}} = \frac{[r(t_i) - r_i^{(fit)}]^2}{\sigma_i^2} \tag{5.2}$$

where $N_{hits} = 6$ as only tracks with six hits (one hit on each of the six layers of the chamber) were used and σ_i is the single wire resolution of the ith tube at the radius $r_i^{(fit)}$, as measured with an external reference system. The hit radii $r(t_i)$ define the impact circles (calculated from the rt-relation) and $r_i^{(fit)}$ is the shortest distance between the reconstructed track $y = m \cdot z + c$ and the ith wire represented by a point with coordinates $(z_i, \ y_i)$ (Figure 5.3), that is :

$$r_i^{(fit)} = \frac{|m \cdot z_i + c - y_i|}{\sqrt{1 + m^2}} \tag{5.3}$$

A quantity that will be used extensively in the following sections is the 'residual'. As it is demonstrated in Figure 5.4, the difference between the fitted muon track ($r_i^{(fit)}$) and the measured radius ($r(t_i)$) is defined as 'residual':

$$Residual = r_i^{(fit)} - r(t_i) \tag{5.4}$$

r(t$_1$)

r$_2^{(fit)}$
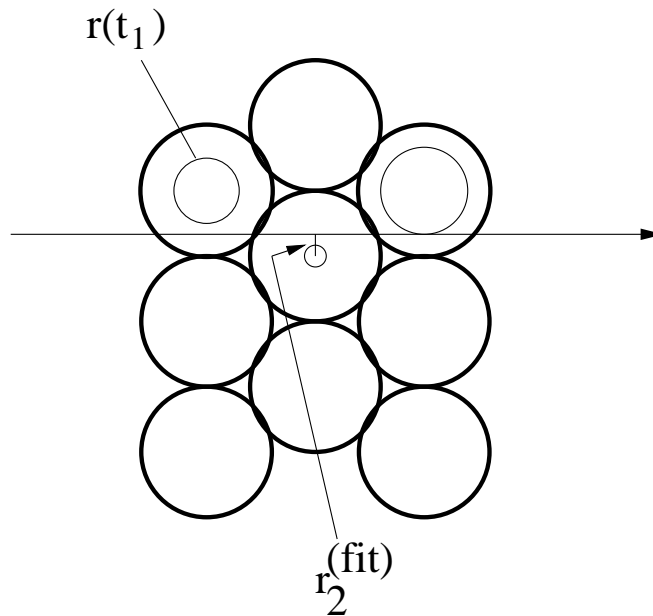
Figure 5.3: *Conventional fit of a straight line to the impact circles. Only one multilayer of drift tubes is shown in this figure. The measured drift times are first converted into radii, then the χ^2 function (5.2) is minimized with respect to the track parameters m and c.*

Muon Track

r measured

Residual

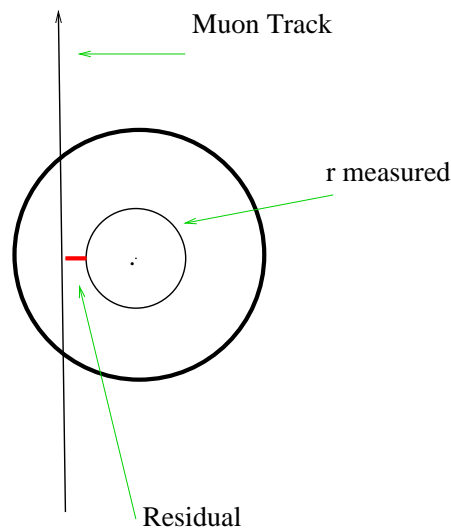Figure 5.4: *The difference between the fitted track ($r_i^{(fit)}$) and the measured radius ($r(t_i)$) is defined as 'residual'. The bold circle is the tube circumference and the dot in its center is the sense wire (anode).*

5.1.3 Description of the wire calibration method

In Figure 5.5 the coordinate frame of our set up at the muon test beam is given. As the chamber was placed vertically to the muon beam, the position of each wire is defined by two coordinates which are perpendicular to the wire: the y coordinate that is perpendicular to the tracks' direction and the z coordinate which is parallel to the tracks' direction.
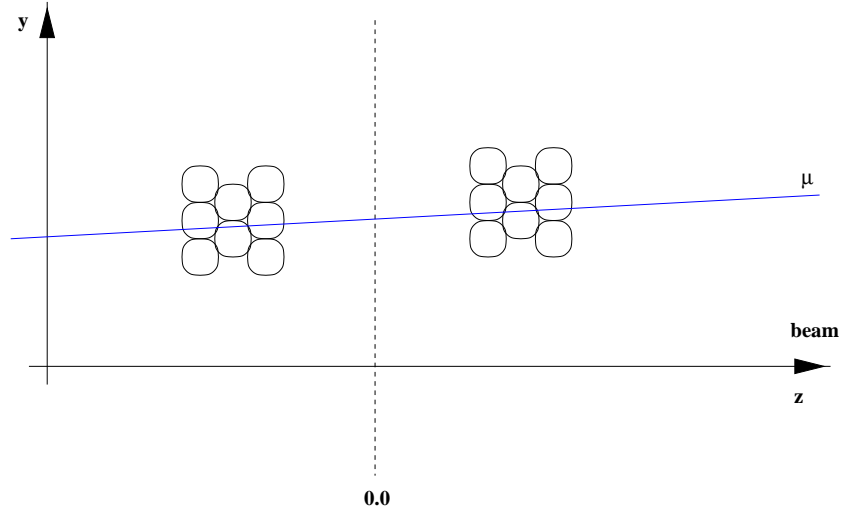
Figure 5.5: *The coordinate frame of the set-up in the muon test beam. The solid blue line corresponds to a muon traversing the two multilayers of the chamber. The dashed line indicates the origin (0.0) of the z axis of the reference frame.*

When the wire of a tube is displaced with respect to its nominal position used in the track fit, the distribution of the residuals versus the drift distance for tracks which traverse the tube right from its wire is not symmetric with the one for tracks which traverse the tube left from its wire. In Figure 5.6(a), the residuals versus the drift distance for one tube is shown. In order to illustrate better the asymmetry between the two residual branches, we divide the drift distance in 30 bins (1mm of width each), fit a Gaussian distribution to the residuals in each bin and then plot the mean values of these distributions as rectangles in Figure 5.6(b). The residuals left from the wire are called 'residuals left' (res_{left}) and the residuals right from the wire 'residuals right' (res_{right}). Between the two branches there is a distance δ. For the determination of the relative wire positions, the positions of two tubes (one on each multilayer) are kept fixed (Figure 5.7), while the y coordinates of the twelve surrounding tubes are moved till the distributions of their residuals left and right from their wires become symmetric that is till the function F which is defined as

$$F = \sum_{i=1}^{14} \sum_{j=1}^{N} \frac{((res_{right})_{ji} - (res_{left})_{ji})^2}{\sigma_{rji}^2 + \sigma_{lji}^2} + \frac{(res_{right})_{ji}^2}{\sigma_{rji}^2} + \frac{(res_{left})_{ji}^2}{\sigma_{lji}^2} \tag{5.5}$$

is minimized. The σ_r and σ_l are the standard deviations of the distribution of the residuals right and left from the tube wire respectively. The first sum is over the group of the 14 tubes which is called 'a flower pair' while the second is over all the residuals values (N) of the branches. The last two terms of the above function offer extra constraints so that the width of the residuals, when they are projected on the y axis of Figure 5.6b, is minimum and centered at zero.

(a)   (b)
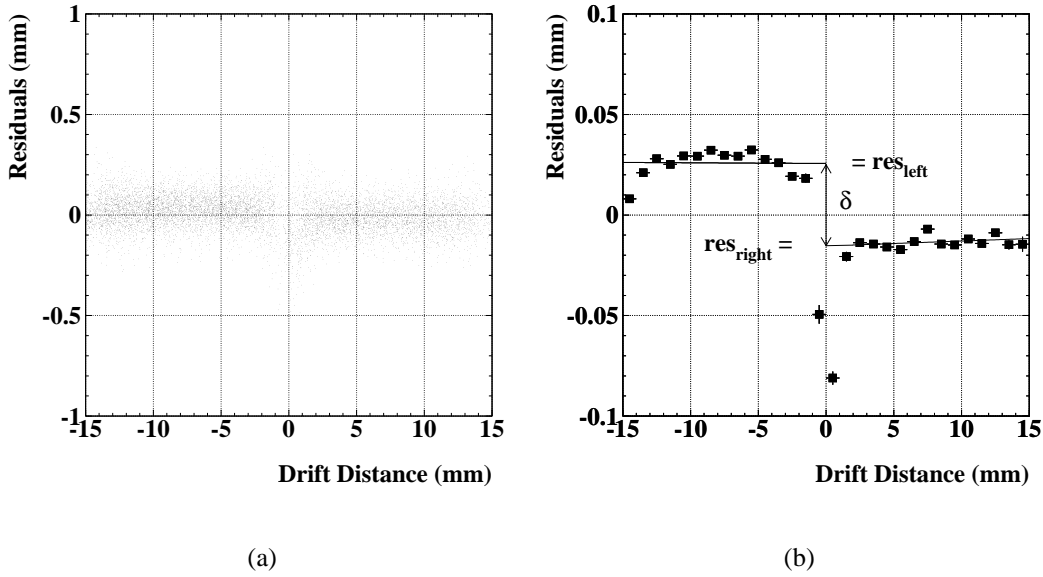
Figure 5.6: *(a) Residuals distribution versus the drift distance in a tube while the chamber was filled with* Ar/N$_2$/CH$_4$ *(91/4/5). (b) Residuals distribution asymmetry for tracks traversing the wire from left and right. The error bars which are very small to be visible in most of the points express the standard error of the mean value in each bin. The distance between the two branches of the residuals is indicated (δ).*

It is worthwhile mentioning that in this procedure we do not take into account the residuals that are closer than 2 mm to the wire and closer than 1 mm to the wall. It is also obvious in Figure 5.6 that there is a larger spread of the residuals close to the wire. Very close to the wire the spatial resolution of the tube worsens as a result of electron cluster position fluctuations [DEI98] and charge fluctuations. Moreover near the wall the MDT starts becoming inefficient [RIE97a]. The reason for that is the fact that near the wall the track length within the gas volume becomes short and in some cases the primary ionization is too small for obtaining a pulse greater than the discriminator threshold.

After finding the new wire positions the asymmetry of the residuals left and right of the wire disappears (Figure 5.8).
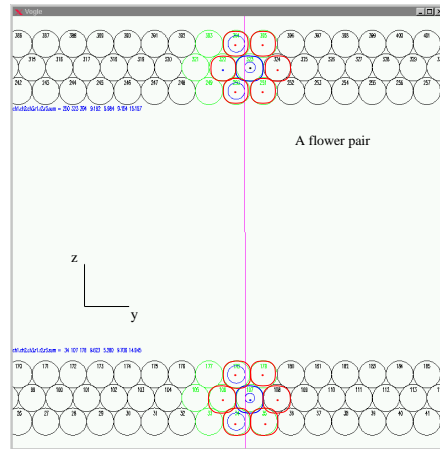
Figure 5.7: *A cross section of the chamber is shown. The tubes indicated in blue are the two central tubes (one on each multilayer) whose wire positions are kept fixed. The surrounding tubes indicated in red, are the ones whose wire positions are varied simultaneously till the asymmetry of the residuals left and right of the wires disappears.*
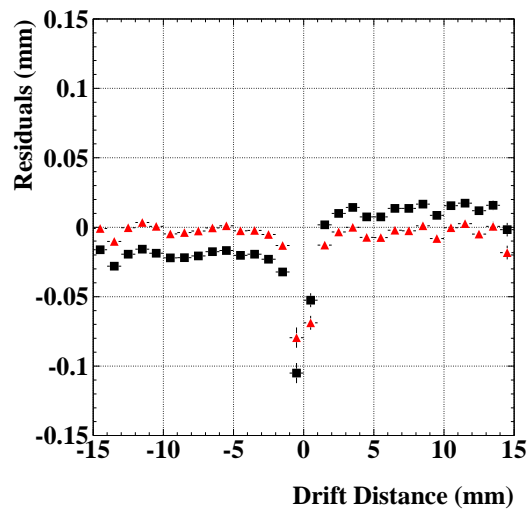
Figure 5.8: *After finding the new wire positions the asymmetry of the residuals left and right of the wire disappears. The black rectangles are the residuals before finding the wire positions and the red triangles correspond to the residuals after the calibration of the wire positions.*

It should be pointed out that this final form of the minimization function (5.5) was obtained after several steps of optimization. Initially we were minimizing the rms of

the residual distributions left and right from the wire together. Later we used only the first term of the (5.5). These two approaches resulted in a not so stable minimization procedure mainly because of the presence of the half illuminated tubes, that is the tubes within the flower pair that are 'illuminated' with tracks only along half of their diameter. These tubes have only one residual branch and not two as it will be shown more detailed in section 6.1.1. Therefore the absence of the last two terms in (5.5) could not provide the necessary constraints in order to incorporate fully these half illuminated tubes into the minimization procedure.

5.1.4 Results and Comparison with the X-ray Tomograph

The rt-relation that we used in our analysis for the 1998 data was the one for $\mathrm{Ar/N_2/CH_4}$ (91/4/5) that was calculated (by autocalibration and the use of external reference system) during test beam measurements in the previous years [ALE99a] (see also Figure 5.14(a)).

As the trigger used in our set-up was quite small (10×10 cm^2), the wire calibration method was developed while analysing the data taken by only a small group of 14 tubes (one flower pair). The total number of six-hit tracks that were used in this flower pair was about 60000. After applying the method to this flower pair, we measured the wire displacements in the y direction with respect to the ideal grid to have a distribution with an rms of $\sim$19 μm (Figure 5.9). This result is in agreement with the required mechanical accuracy of 20 μm with which the chamber was built.
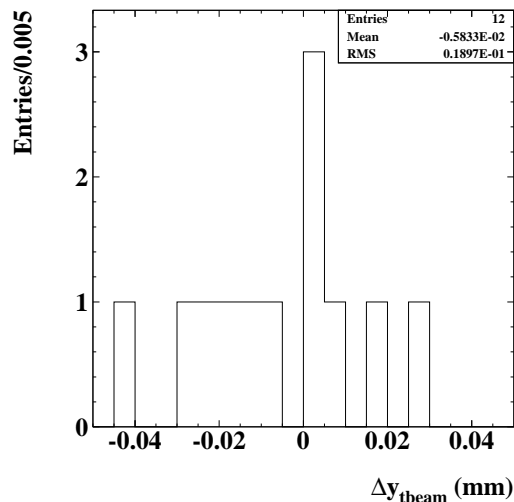
Figure 5.9: *Wire displacements in the y direction with respect to the ideal wire grid for the 12 tubes of one flower pair (data 1998). The rms of the distribution (19 μm) is in agreement with the required mechanical accuracy of the chamber (20 μm).*

The next step in order to verify the reliability of the method, was to compare these results with those provided by the X-ray tomograph. The tomograph scanned the BOS chamber in several positions along its full length. As the beam position during our tests traversed the chamber in its middle, the tomograph scan that we used for our comparison was the one that was performed in the middle of the chamber[1]. Figure 5.10 shows the shift map of this scan in the X-ray tomograph reference frame.

The comparison between our results and those of the tomograph revealed a nice correlation (Figure 5.11) and showed that the accuracy of the method is better than 10μm (Figure 5.12).
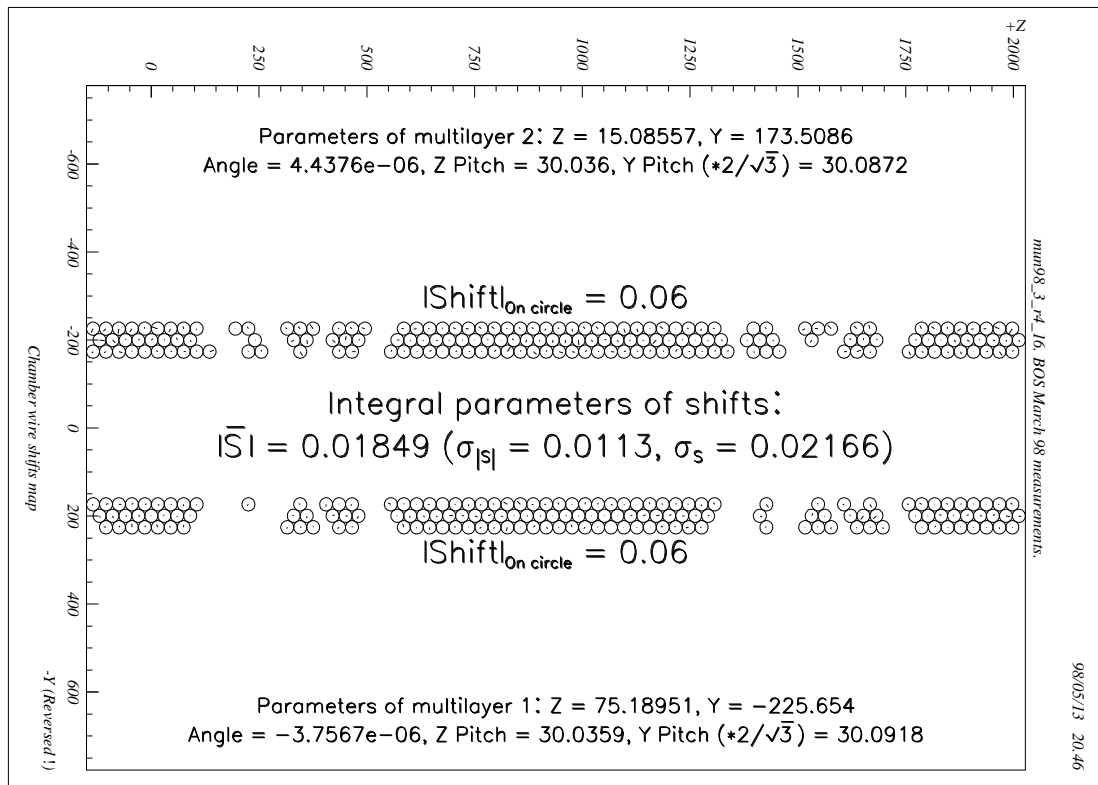
Figure 5.10: *The X-ray tomograph shift map of the scan* mun98_3_r4_16. *The displacements are shown in direction and amplitude for each wire of the BOS prototype chamber. All values are in mm. Many wires are hidden by the chamber cross plates.*

---

[1]According to the X-ray tomograph abbreviation this scan was named as mun98_3_r4_16, where 3 indicates that the scan was in the middle of the chamber, r4 indicates that the chamber was turned by 180 around vertical axis (original orientation) and 16 is just the consequent number of scan during measurements.
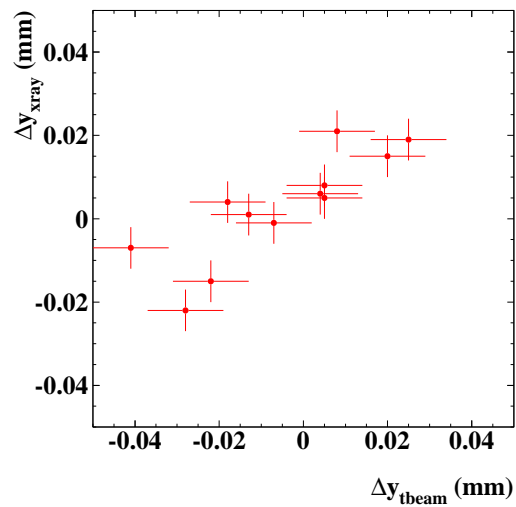
Figure 5.11: *The displacements of the y coordinates of the wire positions from their nominal positions for the 12 tubes of the flower pair measured by the X-Ray tomograph (Δy_{xray}) versus the corresponding displacements (Δy_{tbeam}) found with the method discussed. The error bars for the tomograph points are equal to 5 µm while those of the calibration method are 9 µm (as shown in the Figure 5.12 both results agree within 10 µm).*
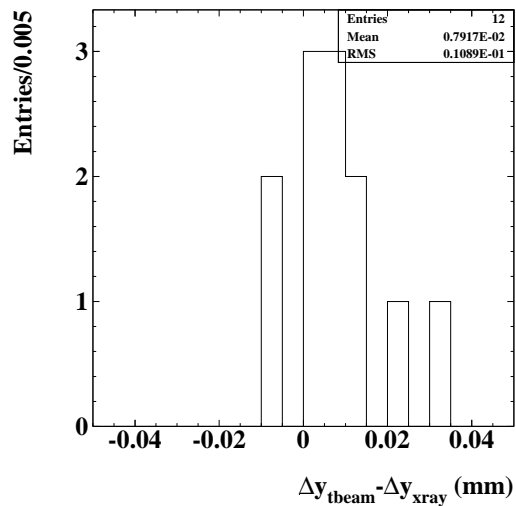
Figure 5.12: *The RMS of 10 µm of the distribution of the difference Δy_{tbeam}-Δy_{xray} shows that the accuracy of the method is better than 10 µm.*

5.2 Set-up for the Ar/CO_2 Measurements

After the success of the calibration method to find the wire displacements in the y direction for twelve tubes, it was decided that data from a bigger area of the chamber should be taken in order to test the validity of the method for a complete chamber. This plan was carried out during the 1999 test beam period. The experimental set-up is shown in Figure 5.13. The beam energy was 300 GeV.
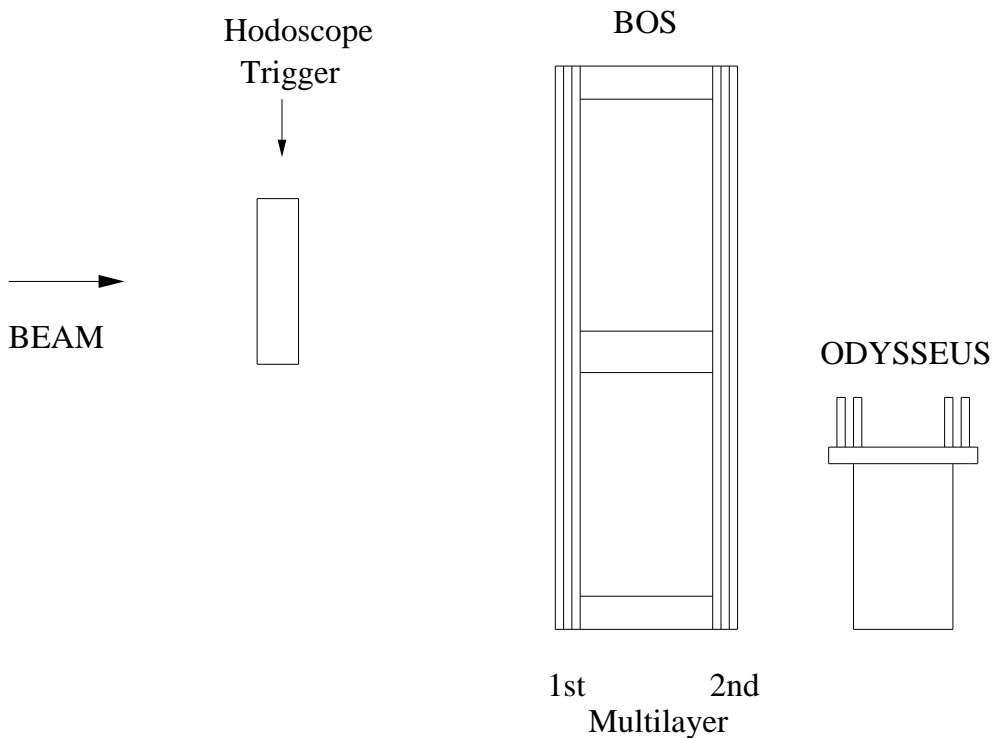
Figure 5.13: *The Experimental set-up in September 1999 with* Ar/CO_2.

A large hodoscope trigger (1×1 m^2) consisting of 12 scintillators was used. The chamber was filled with Ar/CO_2 (93/7) at 3 bar absolute pressure. Its tubes were operated in proportional mode at 3080 Volts corresponding to a gas gain of 2×10^4. The read-out electronics used were again BNL preamplifiers, shapers (with a peaking time of 15 ns) and discriminators (with an effective threshold of 25 primary electrons). TDCs of the KLOE Experiment [VEN95] with 1.042 ns bins were used for the hit-time measurement.

5.2.1 The Gas choice

The gas choice is one of the most critical issues for the MDT system. The favourite gas mixture candidate until the summer of 1998 was the $Ar/N_2/CH_4$ (91/4/5). It was chosen due to its very linear rt relation (see Figure 5.14(a)), the high drift velocity

(maximum drift time of 480 ns) and the good spatial resolution of typically 80 μm.

One of the biggest concerns is the possible degradation of the drift chamber performance due to organic deposits on the electrodes, which are created by processes catalyzed by ionization. The strength of these processes has been found to be proportional to the charge deposit on the anode. Operating at a gas gain of 2×10^4 the charge deposit will be 0.6 C/cm in 10 years ATLAS operation. This charge deposit can either reduce the MDT performance or even completely destroy a tube. It has been found in extensive aging studies that gas mixtures containing organic compounds (e.g. CH_4) produce thin deposits on the wire and on the cathode which affect the performance.

The former baseline gas mixture $Ar/N_2/CH_4$ (91/4/5) showed strong aging damage (decrease of the pulse height, high count rates) at already 1/5 to 1/2 of the charge deposit which is expected during ten years of ATLAS operation [SPE98]. The new baseline gas Ar/CO_2 (93/7) showed no ageing but is slower (maximum drift time 680 ns) and rather non-linear (Figure 5.14(b)). Its drift velocity depends strongly on the reduced electric field, $\frac{E}{\rho}$, where E is the electric field inside the tube and ρ is the gas density. Due to this strong dependence, slight environmental changes (i.e. temperature, pressure and voltage) that influence either the E or the ρ, affect the drift velocity in a tube and consequently the rt relation. Therefore non-linear drift gases show lower operational stability than the linear drift gases.

(a)   (b)
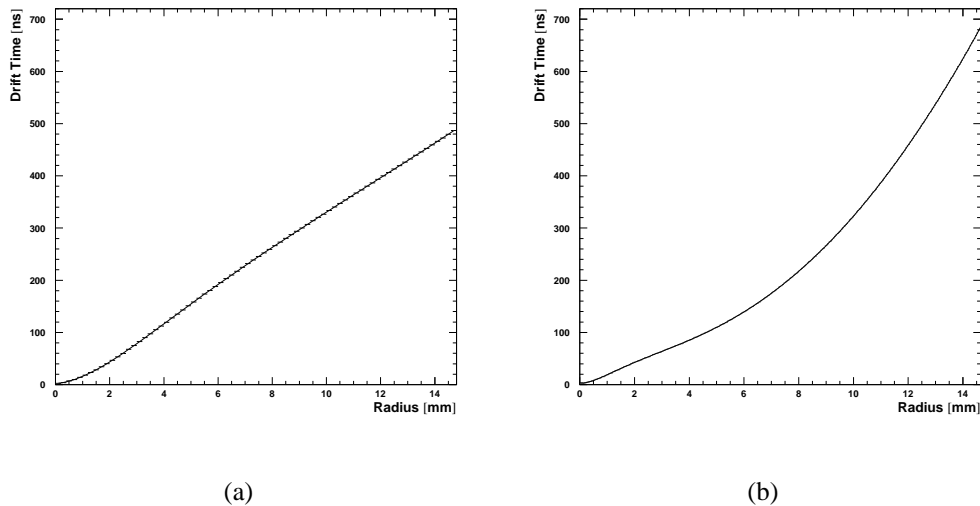
Figure 5.14: *Measured rt relations (a) for* $Ar/N_2/CH_4$ *(91/4/5) and (b) for* Ar/CO_2 *(93/7) at magnetic field B=0 and a gas gain of* 2×10^4.

5.2.2 Spatial Resolution of the chamber

The spatial resolution of the chamber is also different for the two different gas mixtures (the former and the present baseline gas). The spatial resolution as a function of the drift distance r is defined as the width of the residual distribution in discrete slices in r [ALE99a]. The residual distributions are obtained by comparing the track position $r_{predicted}$, predicted by the reference system (ODYSSEUS) and the track position $r(t_{measured})$, measured with the drift tube. In Figure 5.15 the resolution as a function of the distance r from the wire is given for both gases: (a) for $Ar/N_2/CH_4$ (91/4/5) [ALE99b] measured in 1997 and (b) for Ar/CO_2 (93/7) measured in 1999 [KOR98].

(a)   (b)
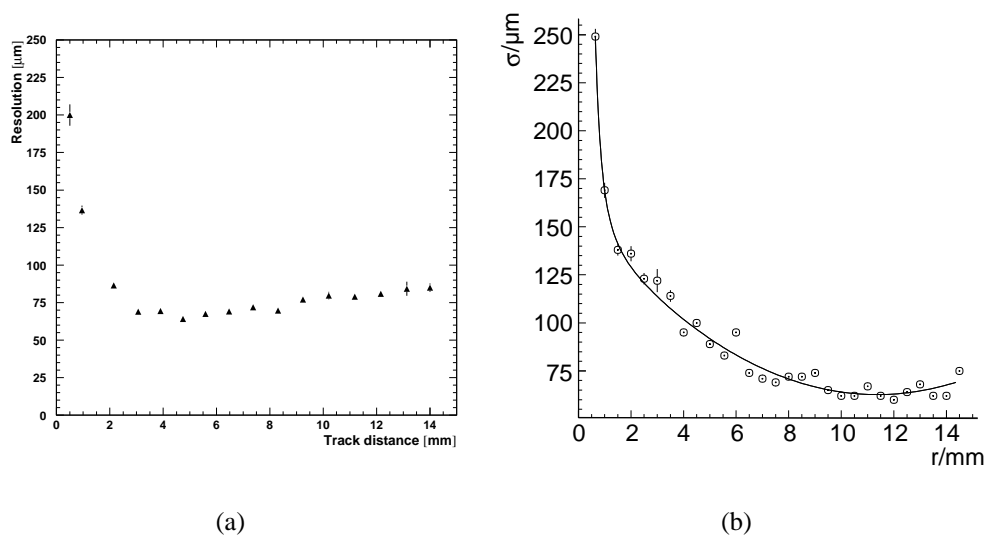
Figure 5.15: *Resolution as a function of the drift distance from the wire: (a) for* $Ar/N_2/CH_4$ *(91/4/5) (b) for* Ar/CO_2 *(93/7).*

The main reason for the qualitatively different radial dependence of the resolution for the two gases is the higher diffusion in $Ar/N_2/CH_4$ which causes the deterioration for $r > 4$ mm [RIE99]. The average tube resolution $< \sigma >$ is given by quadratically averaging the local resolution (σ) as a function of the drift distance, that is:

$$< \sigma >= \sqrt{\frac{1}{R-1} \int_{1mm}^{R} [\sigma(r)]^2 \, dr} \qquad (5.6)$$

where R is the drift distance. According to the ATLAS convention, the first millimeter is excluded from the average because near the wire the resolution is so bad that hits in this range will often not be taken into account by track fits through an MDT chamber. Moreover, the quadratic average would be dominated by the large $\sigma(r)$ in this small interval and would not be a representative number. The average resolution (for operation

without radiation background) as defined in equation (5.6) for $\mathrm{Ar/N_2/CH_4}$ (91/4/5) is 80 μm, whereas for $\mathrm{Ar/CO_2}$ (93/7) is 69 μm.

5.2.3   Results and Comparison with the X-ray Tomograph

Using the silicon strip detector telescope (ODYSSEUS) as external reference system, the r-t relationship was determined. It was compatible with previous testbeam measurements (see section 5.2.1) and we used it for analysing the data from 6 flower pairs (51 tubes in total). This time the adjustment of only the t_0 parameter, as it was described in section 5.1.1, was not enough. Moreover the t_0 could not be measured with the same accuracy for all tubes covered by the large hodoscope trigger. As the dimensions of the beam were 7 $\times$ 7 cm^2 (Gaussian profile), the tubes that were close to the center of the beam had more hits so their t_0 was determined with higher accuracy than the tubes that were placed further from this position.

In order to interpret our data in the best possible way and being able at the same time to measure the positions of the wires, in a first approach we used for each tube a different r-t relationship by applying the conventional autocalibration procedure simultaneously for each tube. During this autocalibration we could only use tracks perpendicular to the chamber since we did not have data sets where the tracks formed different angles with the chamber (as required for the autocalibration procedure).

The wire displacements obtained in this way were consistent with the X-Ray tomograph measurements. This approach though raised the important question, whether the use of an individual r-t relationship for each tube is really necessary.

Further studies showed however, that the tubes could be treated with a common rt relation and that the only parameters that had to be adjusted individually for each tube were a time offset and a scale parameter. More precisely we fitted each one of the above rt relations to the one of the silicon telescope (ODYSSEUS) using a linear transformation. In Figure 5.16 the rt relation of one of our tubes, before and after the fit, is plotted together with the rt relation measured by ODYSSEUS. By dividing the area 2 mm < r < 13 mm into 60 bins, we obtain the initial time value for each one of them (t_{ini}). Consequently we minimized the following function:

$$\chi^2 = \sum_{i=1}^{N} = (t_{ini} - t_{corr})^2 \qquad (5.7)$$

where $t_{corr} = a \cdot t_{odys} + b$, t_{odys} is the time value of the specific bin given by the rt relation determined by the silicon telescope and N is the number of bins between 2 and 13 mm. After this fitting procedure the two parameters a (scale parameter) and b (time offset) are defined. The adjustment of these two parameters corresponds to an adjustment of the t_0 parameter too. Therefore the t_0 was finally determined with the

above procedure with an accuracy of about 300 ps (as derived from simulation studies that will be described in the next chapter). Figure 5.17 shows how the asymmetry of the residuals left and right of the wire of one of the tubes disappears after calibrating the wire positions.
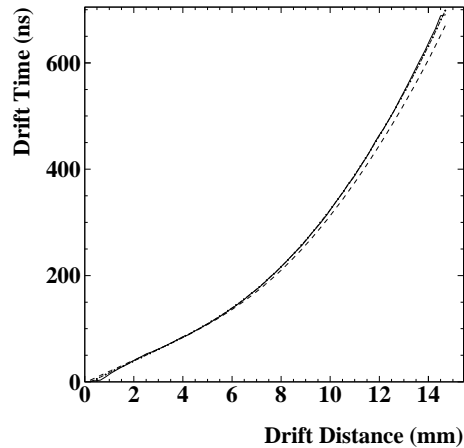
Figure 5.16: *The dashed line is the rt relation measured with ODYSSEUS. The solid line is the rt relation for one of the tubes before the fit. The dot-dashed line is the rt relation of the same tube after the fit and it is not very visible as it almost overlays with the solid line.*
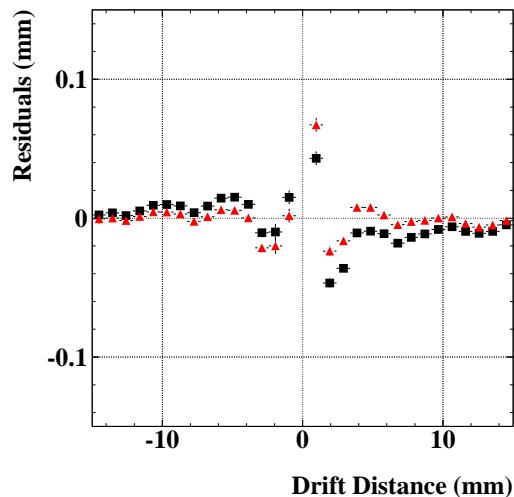
Figure 5.17: *Residuals left and right of the wire versus the drift distance for a tube while the chamber was filled with the baseline gas Ar/CO_2 (93/7). The black rectangles are the residuals before finding the wire positions and the red triangles correspond to the residuals after the calibration of the wire positions.*

The distribution of the wire displacements found with this adjustment has an rms of 16 μm (compatible again with the mechanical accuracy of the chamber) (Figure 5.18). It should be mentioned also that these wire displacements are the same as those obtained while each tube had its own rt relation. Comparison with the X-ray measurements of the new wire coordinates shows again a good correlation (Figure 5.19) and agreement within 10 μm rms (Figure 5.20) [CHO00].
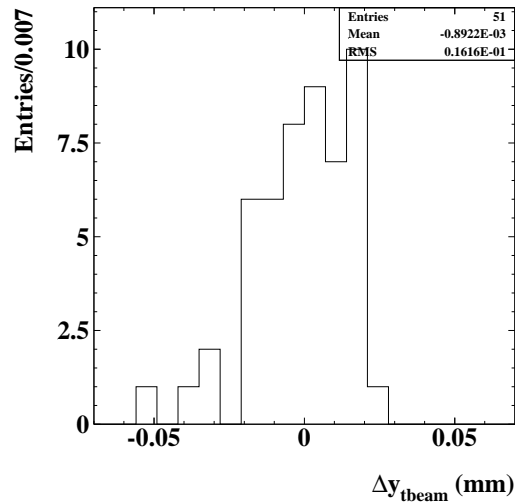
Figure 5.18: *Wire displacements in the y direction with respect to the ideal wire grid for the 51 tubes of six flower pairs (data 1999). The rms of the distribution (16 μm) is again in agreement with the required mechanical accuracy of the chamber (20 μm).*
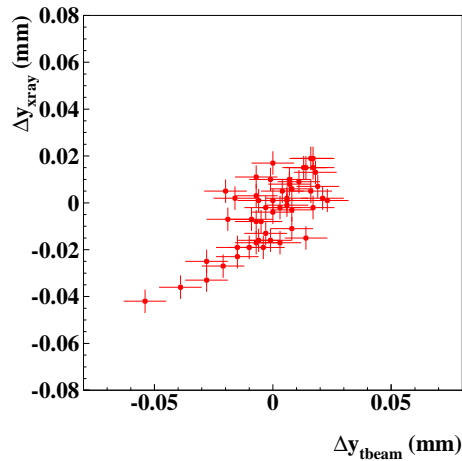
Figure 5.19: *The displacements of the y coordinates of the wire positions from their nominal positions for the 51 tubes measured by the X-Ray tomograph (Δy_{xray}) versus the corresponding displacements (Δy_{tbeam}) found with the method discussed. The error bars are the same like those in Figure 5.11.*
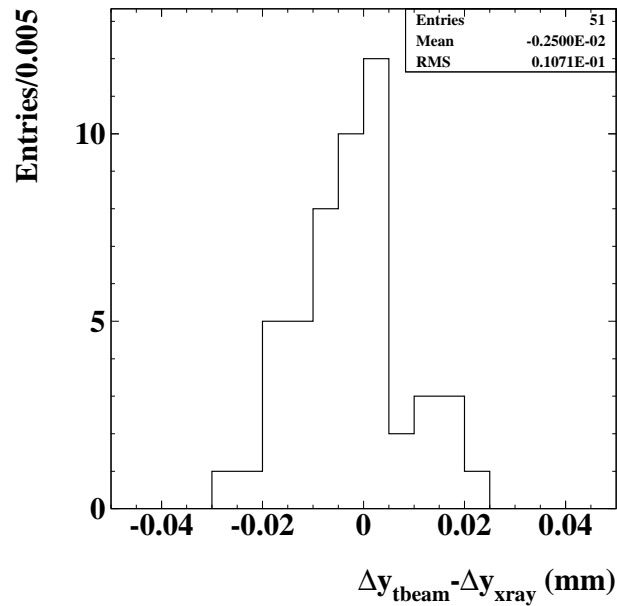
Figure 5.20: *The distribution of the difference Δy_{tbeam}-Δy_{xray}. The rms of the distribution is about 11 μm.*

5.3   Summary

Using the data taken with one of the first full scale MDT prototypes during the 1998 testbeam period, while the chamber was filled with the former ATLAS baseline gas $Ar/N_2/CH_4$ (91/4/5), the relative wire positions (in the y direction) for a group of twelve tubes were found using a wire calibration method that needs no external reference frame. The accuracy of the method was better than 10 μm as derived from a comparison of these results with those of the X-ray tomograph at CERN. The success of these studies was repeated the following year by finding the wire positions of fifty-one tubes of the same prototype chamber; this time the chamber was filled with the new baseline gas Ar/CO_2 (93/7).

Having proven the success of the wire calibration method for more tubes, the simulation studies in order to identify its statistical and systematic effects, when applied along the full width of a chamber, was the final step and I am discussing them in the next chapter.

Chapter 6

Simulation studies of the calibration method

After the successful results of the wire calibration method described in the previous chapter, simulation studies of its application along the whole width of a chamber were performed. Moreover the combination of the information from the individual flower pairs, as it will be described in this chapter, can provide a more complete testing of the mechanical accuracy of the chamber. The systematic and statistical effects of the method that are introduced by different factors are also presented.

6.1 Simulation for individual flower pairs of a chamber

For a simulated chamber filled with Ar/CO_2 (93/7) and having wire displacements of 20 μm rms in the y direction (Figure 6.1), muon tracks perpendicular to the chamber using a GEANT [GEA93] based simulation program (MTGEANT [KOR00]) were produced. GEANT is a system of detector description and simulation tools that help particle physicists to design and optimize the particle detectors, develop and test the reconstruction and analysis programs and interpret their experimental data. The energy of the muons produced was 180 GeV.

Along the whole width of the chamber (72 tubes per layer) there are 70 overlapping groups of 14 tubes (flower pairs). From the many thousands muon tracks produced during the simulation we used 25000 for each flower pair. After applying the method to all of these 70 flower pairs, the local displacements, that is the relative displacements of the wires within a flower pair, were measured.

At this point it is necessary to describe how the comparison between the displacements of the wires found with this method and the generated ones was made. In Figure 6.2 the reference frame (y,z) of the simulated perfect grid of the wires of one flower pair of the chamber is shown. The nominal positions of the tube wires are represented

as black points. Perfect grid means that all the y pitches (separation between two successive wires in the y direction) are equal to 30.036 mm while all the z pitches are equal to 26.054 mm. The distance between the two middle layers of the chamber is 399.07 mm. The distances in this Figure are not in scale.
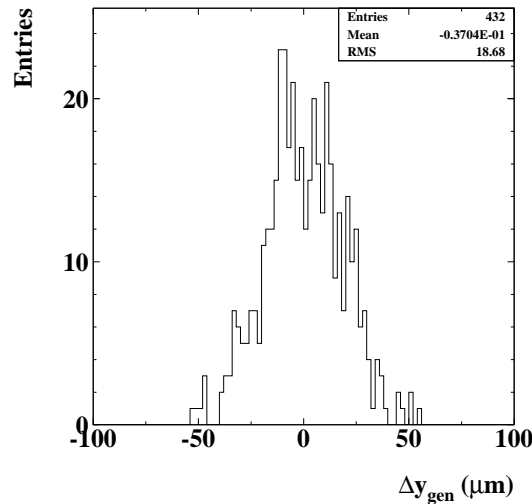
Figure 6.1: *The generated displacements with an rms of about 20 μm of all the 432 wires of a whole chamber.*

In the wire calibration method the wire positions of the two central tubes in the two middle layers are kept fixed (assuming that they coincide with the positions of the perfect grid). The displacements of the surrounding wires that are found, express the relative positions of these wires with respect to the real positions of the central ones. By keeping the two central wires fixed (whose positions in reality are not those of the perfect grid as assumed - they are also displaced) we define a new local reference frame within every flower pair. Therefore the displacements in the perfect grid reference frame should be transformed into displacements in the local flower reference frame. After this transformation the comparison between the (transformed) generated and measured displacements can be performed.

Coming back to Figure 6.2, we illustrate a simple example of the transformation between the two reference frames mentioned (using numbers for clarification). Suppose that only the wire of one of the two central tubes (tube 2) is displaced by 30 μm in the y direction. The line that connects the two central wires defines the direction of the z' axis of the rotated local flower reference frame. The axes of the rotated frame y' and z' are also indicated. Because the displacement of tube 2 is so small (in the order of microns) the angle θ is also very small ($\theta = 0.75 \cdot 10^{-5}$ $^{o} \simeq 0$ ^{o}).
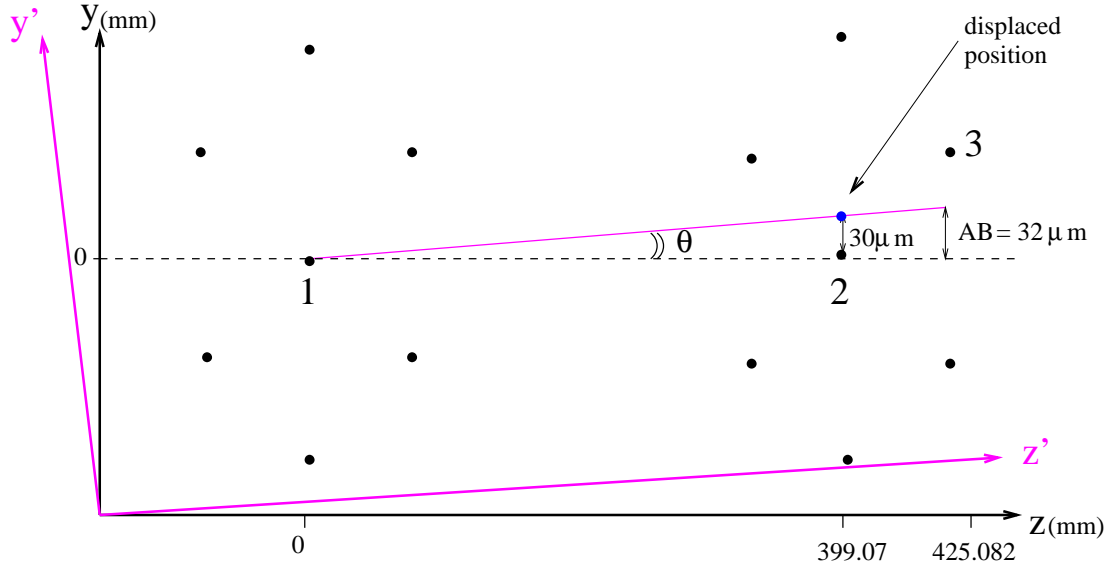
Figure 6.2: *The perfect grid reference frame (y,z) and the rotated local flower frame (y',z'). The black points are the nominal positions of the wires of one flower pair in the (y,z) frame. The blue point close to wire 2 indicates its displaced position in the y direction.*

Given that the coordinates of tubes 2 and 3 are (y_2, z_2) and (y_3, z_3) respectively, their corresponding coordinates (y_i', z_i') (i = 2, 3) in the rotated frame by angle θ will be:

$$y_2' = -z_2 sin\theta + y_2 cos\theta, \qquad y_3' = -z_3 sin\theta + y_3 cos\theta \qquad (6.1)$$

$$z_2' = z_2 cos\theta + y_2 sin\theta, \qquad z_3' = z_3 cos\theta + y_3 sin\theta \qquad (6.2)$$

By replacing $sin\theta = \theta$, $cos\theta = 1$ ($\theta \simeq 0^o$), $z_2 = 399{,}07$ mm, $y_2 = 0.03$ mm, $z_3 = 425.082$ mm and $y_3 = 15.018$ mm (as defined by the perfect grid) we find:

$$y_2' = -0.03 + 0.03 = 0\ mm, \qquad y_3' = -0.032 + 15.018 = 14.986\ mm \qquad (6.3)$$

$$z_2' \simeq z_2 \qquad z_3' \simeq z_3 \qquad (6.4)$$

Equation 6.4 denotes that AB can be considered parallel to the y axis. As the y pitch is equal to 30.036 mm, the distance between wire 2 and wire 3 is:

$$\frac{y_{pitch}}{2} = \frac{30.036}{2} = 15.018\ mm \qquad (6.5)$$

From the second equation in 6.3, it is obvious that the wire 3 will be displaced from its nominal position in the rotated frame by

$$AB = 14.986 - 15.018 = -0.032 \, mm \tag{6.6}$$

The minus sign in the above equation denotes that the wire 3 is closer than the nominal distance to the wire 2. In reality the wire 3 has generated displacement equal to zero but wire 2 has generated displacement equal to 0.030 mm. Our method measures the real relative positions between the fixed tubes and the surrounding ones. Therefore as we keep the wire 2 fixed at position y = 0.0 we will measure that the wire 3 is displaced and is closer to the wire 2 by about 0.032 mm. The displacement that is found with the method, should be compared with the displacement AB of the wire 3 in the rotated frame.

After the correspondence between each reference flower frame of the whole chamber and the perfect grid one is found, the displacements of the wire positions measured with our method were compared to the generated ones (Figure 6.3(a)). This comparison revealed a local accuracy of the method in the order of 5 μm (Figure 6.3(b)). Statistical and systematic components of this accuracy will be investigated in the following sections.

(a)

(b)
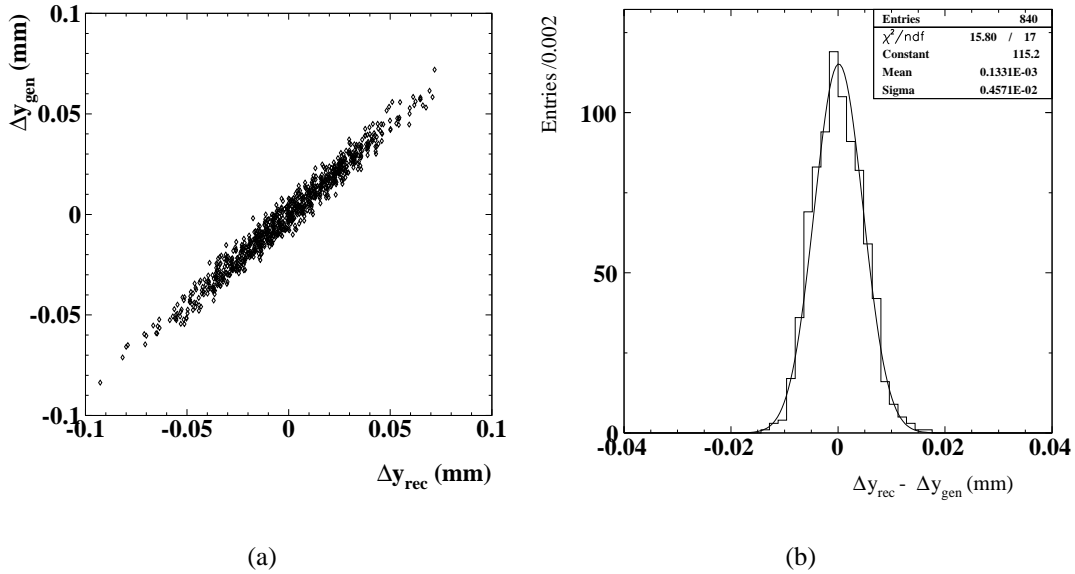
Figure 6.3: *(a) The generated displacements of the y coordinates of the wire positions from their nominal positions for the tubes of one simulated chamber (Δy_{gen}) versus the corresponding displacements (Δy_{rec}) recalculated with the method discussed. (b) The distribution of the difference Δy_{rec}-Δy_{gen} for fixed t_0=0 ps. There are double entries for all tubes of the chamber as the flower pairs measured are overlaid.*
(No of entries = (70 flower pairs) × (12 measured wires) = 840). The distribution has a σ of about 5 μm.

This precision is by a factor two better than the one we obtained using the testbeam data. The reason is that the t_0 parameter was kept equal to zero in the simulation. In reality this is not the case. This parameter can be determined with an accuracy of 200-300 ps for individual tubes [RAU01]. Therefore, we introduced to the drift time spectra of the tubes, Gaussian distributed t_0 offsets of an rms of 200 and 300 ps as it will be described in the next section.

6.1.1   Systematics due to t_0

After introducing to the drift time spectra of all the tubes of the simulated chamber, Gaussian distributed t_0 offsets of an rms of 200 ps the local uncertainty increased to 8 μm (Figure 6.4a). When these offsets had an rms of 300ps the local uncertainty became 9 μm. In Figure 6.4b the local accuracy dependence on the spread of the t_0 values is presented.

(a)   (b)
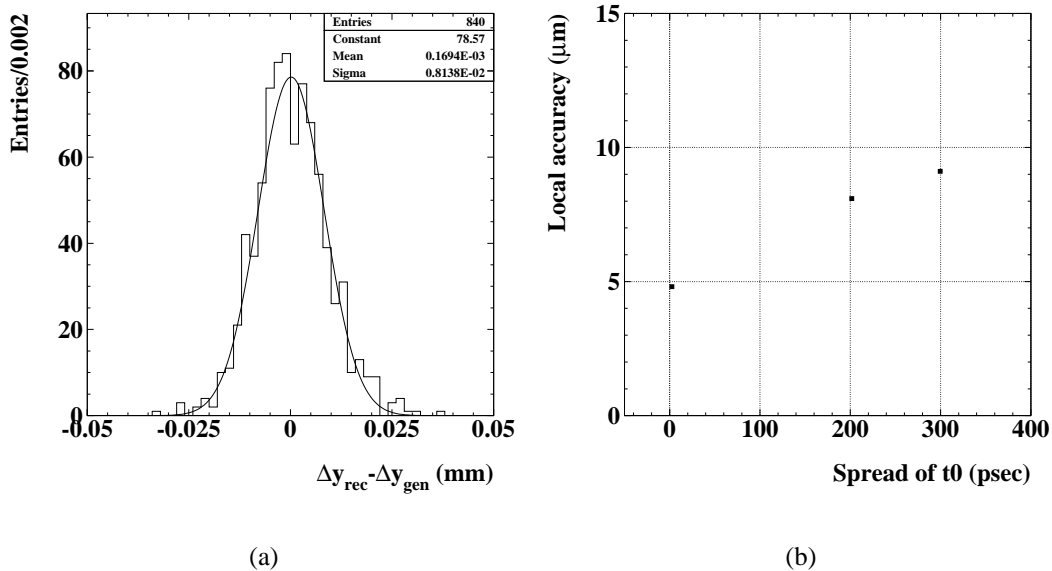
Figure 6.4: *(a) The distribution of the difference Δy_{rec}-Δy_{gen} when the t_0 has a Gaussian distribution with a width of 200 ps, (b) the local accuracy dependence on the spread of t_0.*

The main reason for this effect is the presence of the half illuminated tubes in the two middle layers for each flower pair. For these half illuminated tubes we use only tracks that pass either right or left from their wires, so the distribution of their residuals versus the drift distance has only one branch and not two (Figure 6.5).

When the t_0 changes the two branches of the fully illuminated tubes are moved together either up or down. The distance between them though stays the same. In the

case of the half illuminated tubes, their one branch again is moved up or down but we do not have any information for the second branch. We can not determine the distance between the two branches for these tubes and consequently the information for the wire displacement that is expressed with the distance between the two branches is inevitably partly lost. According to our method the single branches of the half illuminated tubes are just aligned along the line that corresponds to residual values equal to 0 (see the two last terms of the minimization function in equation 5.5).
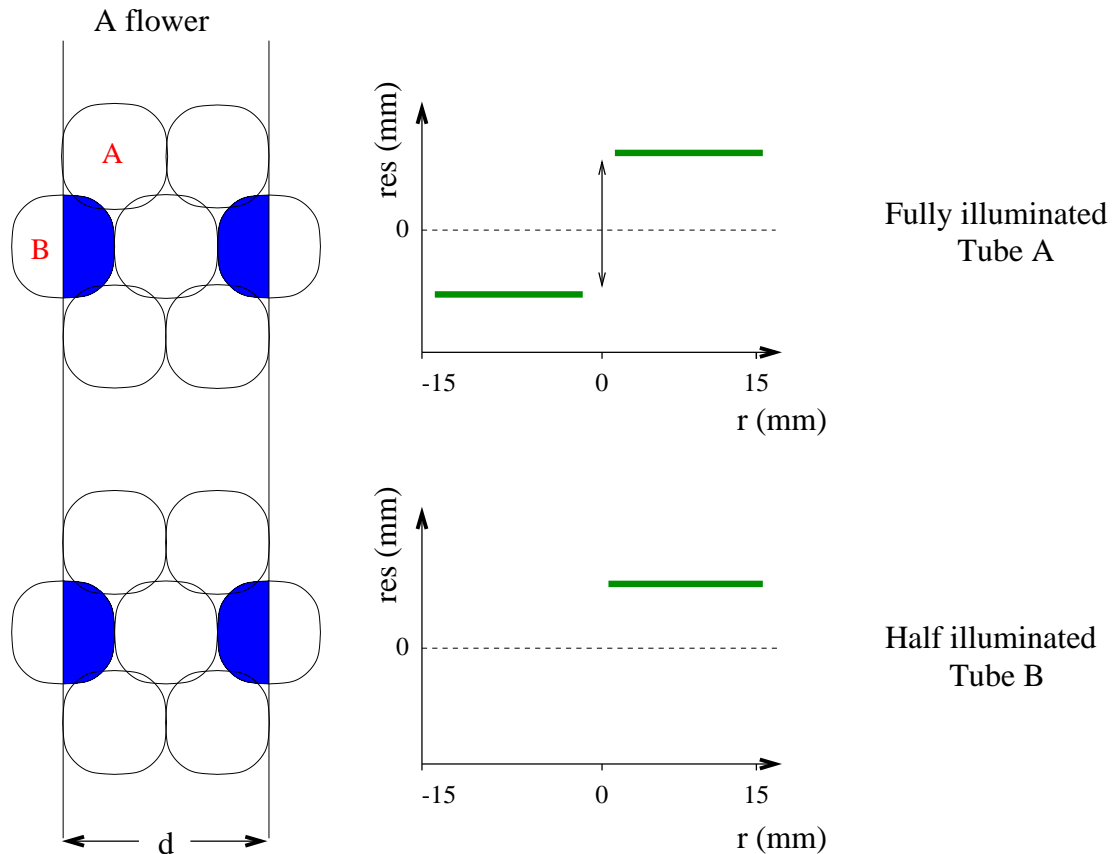
Figure 6.5: *On the left, a flower pair of tubes is shown; d indicates the area whose tracks we use for this flower pair. This has as a result that four tubes(indicated in blue) in the flower pair are half illuminated with tracks. On the right of the figure the residuals versus the drift distance for the fully illuminated tube (A) as well as for the half illuminated one (B) are shown. The tube A has two residual branches but the tube B has only one.*

6.1.2 Statistical effects

As it was previously mentioned, for the studies in sections 6.1 and 6.1.1, we used 25000 muon tracks per flower pair. In order to separate statistical and systematic precision of our method, it was necessary to examine its local accuracy by using different number of tracks. The local accuracy dependence on the number of tracks used is shown in Figure 6.6 for the case that the t_0 was kept equal to 0 and when it had Gaussian distributed values with a width of 200 ps. The error bars of the points express the standard error of the mean value of the accuracy that was obtained by repeating the analysis with several subsamples of the specific number of tracks. It is obvious that for more than 10000 tracks a plateau is reached while for smaller numbers of tracks the local accuracy starts to deteriorate and reaches 11 μm and 13 μm for 1000 tracks for t_0=0 and a spread of t_0 equal to 200 ps respectively.
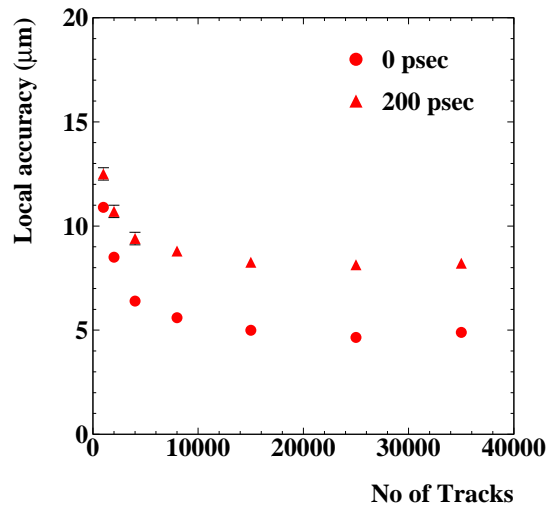
Figure 6.6: *The local accuracy dependence on the number of tracks used per flower pair. The circles correspond to the case where the t_0 was kept equal to 0 whereas the triangles represent the case of t_0 spread with a width of 200 ps. The error bars visible in this Figure are less than 0.5 μm whereas for the other points they are too small to be represented.*

We can conclude that in order to use the full potential of the method a total number of more than 10000 tracks should be used per flower pair. Such a number of tracks can be obtained in real LHC conditions in about 2-3 hours of run.

6.2   Combining information from all flower pairs

The next step was to combine the information of the 70 flower pairs acquiring the wire positions not within a flower pair but within the whole chamber. We tried three different ways of combinations. The more successful one, as well as its later improvement, are described below.

We start combining from the first central wire (in the middle layer of a multilayer) on the left side of the chamber as shown in Figure 6.7. We assume that this wire (1) is fixed at its nominal position of the perfect grid reference frame of the chamber. Using the local information of the first two overlapping flowers, we average the two measured distances between the wire 1 and the wire 2. For example the distance d_{21} of the wire 2 from the wire 1 is:

$$d_{21} = y_{pitch} + \frac{dy_1 + dy_2}{2} \tag{6.7}$$

where y_{pitch} is the nominal y pitch and dy_1 is the displacement of the wire 2 from its nominal position as measured in the green flower and dy_2 is the same displacement as measured in the magenta flower. In this way the position of the wire 2 with respect to the wire 1 is calculated. Subsequently we use again the local information of the next overlapping pair of flowers finding the position of the wire 3 with respect to the wire 2. Repeating this procedure along the full width of the chamber we obtain at a first stage all the wire positions of the middle layer of the multilayer.
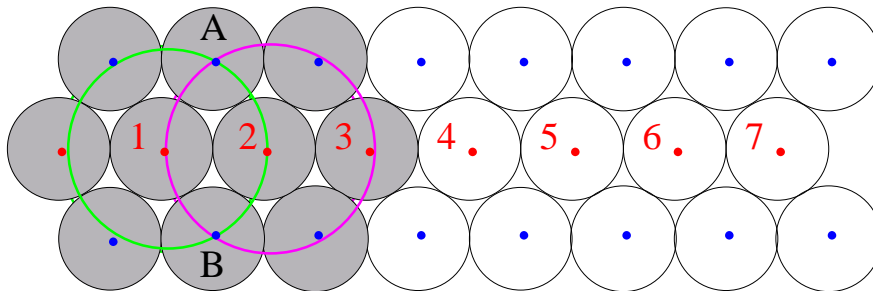
Figure 6.7: *Part of one multilayer of the chamber is shown. The first overlapping flower is indicated with a green circle while the second one with a magenta one. In a first step while combining the local information, the positions of the wires (2, 3, 4, etc) of the middle layer with respect to the first wire (1) are found. The measuring of the positions of the wires A and B follows. Iteration of this procedure along the chamber results in the calculation of the absolute positions of all wires with respect to the first one.*

The position of the wires A and B (shown in the same Figure) with respect to the wire 1 are found by averaging again the local information given by the first pair of

overlapping flowers. Iterating along the whole chamber we obtain the absolute positions of all the wires with respect to the first central wire (y_{cor}).

During this iteration of combining local measurements the problem which arises is the fact that the errors are added up along the chamber. Therefore the further is one tube from the first central tube, the worse its position accuracy gets. We tried to solve this problem by minimizing the following function G:

$$G = \sum_{i=1}^{N} (y_{fit_i} - y_{nom_i})^2, \tag{6.8}$$

where $y_{fit_i} = a_1 \cdot y_{cor_i} + a_2$, while N is the number of the wires in one multilayer, y_{nom_i} is the nominal position of the wire (perfect grid), a_1 is a correction parameter that scales the average distance between two successive wires and a_2 is a second correction parameter that accounts for the shift of one multilayer. The absolute positions of the wires with respect to the whole chamber that we acquired with this procedure in the case where the drift time spectra had Gaussian distributed t_0 offsets of an rms of 200 ps are shown in Figure 6.8; the global accuracy is in the order of 20 μm.

Assuming random and uncorrelated wire displacements, to get the absolute wire positions with respect to the whole chamber, only a small surrounding of each wire is needed. Therefore we select an area of 33 tubes (10 flowers) around each wire and we determine the shift and scale parameters (a_1, a_2) for this specific wire by minimizing this function:

$$G = \sum_{i=1}^{33} (y_{fit_i} - y_{nom_i})^2, \tag{6.9}$$

The global accuracy now improves to 10 μm as can been seen in Figure 6.9a (where $\sigma(t_0)$= 200 ps). The results obtained for the global accuracy while using different t_0 offsets are presented in Figure 6.9b. This local determination of the shift and scale parameter is justified if one wants to test whether individual tubes are at their nominal position with respect to the surrounding tubes.
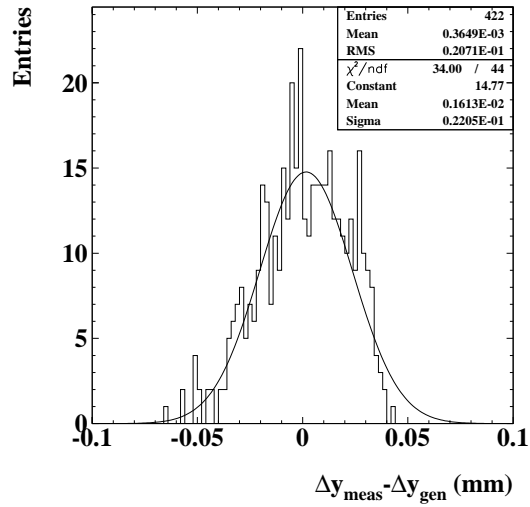
Figure 6.8: *Determination of the absolute wire position distribution with respect to the whole chamber for a t_0 spread of 200 ps.*

(a)   (b)
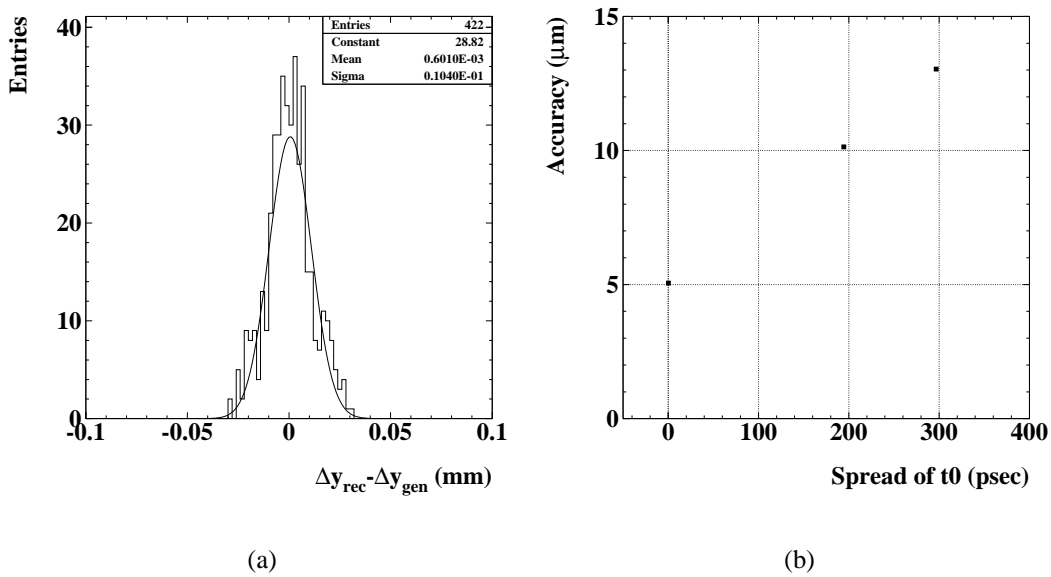
Figure 6.9: *(a) When a small surrounding of the wire to be measured is used, the global accuracy improves to 10 μm for a t_0 spread of 200 ps, (b) the global accuracy dependence on the spread of t_0.*

6.2.1 Statistical effects

The global accuracy dependence on the number of tracks used per flower pair assuming random and uncorrelated wire displacements (fit function of equation 6.9) was also studied (for t_0=0 and spread of t_0 equal to 200 ps) and is presented in Figure 6.10. The plateau of constant global accuracy is reached again for about 10000 tracks per flower pair.
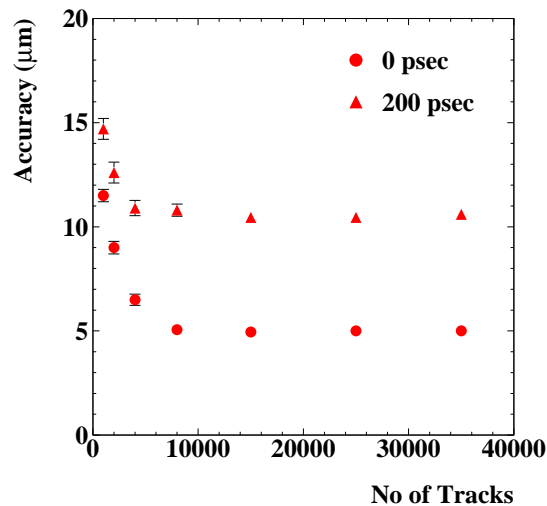
Figure 6.10: *The global accuracy dependence on the number of tracks used per flower pair. The circles correspond to the case where the t_0 was kept equal to 0 whereas the triangles represent the case of t_0 spread with a width of 200 ps. The error bars express again the standard error of the mean value of the accuracy that was obtained by repeating the analysis with several subsamples of the specific number of tracks. At the points where the standard error of the mean is too small (less than 0.2 μm), no error bars are plotted.*

6.3 Summary

Simulation studies of the application of the wire calibration method along the whole width of an MDT chamber in order to identify its systematic and statistical effects were performed. The chamber consists of 70 overlapping flower pairs. By using 25000 tracks per flower pair and keeping the t_0 for all the tubes equal to 0, the accuracy of the method in measuring wire displacements in the y direction within each flower pair (local accuracy) is 5 μm. By introducing Gaussian distributed t_0 offsets of an rms of 200 and 300 ps to the drift time spectra of the tubes, this local uncertainty increases to

8 and 9μm respectively.

By combining the information of the 70 flower pairs we acquired the absolute wire positions within the whole chamber with respect to the first central wires within each multilayer. These absolute wire positions that we obtained in the case where the drift time spectra had Gaussian distributed t_0 offsets of an rms of 200 ps, were measured with an accuracy of 20 μm (global accuracy). Assuming though random and uncorrelated wire displacements, to get the absolute wire positions with respect to the whole chamber, only a small surrounding of each wire is needed. Therefore by slightly modifying the combination procedure of all the 70 flowers the global accuracy improves to 10 μm ($\sigma(t_0) = 200$ ps).

Application of the method on the 70 overlapping flower pairs of one chamber using different number of tracks showed that in order to exploit the full potential of the method a total number of more than 10000 tracks per flower pair should be used.

The simulation studies proved that the wire calibration method can be used successfully in muon test beam conditions where the muons have an energy of 180 GeV or more. Using this method we can perform a very accurate test of the mechanical accuracy of MDT chambers. Moreover, wires that have large displacements and that could spoil the tracking procedure, can be very well identified and calibrated.

Another application of the method will be its use in the data analysis of the ATLAS cosmic ray set-ups, like the one that has already been built at LMU in Munich for the commissioning and calibration of the chamber production at MPI Munich. Of course more studies would be needed in this case as the energy of the cosmic rays is different than this of the test beam resulting in multiple scattering of the muons in the chamber material that could be a limiting factor on the performance of the method.

The wire calibration method described in the last two chapters, could offer a possibility for online calibration of the wire positions of the MDT chambers in the final set-up of the ATLAS detector. An extension of the method could reveal its potential in finding wire displacements also in the z direction. For such studies, tracks that form an angle with the chamber should be used.

Chapter 7

Neutralino Decays in ATLAS

The Standard Model (SM) describes successfully the fundamental interactions (electromagnetic, weak and strong) of elementary particles at the smallest scales and highest energies accessible to current experiments. Nevertheless, it cannot be considered to be the ultimate theory of Nature because it can not provide answers to many questions. The SM is a work in progress and will have to be extended to describe physics at arbitrarily high energies. In this chapter, one of the best motivated extensions of the SM (Supersymmetry or SUSY) is briefly presented. The lightest supersymmetric particle in the most favourable supersymmetry models is the lightest neutralino. Simulation studies of the next-to lightest neutralino decays in ATLAS in certain areas of the SUSY parameter phase space will be described. Moreover, the effect of the very resent simulation implementations of the spin-averaged matrix element in the three-body decays of the second neutralino will be discussed.

7.1 Motivation for extending the Standard Model

The Standard Model [SM61] is based on a gauge principal according to which all the forces of Nature are mediated by an exchange of the gauge fields of the corresponding local symmetry group. The symmetry group of the SM is

$$SU_{colour}(3) \otimes SU_{left}(2) \otimes U_Y(1) \tag{7.1}$$

The $SU_{colour}(3)$ is the group of color symmetry of the strong interactions (the quarks come in three colors). The remaining part of equation (7.1) expresses the symmetry group of the electroweak interactions where the $SU_{left}(2)$ part couples only to left handed fermions and the $U_Y(1)$ part couples to left and right handed fermions.

In the minimal version of the SM there is one doublet of complex scalar Higgs fields, which is introduced in order to give masses to quarks, leptons and the intermediate weak bosons via the spontaneous breaking of the electroweak $SU_{left}(2)$ symmetry.

The SM has been extraordinarily successful; the achieved accuracy of its predictions corresponds to experimental data within 5% [PDG00]. All the particles, except for the Higgs boson, have been discovered experimentally. However, the SM has its natural drawbacks and unsolved problems. The answer to these problems (some of them are listed below) lies beyond the SM and is the task of the Grand Unified Theories (GUTs) [LAN81]. In GUTs the known electromagnetic, weak and strong forces are combined into a single theory. Therefore, at very high energies ($M_{GUT} \sim 10^{16}$ GeV) all forces are equally strong.

Among the problems that the GUTs are addressed to solve are the following:

- What is the origin of mass and the origin of matter?

- What is the origin of the Matter-Antimatter Asymmetry in our universe?

- What is the origin of dark matter, which seems to provide the majority of mass in our universe?

- Why are there so many free parameters in the SM?

- The mechanism of electroweak symmetry breaking is still unclear.

- Why are there three independent symmetry groups?

- Why are there three generations of quarks and leptons?

- Why is the weak scale so small compared with the GUT scale, i.e why is $M_W \sim M_{GUT} 10^{-14}$?

- The fine-tuning problem: radiative corrections to the Higgs masses and gauge boson masses have quadratic divergences. The corrections to the Higgs masses are many orders of magnitude larger than the masses themselves, since they are expected to be of the order of the electroweak gauge boson masses. This requires extremely unnatural fine-tuning in the parameters of the Higgs potential.

The two directly testable predictions of the simplest GUT theory, namely

- the finite lifetime of the proton

- and the unification of the three coupling constants of the electroweak and strong forces at high energies

turned out to be a disaster for simple GUTs. The proton was found to be much more stable than predicted and from the precisely measured coupling constants at the LEP collider at CERN in Geneva, one had to conclude that the couplings did not unify, if extrapolated to high energies [ELL91].

However, it was shown later, that by introducing a symmetry, called Supersymmetry (SUSY) [SUS71], into the Standard Model, both problems disappeared: unification was obtained and the prediction of the proton life time could be pushed above the present experimental lower limit! In the next sections, the main characteristics of SUSY as well as its theoretical achievements are presented.

7.2 What is SUSY?

Supersymmetry is a purely theoretical invention and one of the best motivated extensions of the SM. It has not yet been observed in Nature. Its validity in particle physics follows from the common belief in the unification of the forces.

SUSY is a generalization of the space-time symmetries of quantum field theory that transforms fermions into bosons and vice versa. That is, every known elementary particle has a supersymmetric partner, or superpartner, which is like it in all respects except for its spin. Spin-$\frac{1}{2}$ fermions, leptons and quarks have spin-0 superpartners, while spin-1 bosons, like the photon, have spin-$\frac{1}{2}$ superpartners.
If Q is a generator of SUSY algebra, then

$$Q|boson> = |fermion>, \quad Q|fermion> = |boson> \tag{7.2}$$

Hence, starting with a state of spin 2 (graviton) and acting by SUSY generators we get the following chain of states:

$$\text{spin2} \rightarrow \text{spin 3/2} \rightarrow \text{spin1} \rightarrow \text{spin1/2} \rightarrow \text{spin 0}.$$

The fact that SUSY relates particles with the same mass and other quantum numbers differing by $\pm 1/2$ unit of spin results from its supersymmetric algebra. Attempts to unify all four forces of Nature within the same algebra face a problem as the graviton has spin 2 while the other gauge bosons (photon, gluons, W and Z bosons) have spin 1 [COL67]. The supersymetric algebra solves this problem. Thus SUSY provides a promising ingredient to the unification of particle physics and gravity, which is governed by the Planck scale ($\sim 10^{19}$ GeV), the energy scale where the gravitational interactions of elementary particles become comparable to their gauge interactions (electroweak and strong).

As it has already been mentioned, an important motivation for SUSY is related with the unification theory. According to this theory all known interactions are different branches of a unique interaction associated with a simple gauge group. At first sight this is impossible due to a big difference in the values of the couplings of strong, weak and electromagnetic interactions. However this is not so. The crucial point here is the fact that these coupling constants are 'running'. This means that the couplings are functions of the distance or the energy scale. This dependence is described by the

renormalization group equations (RGE).

Assuming that the SM is valid up to the unification scale, one can then use the RGE for the three couplings. The result is demonstrated in Figure 7.1a showing the evolution of the inverse of the couplings as a function of the logarithm of energy. This Figure clearly demonstrates that within the SM the coupling constant unification at a single point is impossible. This weakness of the SM can be overcome by SUSY. In the SUSY case, the slopes of the renormalization group evolution curves are modified so that they meet finally at a single point (Figure 7.1b). This perfect unification can be obtained if the masses of the sparticles are of an order of $M_{SUSY} \sim 1$ TeV [AMA91].

(a)   (b)
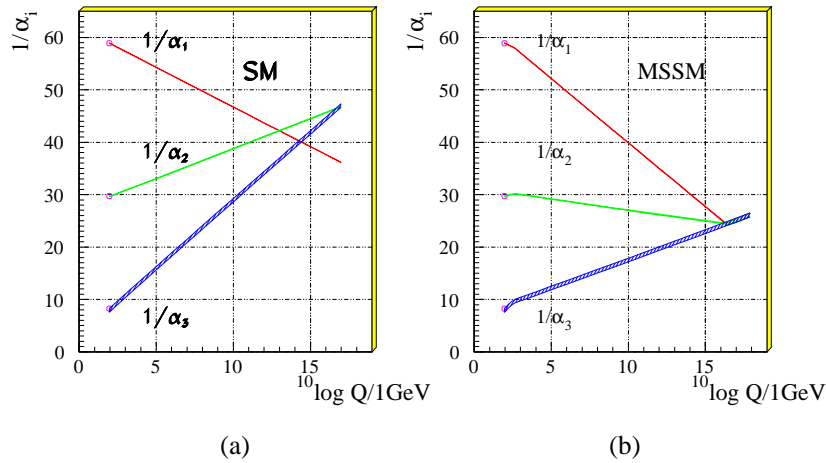
Figure 7.1: *(a) Evolution of the inverse of the three coupling constants in the Standard Model and (b) in the supersymmetric extension of it (MSSM, see section 7.3). Only in the latter case unification is obtained.*

SUSY offers also a possible explanation of the so called hierarchy problem. There are two aspects of this problem. The first one is the fact that the electroweak scale (M_W) and the unification scale (M_{GUT}) are so different. The ratio between these two scales is extremely small:

$$\frac{M_W}{M_{GUT}} = 10^{-14} \tag{7.3}$$

SUSY provides the fine tuning that is needed in order to get such a small number in a natural way: large radiative corrections from the top-quark Yukawa coupling to the Higgs sector drive one of the Higgs masses squared negative, thus triggering electroweak symmetry breaking. Since radiative corrections are logarithmic in energy, this automatically leads to a large hierarchy between the scales.

The second aspect of the hierarchy problem is connected with the preservation of a given hierarchy. Even if we choose the hierarchy like equation 7.3, the radiative corrections will destroy it. In order to illustrate this effect, let us consider the radiative corrections to the light Higgs mass due to a heavy particle. These corrections turn out to be in the order of the M_{GUT} scale and obviously they spoil or even cancel the hierarchy. A very accurate cancellation of these large corrections with a precision of $\sim 10^{-14}$ is needed. The only known way of achieving this kind of cancellation (also known as cancellation of the quadratic divergencies) is supersymmetry. In SUSY these loop corrections contain both fermions and bosons, which according to the Feynman rules contribute with an opposite sign. Therefore the contribution from boson loops cancels those from the fermion ones. This cancellation is true in the case of unbroken supersymmetry and it is true up to the SUSY breaking scale (M_{SUSY}), which should not be very large to make the fine-tuning natural.

For all the above possible answers that SUSY can offer to our present questions we have to pay the price of the doubling of the number of elementary particles, since SUSY presupposes a symmetry between fermions and bosons. This symmetry though is not an exact symmetry of Nature. If it was, then the superpartners would have the same mass as their partners and they would have been detected easily long time ago. But this is not the case. No supersymmetric particle has yet been detected. Thus, supersymmetry must be a dynamic symmetry not manifest in the observed ground states of Nature at low energy densities, i.e. a 'broken' symmetry. More details about SUSY breaking will be given in the next two sections. But SUSY particles, if they exist, should be observable in the next generation of accelerators, since their mass estimates, as it has been earlier mentioned, are in the TeV region.

7.3 Minimal Supersymmetric Standard Model (MSSM)

The Minimal Supersymmetric Standard Model (MSSM) is the supersymmetric extension of the Standard Model with the least number of additional new particles and R-parity conservation. R-parity is a multiplicative quantum number defined as

$$R = (-1)^{3(B-L)+2S} \tag{7.4}$$

where B, L and S are the baryon number, lepton number and spin respectively. This formula implies that all ordinary SM particles have even R-parity ($R = +1$), whereas the corresponding SUSY partners have odd R-parity ($R = $ -1). The conservation of R-parity in scattering and decay processes has a crucial impact on the supersymmetric phenomenology: SUSY particles must be produced in pairs and that the lightest SUSY particle (LSP) is absolutely stable.

The particle spectrum in the MSSM consists of two kinds of supermultiplets: vector supermultiplets for the gauge bosons and chiral supermultiplets for the matter fields.

These supermultiplets are listed in tables 7.1 and 7.2.

Names	spin 0	spin 1/2
squarks, quarks (x 3 families)	$(\tilde{u}_L \tilde{d}_L)$ $\tilde{u}_R$ $\tilde{d}_R$	$(u_L d_L)$ u_R d_R
sleptons, leptons (x 3 families)	$(\tilde{\nu} \tilde{e}_L)$ $\tilde{e}_R$	(νe_L) e_R
Higgs, higgsinos	$(H_u^+ H_u^0)$ $(H_d^0 H_d^-)$	$(\tilde{H}_u^+ \tilde{H}_u^0)$ $(\tilde{H}_d^0 \tilde{H}_d^-)$

Table 7.1: *Chiral supermultiplets in the MSSM. The squarks and leptons come in three generations.*

Names	spin 1/2	spin 1
gluino, gluon	$\tilde{g}$	g
winos, W bosons	$\tilde{W}^\pm \quad \tilde{W}^0$	$W^\pm \quad W^0$
bino, B boson	$\tilde{B}^0$	B^0

Table 7.2: *Vector supermultiplets in the MSSM.*

The names for the spin-0 partners of the quarks and leptons are constructed by prepending an 's', which is short for scalar. Thus they are called squarks and sleptons. The symbols for the squarks and sleptons are the same as for the corresponding fermion, but with a tilde used to denote the superpartner of a Standard Model particle. For example, the superpartners of the left-handed and right-handed parts of the electron Dirac field are called left- and right-handed selectrons and are denoted $\tilde{e}_L$ and $\tilde{e}_R$. It is important to mention that the subscripts L or R here do not denote helicity, since the squarks and sleptons have no spin. These labels just indicate in analogy to the non-SUSY particles, whether they are SU(2) doublets or singlets. While the chiral fermions of the SM must have the same mass by Lorentz invariance, their superpartners are scalars with separate masses; their mass eigenstates are mixtures of the left and right weak interaction states. This mixing is stronger in the third generation of particles, thus giving rise to the following mass eigenstates: $\tilde{t}_{1,2}, \tilde{b}_{1,2}, \tilde{\tau}_{1,2}$. In the SM the neutrinos are always left-handed, so the sneutrinos are denoted by $\tilde{\nu}$, with a possible subscript indicating which lepton flavor they carry $(\tilde{\nu}_e, \tilde{\nu}_\mu, \tilde{\nu}_\tau)$.

The names for the spin-1/2 partners of the SM gauge bosons are constructed by appending '-ino' to the name of the SM particle. For example, the fermionic partners

of the Higgs scalars are called Higgsinos. The symbols of the gauginos are the same as for the corresponding gauge boson, but again with a tilde (e.g. $\tilde{H}$ is the symbol for Higgsino).

The Higgs sector of the MSSM contains two doublets of complex fields:

$$\begin{pmatrix} H_u^+ \\ H_u^0 \end{pmatrix} \quad \text{and} \quad \begin{pmatrix} H_d^0 \\ H_d^- \end{pmatrix}$$

Hence there are eight degrees of freedom. As in the case of the SM, 3 degrees of freedom cause the masses of the Z and $W^\pm$ bosons, while the remaining five give rise to five physical Higgs bosons: a charged boson pair ($H^\pm$), two CP-even neutral bosons (H^0, h) and one CP-odd neutral boson (A).

7.3.1 SUSY breaking

SUSY must of course be broken, since superpartners have not been observed. In the general MSSM, supersymmetry breaking is accomplished by hand, that is by including in the Lagrangian the most general renormalizable soft-supersymmetry breaking terms consistent with the $SU(3) \times SU(2) \times U(1)$ gauge symmetry and R-Parity invariance. These soft terms are mass terms of all superpartners and Higgs-squark-squark and Higgs-slepton-slepton trilinear interaction terms (these are the so-called 'A parameters'). This effect results in the introduction of many new free parameters which actually parametrize our ignorance of the fundamental mechanism of supersymmetry breaking. There are a total of 105 new parameters in addition to the SM ones, thus the total number of truly independent parameters that the MSSM possesses is 124. Electroweak symmetry can not be broken by hand in a similar way, since this would destroy gauge invariance. In the SM masses can be introduced only by spontaneous symmetry breaking using the Higgs mechanism.

The addition of so many new parameters in the MSSM Langragian mentioned above, can not be arbitrary. For a better and more complete understanding of this, it is necessary to consider models in which SUSY is spontaneously broken and then it is transmitted to the MSSM by some mechanism.

Since none of the fields of the MSSM can develop non zero vacuum expectation value to break SUSY without spoiling the gauge invariance, it is supposed that spontaneous supersymmetry breaking takes place via some other fields. According to the most common scenario for producing low energy supersymmetry breaking, there exist two sectors: a 'hidden' sector consisting of particles, which lead to breaking of SUSY and are completely neutral with respect to the SM gauge group, and a 'visible' sector consisting of the particles of the MSSM. SUSY breaking is assumed to occur in the hidden sector and as these two sectors interact with each other by exchange of some

fields called messengers, the SUSY breaking is mediated from the hidden to the visible sector. There might be various types of messengers fields: gravity, gauge, etc. Therefore there exist different scenarios of SUSY breaking. The scenario where the messenger is gravity (mSUGRA) is discussed in section 7.4.

7.3.2   Neutralinos and charginos

Once SUSY and electroweak symmetry are broken, particles with the same quantum numbers will in general mix. Gauginos (winos and bino) and Higgsinos mix to form:

- two pairs of charged spin-1/2 particles, the charginos $\tilde{\chi}_i^{\pm}$ (i = 1, 2)

- four neutral spin-1/2 particles, the neutralinos $\tilde{\chi}_i^0$ (i = 1, 2, 3, 4)[1]

The chargino mass matrix is:

$$M^{(c)} = \begin{bmatrix} M_2 & \sqrt{2}M_W sin\beta \\ \sqrt{2}M_W cos\beta & \mu \end{bmatrix} \tag{7.5}$$

This matrix has two chargino eigenstates $\tilde{\chi}_{1,2}^{\pm}$ with mass eigenvalues:

$$\mathcal{M}_{1,2}^2 = \frac{1}{2}\left[M_2^2 + \mu^2 + 2M_W^2 \pm \sqrt{(M_2^2 - \mu^2)^2 + 4M_W^4 cos^2 2\beta + 4M_W^2(M_2^2 + \mu^2 + 2M_2\mu sin2\beta)} \right]$$

The neutralino mass matrix is:

$$M^{(0)} = \begin{bmatrix} M_1 & 0 & -M_Z cos\beta sin\theta_W & M_Z sin\beta sin\theta_W \\ 0 & M_2 & M_Z cos\beta cos\theta_W & -M_Z sin\beta cos\theta_W \\ -M_Z cos\beta sin\theta_W & M_Z cos\beta cos\theta_W & 0 & -\mu \\ M_Z sin\beta sin\theta_W & -M_Z sin\beta cos\theta_W & -\mu & 0 \end{bmatrix}$$
$$\tag{7.6}$$

The physical neutralino masses ($M_{\tilde{\chi}_i^0}$) are obtained as eigenvalues of this matrix after diagonalization. In the above mass matrixes $tan\beta = u_2/u_1$ is the ratio of two Higgs vacuum expectation values, θ_W is the weak mixing angle, μ is the Higgsino mass parameter and M_1, M_2 the wino ($\tilde{W}$) and bino ($\tilde{B}$) masses respectively. It is worthwhile mentioning that the third gaugino mass is this of the gluino (M_3).

It is difficult to quote rigorous experimental lower mass limits for the supersymmetric particles because they are extremely model dependent. The LEP experiments and SLD at SLAC excluded essentially all visible supersymmetric particles up to about half the mass of the Z boson. Current lower mass limits for the lightest neutralino ($\tilde{\chi}_1^0$) is about 42 GeV. A lower mass limit for the lightest chargino ($\tilde{\chi}_1^{\pm}$) of approximately 45

---

[1] The numbering of the $\tilde{\chi}_i^0$ is ascending with their mass.

GeV, independent of the field composition and of the decay mode, has been obtained by the LEP experiments from the analysis of the Z width and decays [PDG00].

In the MSSM framework, the lightest supersymmetric particle is the lightest neutralino ($\tilde{\chi}_1^0$). Since this neutralino is neutral and colorless, interacting only weakly with matter, is an ideal candidate for cold dark matter. The fact that supersymmetry provides cold dark matter is one of its major successes. According to the inflationary theory of the Big Bang, the dark matter makes up about 90% of the total mass in the universe and it has to be non-baryonic. The most impressive evidence for the dark matter comes from the so-called flat galaxy rotation curves [PRI88]. If neutralino LSPs really make up the cold dark matter, then their mass density in our neighborhood ought to be at least about 0.1 GeV/cm^3 in order to explain the rotation curves of galaxies. In principle, they should be detectable through their weak interactions with ordinary matter, or by their ongoing annihilations (in the galactic halo and in the center of the Earth and the Sun). An ambitious approach is being made by the Alpha Magnetic Spectrometer Experiment (AMS) [BAT98]. In November 2004, the AMS detector will be transported by the Space Shuttle to the International Space Station. One of the goals of this experiment is the detection of neutralino LSP annihilation products (positrons, antiprotons and γ rays).

7.4 Minimal Supergravity Model (mSUGRA)

As mentioned in section 7.3.1, the Minimal Supergravity Model [IBA82, ELL83] is a SUSY breaking scenario. In this case, the two sectors (hidden and visible) interact with each other via gravity.

The mSUGRA model assumes that at the GUT scale all scalars (squarks, sleptons and Higgs bosons) have a common mass m_0, all gauginos and Higgsinos have a common mass $m_{1/2}$ and all the trilinear Higgs-sfermion-sfermion couplings have a common value A_0. The 26 renormalisation group equations (RGE) [OHM94] are then solved iteratively starting from the GUT scale down to the weak scale. Because of the specific form of the RGE that take into account radiative corrections, the squared mass of the Higgs field is driven negative so that the Higgs potential develops a nontrivial minimum. This is the effect of the large top (and bottom) Yukawa couplings in the RGE. At this minimum the electroweak symmetry happens to be spontaneously broken while the color and electromagnetic interactions are left unbroken. The vacuum expectations of the Higgs fields acquire nonzero values and provide masses to quarks, leptons and gauge bosons, and additional masses to their superpartners. Thus, contrary to the SM, where one has to choose the negative sign of the Higgs mass squared 'by hand', in the MSSM the effect of spontaneous symmetry breaking is triggered by the radiative corrections.

In the mSUGRA approach, the MSSM-124 parameter freedom is sharply reduced to 23: 18 of them (excluding the Higgs mass) are the Standard Model parameters and the remaining five are the following:

- m_0 the common scalar mass,

- $m_{1/2}$ the common gauginos and Higgsinos mass,

- A_0 the trilinear Higgs-sfermion-sfermion couplings,

- $tan\beta$ the ratio of the two Higgs vacuum expectation values,

- $sign(\mu)$ the sign of the Higgsino mass parameter.

The masses of the two lightest neutralinos and the lightest chargino are determined by the $m_{1/2}$. The slepton masses are determined by m_0 and $m_{1/2}$. Hence, within mSUGRA the following relations are valid [INO82]:

$$M_{\tilde{\chi}_2^0} \approx M_{\tilde{\chi}_1^\pm} \approx 2M_{\tilde{\chi}_1^0} \approx (0.25 - 0.35)M_{\tilde{g}} \approx 0.9\, m_{1/2} \tag{7.7}$$

$$M_{\tilde{l}_L}^2 = m_0^2 + 0.52\, m_{1/2}^2 - 0.5(1 - 2\sin^2\theta_W)\, m_Z^2 \cos2\beta \tag{7.8}$$

$$M_{\tilde{l}_R}^2 = m_0^2 + 0.15\, m_{1/2}^2 - \sin^2\theta_W\, m_Z^2 \cos2\beta \tag{7.9}$$

where M denotes the mass of the corresponding particle which is indicated as an index.

7.4.1   mSUGRA parameter space points at LHC

The masses, mixings and decays of all SUSY and Higgs particles are determined in terms of the five mSUGRA parameters mentioned in the last section. Some representative masses are shown in Figure 7.2. The shaded regions in the figures are excluded by theory or experiment. The dots represent the five mSUGRA parameter space points selected by the LHC Committee (LHCC) in 1996 for detailed study by the ATLAS and CMS Collaborations. The parameters of the five LHCC points are listed in Table 7.3.

SUGRA phenomenology for $tan\beta \geq 10$ is more complicated because of the need to include additional Yukawa couplings and mixings in the $\tilde{b}$ and $\tilde{\tau}$ sectors. For this technical reason the five LHCC mSUGRA points were selected to have $tan\beta \leq 10$. There is, however, no reason to disfavour larger values of $tan\beta$. Therefore, a sixth point with large $tan\beta$ was added later by the ATLAS experiment for detailed studies. This point was selected so that the only two-body gaugino decays are $\tilde{\chi}_2^0 \rightarrow \tilde{\tau}_1\tau$ and $\tilde{\chi}_1^\pm \rightarrow \tilde{\tau}_1\nu$; these decays therefore dominate and give signatures involving τ's.
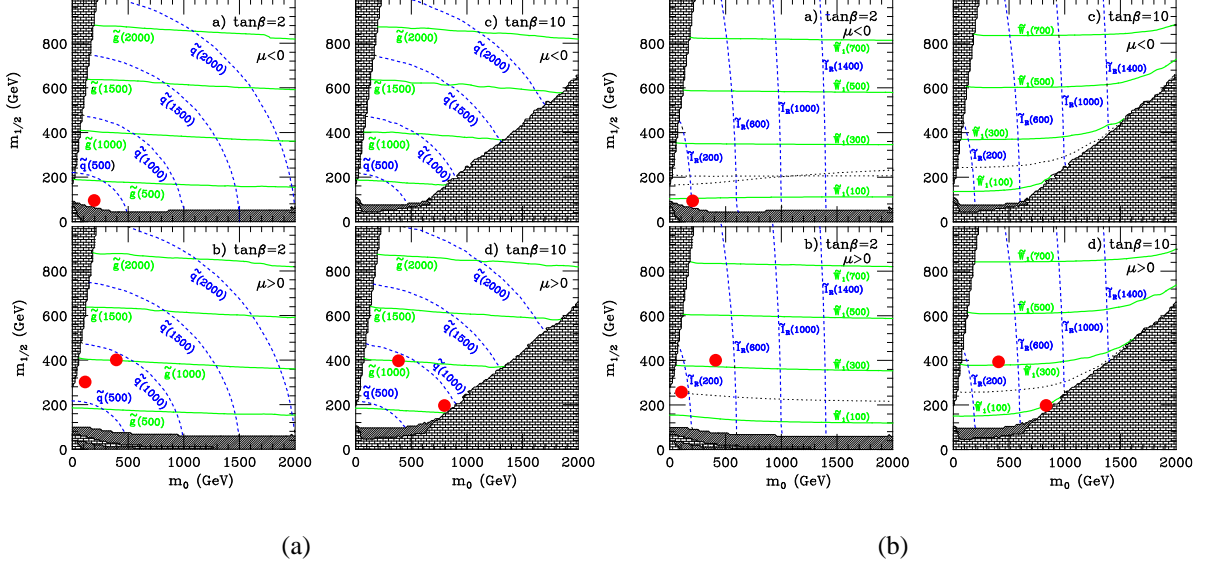
Figure 7.2: *(a) Contours showing gluino and squark masses in the $m_0, m_{1/2}$ plane for $A_0 = 0$ and representative values of $\tan\beta$ in the mSUGRA model. The bricked regions at small m_0 are excluded by the requirement that $\tilde{\chi}_1^0$ be the LSP. The bricked regions at large m_0 and $\tan\beta$ are excluded in ISAJET 7.22 by having no electroweak symmetry breaking. The cross-hatched regions were excluded by experiment at the time of Ref. [BAE95]. The dots represent the five mSUGRA points selected by the LHCC. (b) Contours showing wino and slepton masses in the same parameter plane for again $A_0 = 0$ and representative values of $\tan\beta$ in the mSUGRA model.*

Point	m_0(GeV)	$m_{1/2}$(GeV)	A_0(GeV)	$\tan\beta$	signμ
1	400	400	0	2	+
2	400	400	0	10	+
3	200	100	0	2	-
4	800	200	0	10	+
5	100	300	300	2.1	+
6	200	200	0	45	-

Table 7.3: *The mSUGRA parameter space points studied at LHC and a sixth point with large $\tan\beta$ added later by ATLAS.*

For the mSUGRA parameter choices of points 1 and 2, the SUSY particles are rather heavy, with masses ranging from $m_{\tilde{\chi}_1^0} \sim 170$ GeV for the LSP, to $m_{\tilde{\chi}_1^\pm} \sim 325$ GeV for the lightest chargino, to ~ 500 GeV for left-handed sleptons, and to ~ 1000 GeV for the first two families of squarks and the gluino. These two points were mainly chosen because of the large production of h bosons through cascade decays of $\tilde{q}$ and $\tilde{g}$ involving $\tilde{\chi}_2^0 \rightarrow \tilde{\chi}_1^0$h decays. The resulting h $\rightarrow$ b$\bar{\text{b}}$ decays and the enhanced decay branching ratios of gluinos to heavy-flavour quarks and squarks lead to a large multi-

plicity of b-jets in the final state. This last feature, combined with the more standard features of large transverse missing energy from escaping $\tilde{\chi}_1^0$s, are sufficient, despite the rather small production cross-sections, to reduce the SM background well below the SUSY signal. At these two points, SUSY decay modes involving leptons are rather rare. The hadronic decay modes of the charginos and neutralinos are dominant. In particular the channel $\tilde{\chi}_2^0 \to \tilde{\chi}_1^0 h$ is open whereas the $\tilde{\chi}_2^0 \to \tilde{\chi}_1^0 \tilde{l}$ is closed and the three-body decay $\tilde{\chi}_2^0 \to \tilde{\chi}_1^0 l^+ l^-$ has a negligible branching ratio. Finally, the sleptons are all rather heavy for points 1 and 2, and therefore the only significant source of leptons in the final states of SUSY particle cascade decays is semi-leptonic W decays, where the W bosons are produced dominantly in $\tilde{b}_1 \to \tilde{t}_1 W$ and $\tilde{\chi}_1^\pm \to \tilde{\chi}_1^0 W$ decays.

The main differences between points 1 and 2, in the SUSY sector are for the masses of the squarks of the third family. Another major difference between points 1 and 2, arising from the different values of $tan\beta$ ($tan\beta = 2$ and 10 respectively), is in the Higgs sector. The lightest Higgs mass is ~ 95 GeV at point 1 and ~ 115 GeV at point 2. The other Higgs boson masses are all degenerate and very large (~ 1050 GeV for point 1 and ~ 740 GeV for point 2) and therefore most likely not observable above the background at the LHC.

Point 3 is the 'comparison point', selected so that other existing or proposed accelerators could find something. This point is already ruled out: LEP would have discovered the light Higgs with a mass of 68 GeV. Points 1 and 5 have light Higgs masses which were already excluded by the preliminary limits of the LEP experiments [LEP99]. In all three cases the Higgs mass can be increased by increasing the $tan\beta$ to about three. For point 3 it might also be necessary to increase m_0 and $m_{1/2}$ so that the charginos are in a mass region which could have been explored by LEP. As an example, the mSUGRA point

$$m_0 = 250\,\text{GeV} \quad m_{1/2} = 125\,\text{GeV} \quad A_0 = 0 \quad tan\beta\text{=}5 \quad \mu < 0$$

has a superparticle spectrum generally similar to Point 3 but a light Higgs mass of 98.6 GeV. The gluino mass is 350 GeV and it has a high probability to decay via $\tilde{q} \to \tilde{b}_1 \tilde{b} \to \tilde{\chi}_2^0 b\tilde{b}$; the $\tilde{\chi}_2^0 \to \tilde{\chi}_1^0 l^+ l^-$ branching ratio is smaller but still large enough to be observable. Thus Point 3 remains useful even though it is ruled out by the Higgs search.

The prominent features of this point are: (a) the mass of the gluino and the squarks are relatively small, around 300 GeV, resulting in an extremely large SUSY cross section (1.3 mb) and in the direct production of the SUSY particles being dominated by gluino and squark production; (b) if the produced squark is heavier than the gluino, it decays frequently into gluino, therefore in a large fraction of the events there is a gluino pair, and in the majority of the events there is at least one gluino in the final state; (c) the gluino in its turn decays predominantly into a b-quark and a $\tilde{b}_L$, with

the latter decaying via $\tilde{b}_L \rightarrow \tilde{\chi}^{\pm}_{1,2}q$, $\chi^0_i b$, where $i = 1,2,3,4$; (d) the charginos and neutralinos decay with a sizeable branching fraction into electrons and muons. Therefore an unambiguous signature of SUSY can be obtained in the multi-lepton/multi-b-quark channels.

Point 4 was chosen to be near the boundary for electroweak symmetry breaking, implying that μ is small so that there is quite strong mixing between gauginos and Higgsinos in equations (7.5) and (7.6). This boundary turns out to be quite sensitive to the details of how electroweak symmetry breaking is implemented. At point 4 the gluino is relatively light (small gaugino mass $m_{1/2}$) and the total SUSY cross-section is $\simeq 32$ pb. Furthermore squarks and sleptons are heavy (large scalar mass m_0) at point 4. As a consequence, the second neutralino ($\tilde{\chi}^0_2$) can only decay into $Z^* \tilde{\chi}^0_1$, as discussed in the next section. In particular, the channel $\tilde{\chi}^0_2 \rightarrow \tilde{\chi}^0_1 h$, which is the dominant decay mode of the second neutralino at points 1,2 and 5, and which has been shown to be a very useful handle to select clean SUSY samples, is closed. Point 4 is outside the reach of LEP2 and Tevatron unlike point 3.

Point 5 was motivated by cosmology. As it has already been mentioned, there is strong evidence for non-baryonic cold dark matter in the universe. There is the possibility that a part of this cold dark matter is made up of the 'relic' neutralino density from the very early universe. The requirement of a relic neutralino density consistent with theoretical prejudices and astrophysical observations, puts constraints on the rate of annihilation of the lightest neutralinos. The rate depends on the masses of the virtual sparticles which are exchanged in the annihilation. In particular, the main annihilation channel for neutralinos in most of the parameter space is the one via exchange of sleptons, which are therefore required to be relatively light, in order to provide the required annihilation rate. Indeed, at point 5 the sleptons are relatively light (small value of m_0), whereas the squarks and gluinos are in the middle of the range accessible to LHC experimentation.

7.5   Neutralino Decay Studies in mSUGRA

The Monte Carlo generators used for the study presented here was PYTHIA 6.158 and PYTHIA 6.160. The supersymmetric extension of PYTHIA, which is called SPYTHIA [SPY96] and can simulate particle production and decay in mSUGRA (approximately), is implemented already in the above mentioned versions of PYTHIA.

The weak point of the version 6.158 (and of course of all the older ones), arises from the pure phase-space treatment of SUSY particle decays and from not accounting for spin correlations, neither at production not for decays. It is assumed that the matrix element for these decays is relatively flat in phase space, and could thus be treated as a constant. In July 2001, the version 6.160 was released. The spin-averaged matrix element is now included in the SUSY particles decays, thus taking into account the spin of the neutralinos, as well as the propagator (Z*) in three-body decays. A number of approximations were although made. The decay chain is really treated in independent steps, instead of including the possibility of correlations. For example, in the decay of the gluino ($\tilde{g} \to q\bar{q}\tilde{\chi}_2^0$), gluino spins are averaged over; so, if there was any polarization in the production process, it is ignored. Next, the $\tilde{\chi}_2^0$ spins are summed over, so again, any polarization of the $\tilde{\chi}_2^0$ is lost in this summation. Finally, when the $\tilde{\chi}_2^0$ is decayed ($\tilde{\chi}_2^0 \to \tilde{\chi}_1^0 l^+ l^-$), the $\tilde{\chi}_2^0$ spins are averaged over, and the $\tilde{\chi}_1^0$ spins are summed [MRE01].

In the present thesis, the first studies for the second neutralino decay at point 4 of mSUGRA using the improved code of PYTHIA (PYTHIA 6.160) are presented. A comparison between the results of the two versions of PYTHIA is made offering the possibility of distinguishing between a spin-averaged matrix neutralino decay and a pure phase space one.

7.5.1   Main Characteristics of the fourth point

The point 4 is characterised by the following values of the parameters in the 5-dimensional mSUGRA space:

$m_0 = 800$ GeV
$m_{1/2} = 200$ GeV
$A_0 = 0$
$tan\beta = 10$
$sign(\mu) = +$

The particle mass spectrum for this specific point is given in Table 7.4. Among the SUSY processes, which have large cross-sections at Point 4 at the LHC, gluino pair production dominates (since the gluino is light) followed by $\tilde{q}\tilde{g}$ production. Since the squarks are heavy in this point, $\tilde{q}\tilde{q}$ production has a much smaller cross-section (Table 7.5). Figure 7.3 shows processes of gluon fusion, quark-antiquark and quark-gluon

scattering that produce $\tilde{g}\tilde{g}$ and $\tilde{q}\tilde{g}$.

At point 4 the gluino mass is smaller than the squark mass, therefore the gluino can not decay to $\tilde{q}q$ pairs as it does at the other four mSUGRA points. Instead, it undergoes three-body decays into a $q\bar{q}$ pair plus a gaugino (see Table 7.6).

Particle	Mass (GeV)	Particle	Mass (GeV)
$\tilde{g}$	563	$\tilde{\chi}_1^0$	80
$\tilde{q}$	896	$\tilde{\chi}_2^0$	152
$\tilde{t}_1$	542	$\tilde{\chi}_3^0$	384
$\tilde{t}_2$	767	$\tilde{\chi}_4^0$	397
$\tilde{b}_1$	740	$\tilde{\chi}_1^\pm$	151
$\tilde{b}_2$	882	$\tilde{\chi}_2^\pm$	399
$\tilde{l}$	809	h	111

Table 7.4: *Sparticles masses at Point 4 of mSUGRA, as given by PYTHIA 6.160. For the masses of the squarks of the first two generations and of the sleptons, an average between the left-handed and the right handed helicity states has been taken.*

Process	$\sigma(pb)\ PYTHIA\ 6.160$
$\tilde{g}\tilde{g}$	14.80
$\tilde{q}\tilde{g}$	10.00
$\tilde{q}\tilde{q}$	1.00
$\tilde{\chi}^\pm\tilde{\chi}^0$	3.40
$\tilde{\chi}_1^\pm\tilde{\chi}_1^\mp,\tilde{\chi}_2^\pm\tilde{\chi}_2^\mp,\tilde{\chi}_1^\pm\tilde{\chi}_2^\mp$	1.70
$t\bar{t}$	0.44
$\tilde{\chi}^0\tilde{\chi}^0$	0.03
Other	0.88
Total	32.25

Table 7.5: *Production cross-sections for some main SUSY processes at Point 4, as given by PYTHIA 6.160.*

Gluino	Decay channel	BR (%)
$\tilde{g} \rightarrow$	$q\,\bar{q}'\,\tilde{\chi}_1^\pm$	51.18
	$q\,\bar{q}\,\tilde{\chi}_2^0$	31.23
	$q\,\bar{q}\,\tilde{\chi}_1^0$	17.32
	$q\,\bar{q}'\,\tilde{\chi}_2^\pm$	0.12
	$q\,\bar{q}\,\tilde{\chi}_4^0$	0.12
	$q\,\bar{q}\,\tilde{\chi}_3^0$	0.01

Table 7.6: *Gluino decay modes and branching ratios (BR), as given by PYTHIA 6.160.*
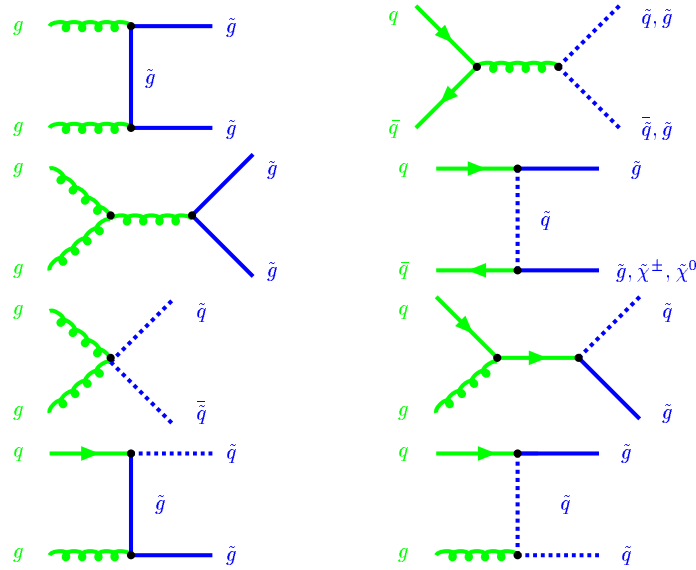
Figure 7.3: *Processes responsible for gluino pair production as well as for squark-gluino production at LHC.*

At point 4 leptons are mainly produced in the chargino and neutralino decays shown in Table 7.7. The light charginos and neutralinos have no two-body decays at this mSUGRA point. The second neutralino decays into the first neutralino and two leptons in a three-body decay that occurs through a virtual Z*. The branching ratio of this decay, considering only electrons and muons, is about 5%. The study of this decay channel is the subject of the following sections.

Decay	Branching ratio per lepton family (%)
$\tilde{\chi}_2^0 \to \tilde{\chi}_1^0 l^+ l^-$	2.58
$\tilde{\chi}_1^\pm \to l \nu \tilde{\chi}_1^0$	10.9
$\tilde{\chi}_2^\pm \to \tilde{\chi}_1^\pm Z$ with $Z \to l^+ l^-$	1.0

Table 7.7: *Decays of gauginos that produce leptons at point 4 (l= e, μ, τ).*

7.5.2   Dilepton invariant mass distribution

The three-body decay of the next-to lightest neutralino ($\tilde{\chi}_2^0$) gives an interesting signature for point 4, which should allow not only the observation of a SUSY signal, but also the measurement of some parameters of the theory such as the mass difference between the second lightest and the lightest neutralino. The relevant Feynman diagram is shown in Figure 7.4.
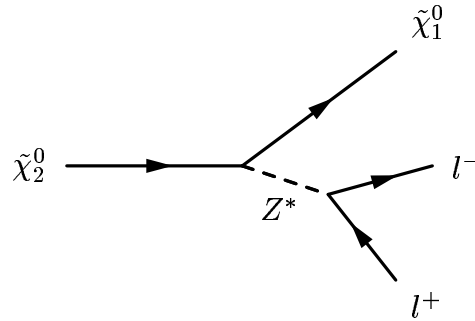
Figure 7.4: *The second neutralino decay through a virtual Z* at point 4 ($l^+, l^- = lep$-tons).*

For our studies, SUSY signal events for point 4 were generated using PYTHIA 6.158 and PYTHIA 6.160. All SUSY processes were switched on at the same time (MSEL=39 in SPYTHIA). The total number of events produced for each version of PYTHIA was $3 \cdot 10^5$. Subsequently, these produced events were passed through the standard fast detector simulation and physics analysis program ATLFAST [ATL98]. ATLFAST is much faster than the existing full simulation programs of ATLAS as it is based on a parametrized detector response to the physics reactions. It includes the most crucial detector effects such as jet reconstruction in the calorimeters of the detector, momentum and energy smearing of leptons and photons, magnetic field effects, missing transverse energy and trigger simulation. Its reliability has been extensively tested for many processes by comparing it with the full simulation results.

The main potential Standard Model backgrounds are $t\bar{t}$ production, W and Z pair production (WW, ZZ), Z +jets, W + jets and finally WZ. We produced $2 \cdot 10^6$ $t\bar{t}$ events ($\sigma = 399$ pb) and $8 \cdot 10^5$ events of the remaining processes ($\sigma = 2300$ pb). These events were also processed through ATLFAST. A cut of $p_T > 100$ GeV of the hard-scattering process was applied at the generation level.

Features discriminating SUSY events from SM processes are the large transverse missing energy, due to the presence of two $\tilde{\chi}_1^0$s in the final state, and large multiplicity of high-p_T jets and/or leptons, since the produced sparticles are usually heavy and decay through cascade decays. Therefore, in order to select a clean SUSY sample and eliminate as much as possible the SM background, the following selection criteria are applied:

- Two opposite-sign same-flavour (OS-SF) isolated[2] leptons (electrons or muons) are required.

---

[2]A lepton is labelled as 'isolated' if the transverse energy contained in a cone of size $\Delta R = \sqrt{\Delta^2 \eta + \Delta^2 \phi} = 0.2$ around the lepton direction is smaller than 10 GeV and the lepton is seperated from calorimeter clusters by $\Delta R > 0.4$ (the η and ϕ are explained later in the text).

- The most energetic lepton of the two should have a transverse momentum $p_{T,1} > 20$ GeV while the less energetic should have $p_{T,2} > 10$ GeV. Both should have pseudorapidity $|\eta| < 2.5$.

- The missing transverse energy E_T^{miss} in our events should be $E_T^{miss} > 200$ GeV to account for the lightest neutralinos $\tilde{\chi}_1^0$ escaping the detector.

- At least four jets with transverse momenta $p_T > 100$, 55, 55 and 55 GeV respectively and pseudorapidity $|\eta| < 3.2$ are required to account for gluino pair production as primary production mechanism.

The beam direction defines the z-axis and the x-y plane is the plane transverse to the beam direction. The positive x-axis is defined as pointing from the interaction point to the centre of the LHC ring and the positive y-axis is pointing upwards. The azimuthal angle ϕ is measured around the beam axis and the polar angle θ is the angle from the beam axis. The pseudorapidity is defined as:

$$\eta = -ln\,tan(\theta/2) \tag{7.10}$$

The transverse momentum p_T and the transverse energy E_T, as well as the missing transverse energy E_T^{miss} and other transverse variables, are defined in the x-y plane. The presence of the E_T^{miss} is revealed by summing the transverse momenta of all the observed particles. If the sum is not zero, as required by momentum conservation, the missing transverse energy can only be due to particles that escaped detection (neutrinos, neutralinos etc). The reason that we are using these transverse quantities is that at the LHC we have no longitudinal momentum balance as the collision is going to take place between the constituents of the protons, which carry only a fraction of the total energy of the proton.

After selecting the opposite-sign same-flavour leptons, which satisfy the above selection cuts, we reconstructed their invariant mass. This dilepton mass distribution was then normalised for an integrated luminosity of $3 \cdot 10^4$ pb^{-1} (three years of LHC running at low luminosity). The dominant remaining SM background is from $t\bar{t}$ production and it was also normalised for the same integrated luminosity as the SUSY reconstructed events. The other SM backgrounds (WW, WZ, ZZ, Z+jets and W+jets) are completely suppressed by the jet multiplicity cut and the E_T^{miss} cut. Figure 7.5 shows the dilepton mass distribution for both versions of PYTHIA used. In both cases around 6500 SUSY events (OS-SF) remain while the SM $t\bar{t}$ background is reduced to only 250 events. The main background left comes from other SUSY processes e.g. chargino decays (SUSY background).

An excess of dileptons with the specific shape of the dilepton mass spectrum shown in this Figure, can be used as evidence for discovery of SUSY through $\tilde{\chi}_2^0$ production. The endpoint of the distribution measures the mass difference between the second

lightest and the lightest neutralino $M_{l^+l^-}^{max} = M_{\tilde{\chi}_2^0} - M_{\tilde{\chi}_1^0} \simeq 72$ GeV (same for both versions). It is obvious that the inclusion of the spin-averaged matrix element in the second neutralino decay modifies the shape of the dilepton mass spectrum (Figure 7.5b), which peaks close to the endpoint, indicating more apparently that the decay takes place through a virtual Z and not an slepton (which is heavy at this mSUGRA point anyway).
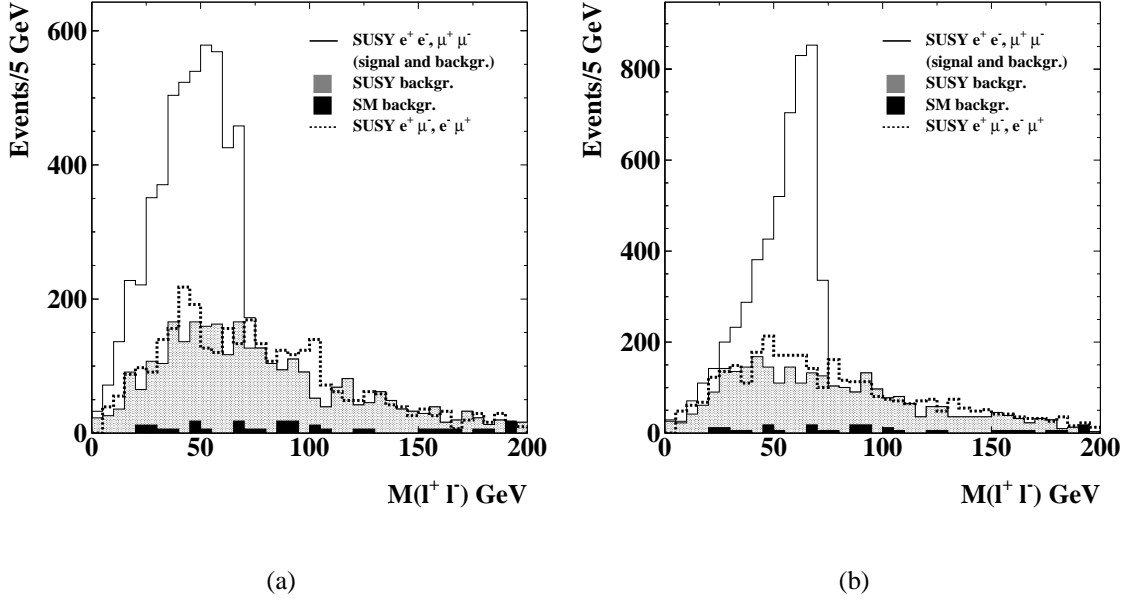

(a)   (b)

Figure 7.5: *Expected dilepton invariant mass distributions for SUSY events containing opposite-sign same-flavour lepton pairs at Point 4 (full histogram) and for the $t\bar{t}$ background (dashed black histogram), for an integrated luminosity of $3 \cdot 10^4$ pb^{-1} for (a) PYTHIA 6.158 (phase space neutralino decay), and (b) PYTHIA 6.160 (spin-averaged matrix element included in the sparticles decays). In both Figures the SUSY background consisting of opposite-sign same-flavour lepton pairs is also indicated (dashed grey histogram). The dashed histogram represents the combinatorial background consisting of opposite-sign opposite-flavour lepton pairs.*

It should be pointed out that the dilepton mass distribution of PYHTIA 6.158 (Figure 7.5a), differs a bit from the one presented at the [ATL99] and [FAB97]. The main difference is the absence of a peak at around 90 GeV in our results. This structure concentrated around the Z mass, while using older versions of PYTHIA, indicated the production of Z bosons in SUSY cascade decays. This Z peak was mainly due to the production of the second chargino $\tilde{\chi}_2^\pm$ in the gluino decay ($\tilde{g} \rightarrow q\bar{q}'\tilde{\chi}_2^\pm$) with a branching ratio of 6%, followed by the decay $\tilde{\chi}_2^\pm \rightarrow Z\tilde{\chi}_1^\pm$. In the versions of PYTHIA that we used in the present study, the branching ratio for this gluino decay is only 0.12%, thus

the Z peak almost vanishes.

The combinatorial background contribution from other SUSY processes can be estimated by using a sample of events selected with the same cuts as already described earlier in this section, except that the two leptons are required to have opposite sign and opposite flavour (OS-OF), i.e. $e^+\mu^-$ or $e^-\mu^+$. About 3300 such events are expected from SUSY production at Point 4 for an integrated luminosity of $3 \cdot 10^4$ pb^{-1}. Figure 7.5 shows the dilepton invariant mass distribution for the OS-OF SUSY sample (both PYTHIA versions), superimposed to the OS-SF SUSY and background distributions. The distribution of this combinatorial background is very similar to the SUSY background given by the simulation and is therefore a powerful tool to estimate the SUSY background in real conditions at LHC.

A more quantitative comparison between the invariant mass spectra of the two PYTHIA versions is made by fitting the two distributions with the same function and compare its parameters. After several attempts, we obtained the following fitting function:

$$F(x) = p_1 \cdot e^{\frac{(x-p_2)}{p_3} - e^{\frac{x-p_2}{p_3}}} + P \tag{7.11}$$

where p_i ($i = 1,2,3$) are the parameters determined by the fit, while P is a fixed polynomial of 6th degree that fits the combinatorial distribution and is treated as a constant in the fit using the function F(x). The parameter p_1 serves as a normalisation parameter for the size of the distribution, the p_2 is the peak position and finally p_3 characterizes the width of the distribution. The result obtained after we performed the fit on the dilepton mass distributions shown in Figure 7.5, is presented in Figure 7.6.
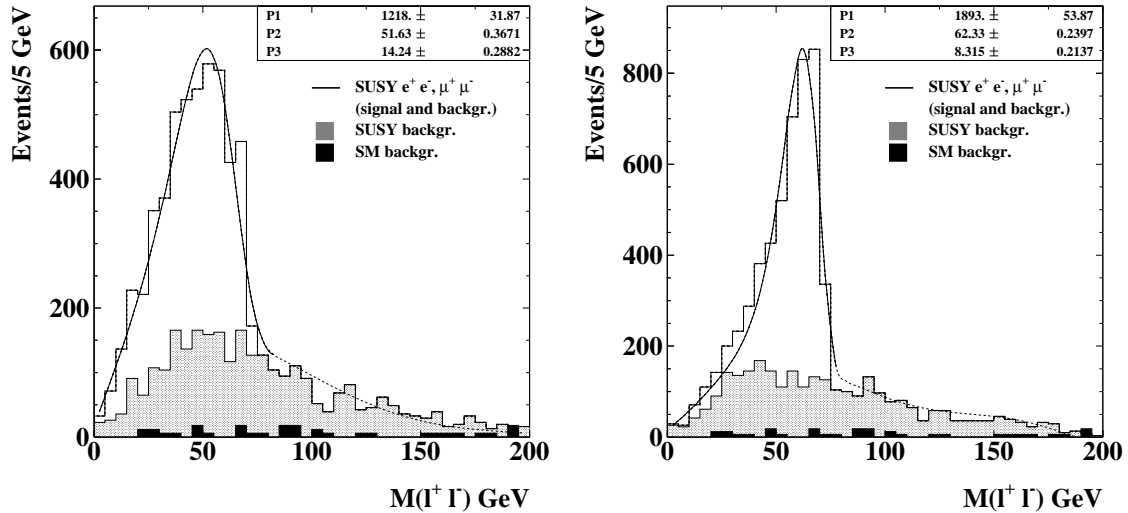

Figure 7.6: *The dilepton invariant mass distributions of Figure 7.5 fitted with the function (7.11) for (a) PYTHIA 6.158 and (b) PYTHIA 6.160. The fitted function is plotted as a solid line in the mass region used in the fit.*

It is obvious, as indicated also by the values of the parameter p_3, that the mass distribution where only the phase space neutralino decay is taken into account, has a larger width than the distribution where the spin-averaged matrix element is included in the sparticles decays ($p_3 \approx 14$ and ≈ 8 GeV for PYTHIA versions 6.158 and 6.160 respectively). The peak of the distribution for PYTHIA 6.160 is shifted more to higher energies and is expressed by the value of the parameter $p_2 \approx 62$ GeV, while for PYTHIA 6.158 is $p_2 \approx 52$. Therefore at Point 4 the effects of the matrix element inclusion are profound.

7.5.3 Modifying the parameters of mSUGRA

The next step was to identify the regions in the parameter space of mSUGRA where the potential of the specific channel of the second neutralino decay can be explored. These studies are presented in this section.

Changing the m_0 and $m_{1/2}$

Our purpose is to study the change of the shape of the dilepton mass distribution (and not of the endpoint position as already studied in [FAB97]) of the decay $\tilde{\chi}_2^0 \to \tilde{\chi}_1^0 l^+ l^-$ in different points of the mSUGRA parameter space, starting from the point 4. Therefore, we scanned the $m_0, m_{1/2}$ space only, while keeping the values of the $tan\beta$, the $sign(\mu)$ and the A_0 the same as in Point 4. We selected those points of the parameter space where the mass difference between the next-to lightest and the lightest neutralino is that of Point 4 ($M_{\tilde{\chi}_2^0} - M_{\tilde{\chi}_1^0} \approx 72$ GeV). In points where this requirement is not fulfilled, the position of the endpoint of the invariant mass distribution of the OS-SF lepton pairs would change. Some of the points where $M_{\tilde{\chi}_2^0} - M_{\tilde{\chi}_1^0} \approx 72$ GeV, are shown in Figure 7.7. The parameter $m_{1/2}$ is almost completely responsible for determining the gluino mass, as well as the masses of the two lightest neutralinos (see equation 7.7). Therefore the mass difference between $\tilde{\chi}_2^0$ and $\tilde{\chi}_1^0$ is not very sensitive to the change of the parameter m_0.
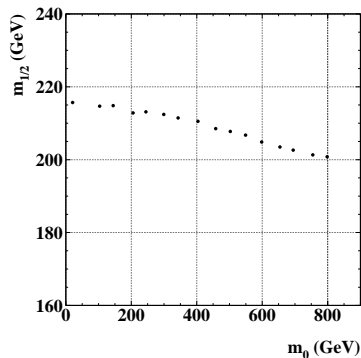

Figure 7.7: *Points in a region of the $m_0, m_{1/2}$ parameter space where $M_{\tilde{\chi}_2^0} - M_{\tilde{\chi}_1^0} \approx 72$ GeV.*

It is important to mention that the scan of the parameter space was made for values of $m_0 < 800\,\text{GeV}$ and $m_{1/2} > 200\,\text{GeV}$. As it was demonstrated in Figure 7.2a, for the region around Point 4, values of $m_0 > 800\,\text{GeV}$ and $m_{1/2} < 200$ are excluded. From the points presented in the above Figure, we selected the ones listed in Table 7.8. We named them as A, B, C and D for quick reference.

Point	m_0	$m_{1/2}$
A	600	205.5
B	400	210.5
C	200	213.5
D	25	215.5

Table 7.8: *The four points of the mSUGRA parameter space selected for our studies.*

For each of these scan points we reconstructed for both versions of PYTHIA (6.158 and 6.160), the invariant mass distribution of opposite-sign same-flavour lepton pairs and applied the same selection cuts as described in section 7.5.2. The dilepton mass spectra obtained for points A, B and C are presented in Figures 7.8, 7.9 and 7.10 respectively. The combinatorial background coming from other SUSY processes is also plotted. For point D, the branching ration for the decay $\tilde{\chi}_2^0 \to \tilde{\chi}_1^0 l^+ l^-$ is negligible, so this channel is almost closed and practically no signal events were observed.

(a)   (b)
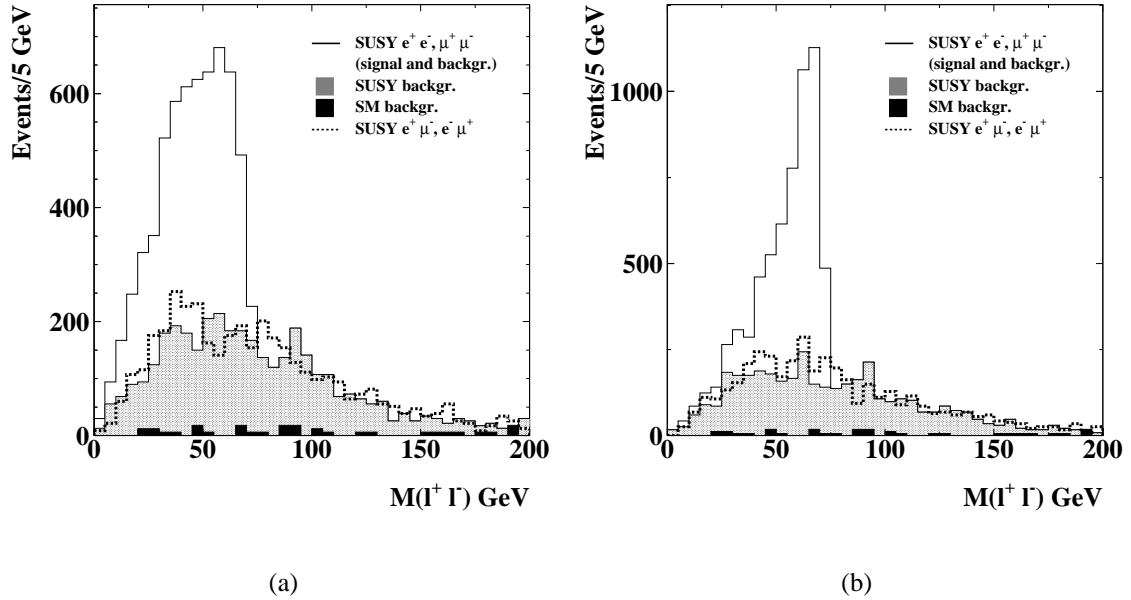
Figure 7.8: *Point A: Dilepton invariant mass distributions for SUSY events containing OS-SF lepton pairs (full histogram), OS-OF lepton pairs (dashed histogram), and for $t\bar{t}$ events containing OS-SF pairs (dashed black histogram) for an integrated luminosity of $3 \cdot 10^4\,pb^{-1}$, for (a) PYTHIA 6.158 and (b) PYTHIA 6.160.*

(a)

(b)
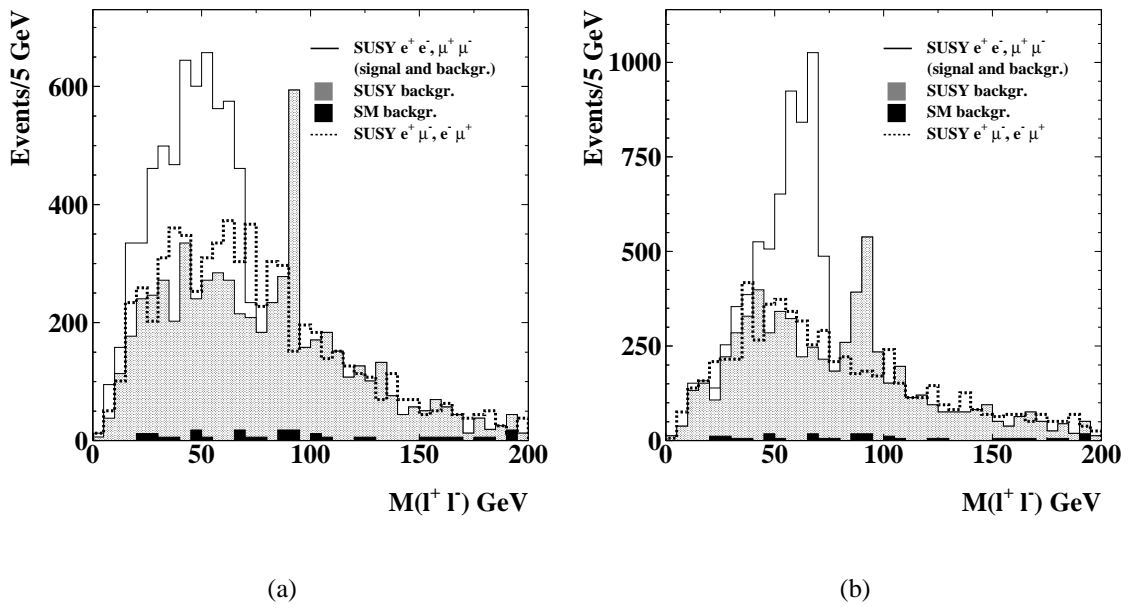
Figure 7.9: *Same as in Figure 7.8 but for point B.*

(a)

(b)
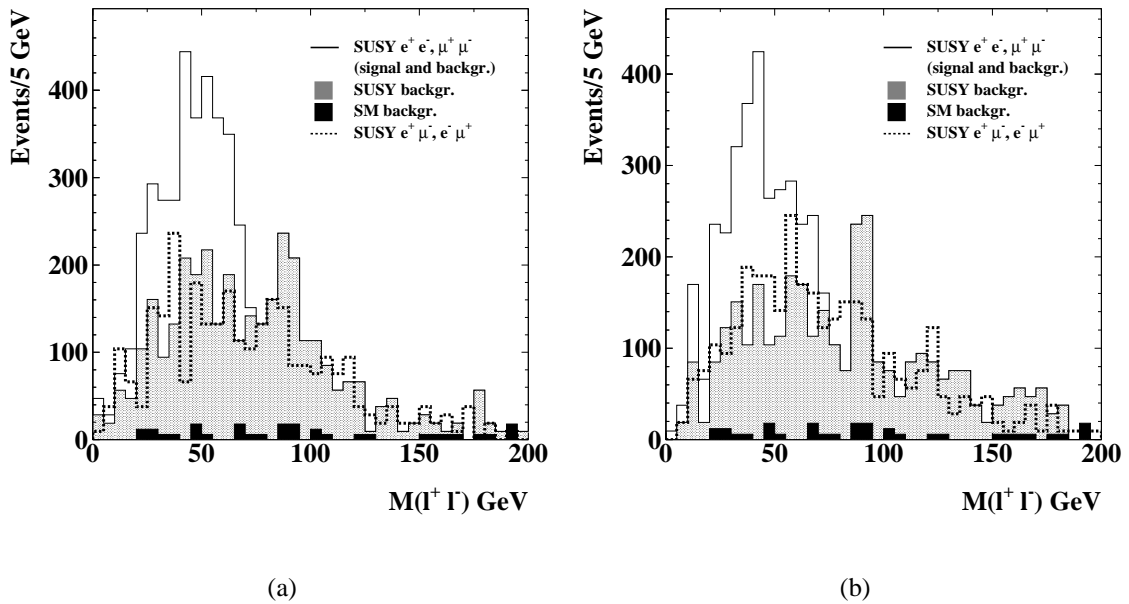
Figure 7.10: *Same as in Figure 7.8 but for point C.*

In order to quantitatively distinguish between the two PYTHIA versions for each scan point, we fitted the mass distributions with the function (7.11). The fitted curve is shown in the Figures 7.11, 7.12 and 7.13 for the points A, B and C respectively. The values of the parameters p_2 and p_3 that were obtained from the fit, as well as the number of OS-SF SUSY events in each distribution, are summarized in Table 7.9.

(a)   (b)

Figure 7.11: *Point A: The dilepton invariant mass distributions of Figure 7.8 fitted with the function (7.11) for (a) PYTHIA 6.158 and (b) PYTHIA 6.160.*

(a)   (b)

Figure 7.12: *Point B: The dilepton invariant mass distributions of Figure 7.9 fitted with the function (7.11) for (a) PYTHIA 6.158 and (b) PYTHIA 6.160.*
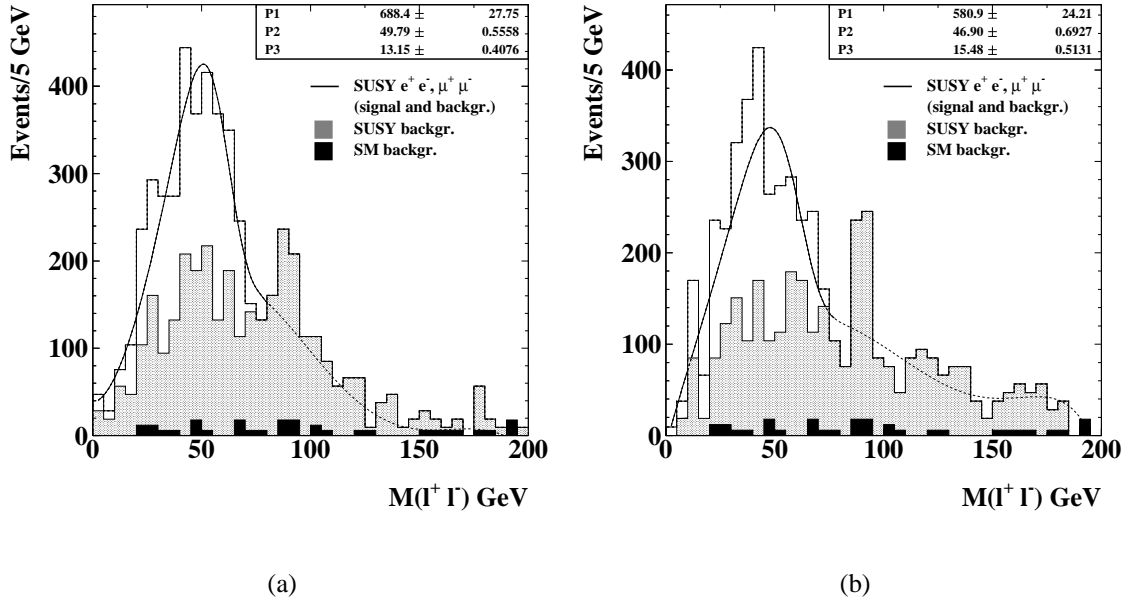
Figure 7.13: *Point C: The dilepton invariant mass distributions of Figure 7.10 fitted with the function (7.11) for (a) PYTHIA 6.158 and (b) PYTHIA 6.160.*

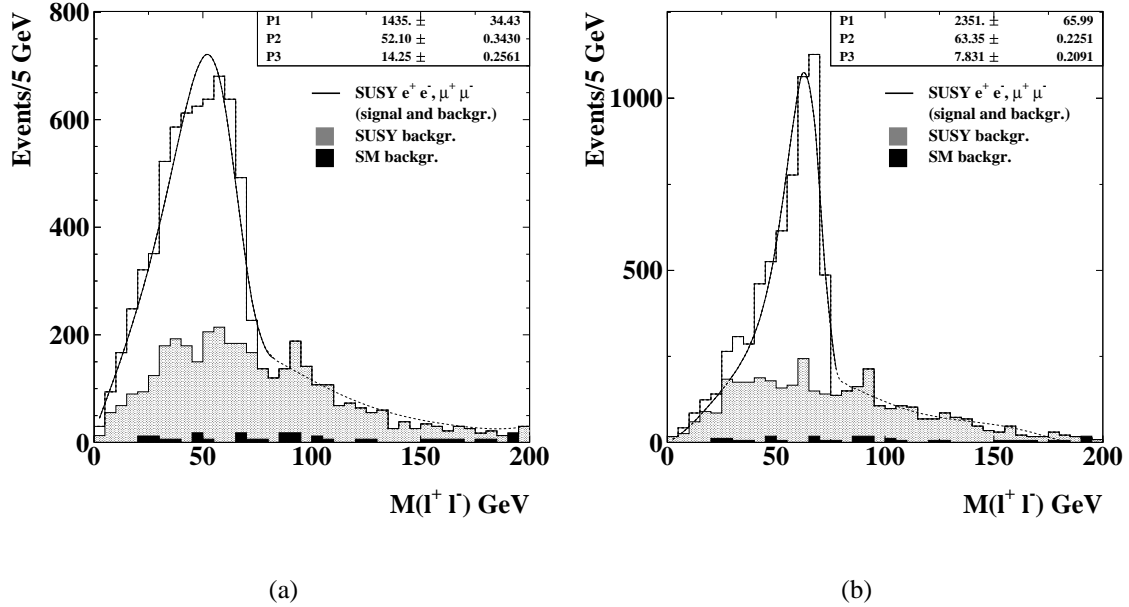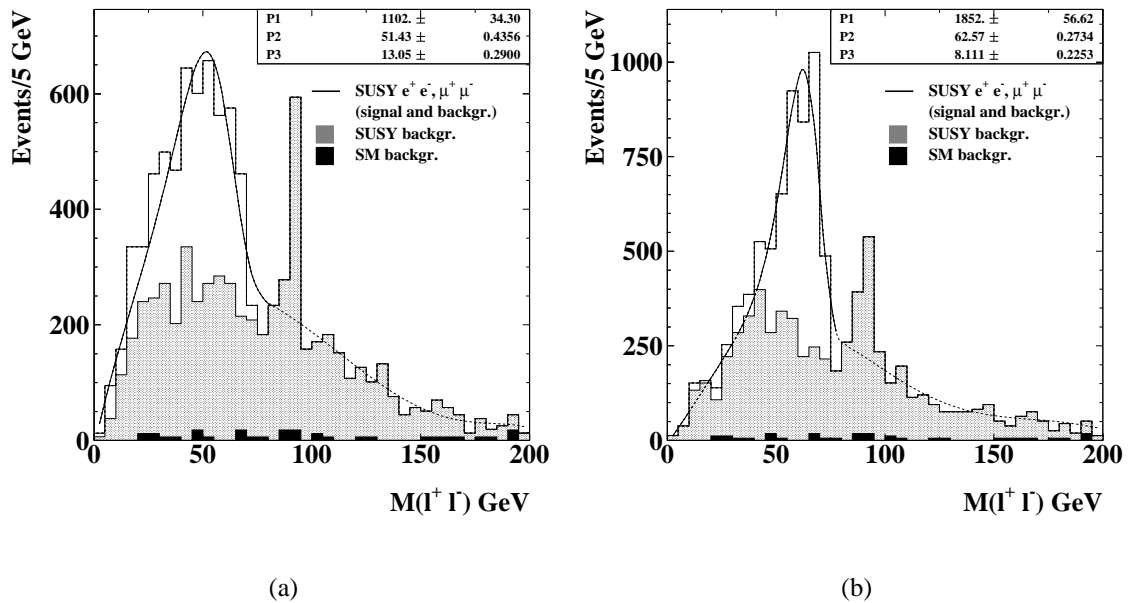|	PYTHIA 6.158			PYTHIA 6.160		
Point	No of events	$p_2(GeV)$	$p_3(GeV)$	No of events	$p_2(GeV)$	$p_3(GeV)$
4	6500	52	14	6500	62	8
A	7800	52	14	8000	63	8
B	9000	51	13	9500	63	8
C	5200	50	13	5000	47	15

Table 7.9: *Number of OS-SF SUSY events and the values of parameters p_2 and p_3, for Point 4, as well as for the points A, B and C (for both versions of PYTHIA).*

It is obvious that for points A and B, the two versions of PYTHIA can be distinguished. The effect of the spin-averaged matrix element is profound, as the mass distribution obtained using the newer version, is still steeper close to the endpoint position and its width is smaller than the one resulting from the use of the older version. The shape of the invariant mass distribution for signal events, is not very sensitive to the change of the parameter m_0; for the wide range of $m_0 = 800$ GeV till $m_0 \sim 400$ GeV the shape is very similar. At point C, the distributions for both versions of PYTHIA become quite similar. The number of OS-SF events for both versions stays quite the same.

A noticeable difference between the invariant mass spectra for different values of m_0, is the appearance of a peak around 90 GeV (see points B and C).

At point B, the Z peak is mainly due to the production of the second chargino $\tilde{\chi}_2^-$ in the decay $\tilde{b}_1 \to \tilde{\chi}_2^- t$ with a branching ratio of 17%. At this mSUGRA point the squarks have smaller masses (~ 600 GeV) than those at Point 4 so the $\tilde{q}\tilde{g}$ production dominates. The SUSY cross-section is larger (63.34 pb). Moreover, the gluino decays mainly as $\tilde{g} \to \tilde{b}_1 \bar{b}$, $\tilde{b}_1 b$ (78% branching ratio). Such a decay mode of the gluino at Point 4 is impossible due to the fact that $\tilde{b}_1$ is heavier there.

At point C, the $\tilde{q}\tilde{g}$ production again dominates. The gluino does not have three body decays at this point; instead, it decays mainly to $\tilde{q}\bar{q}$. Subsequently the squarks decay producing neutralinos and charginos. The Z peak at this point comes from the decays of these charginos. The SUSY cross section is even larger here (94.3 pb). Although at points B and C the Z peak is quite high, it still does not obscure the mass distributions for < 72 GeV that we are interested in.

As we move from point 4 towards point C, the masses of the sleptons (squarks) decrease from ~ 800 GeV (~ 900 GeV) down to ~ 250 GeV (~ 500 GeV).

Changing the $tan\beta$ and $sign(\mu)$

A supplementary step in our studies was to explore the potential use of the channel $\tilde{\chi}_2^0 \to \tilde{\chi}_1^0 l^+ l^-$ in more regions of the mSUGRA parameter space where except from the m_0 and $m_{1/2}$ parameters, the value of $tan\beta$ and the $sign(\mu)$ were changed. Therefore we considered three more cases where first the $sign(\mu)$ was taken negative (while the remaining mSUGRA parameters were the same as the ones at point 4), secondly the value of the $tan\beta$ assumed to be equal to 2 ($\mu > 0$) and finally $tan\beta = 2$ with $\mu < 0$. For these three cases, as well as for the case where $tan\beta = 10$ and $sign(\mu) > 0$ (as they are point 4), we first calculated the branching ratio of our decay channel while scanning the parameter space of $(m_0, m_{1/2})$ (Figure 7.14).

In the following part of this section, studies in a few selected points with different values of mSUGRA parameters are presented.
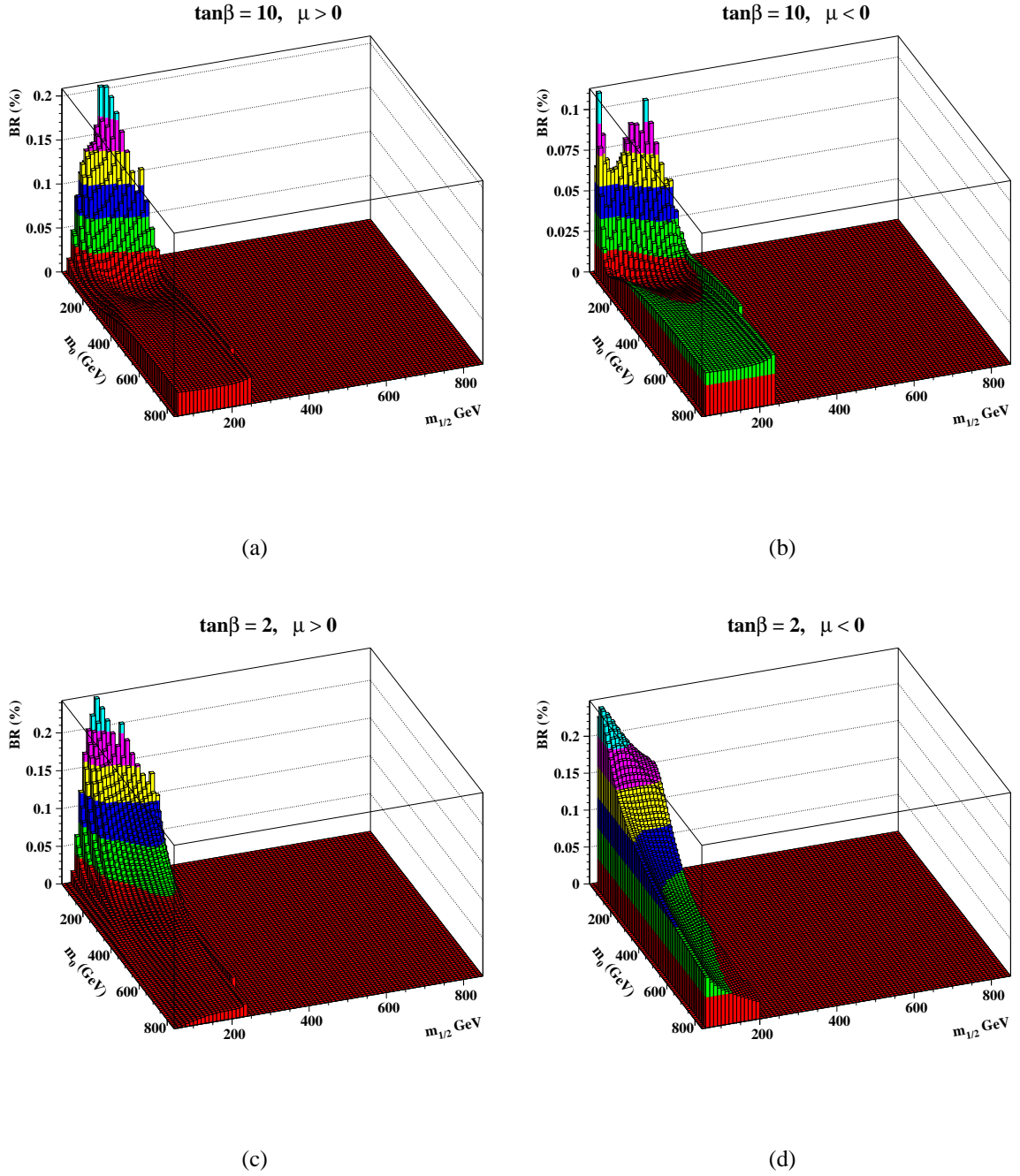
Figure 7.14: *Branching ratios of the decay $\tilde{\chi}_2^0 \rightarrow \chi_1^0 l^+ l^-$ in different regions of the mSUBRA parameter space, (a) $tan\beta = 10$ and $sign(\mu) > 0$, (b) $tan\beta = 10$ and $sign(\mu) < 0$, (c) $tan\beta = 2$ and $sign(\mu) > 0$, (d) $tan\beta = 2$ and $sign(\mu) < 0$.*

The dilepton mass distribution of opposite-sign same-flavour lepton pairs for the point

$$m_0 = 800\,\text{GeV} \quad m_{1/2} = 200\,\text{GeV} \quad A_0 = 0 \quad tan\beta = 10 \quad \mu < 0$$

called for simplicity in this analysis, point 'minus', is shown in Figure 7.15. The same distribution but fitted with the function (7.11) is presented in Figure 7.16. It should be pointed out that this point differs from this of point 4 only by the $sign(\mu)$.

The number of OS-SF SUSY events expected are about 6700 for both versions of PYTHIA and for an integrated luminosity of $3 \cdot 10^4$ pb^{-1}. The already well known effect of the spin-averaged matrix element is again visible in these Figures. The mass distribution in Figure 7.15b is very similar to the one of point 4, as even the position of the endpoint does not change. At point 'minus', the mass difference between the next-to lightest and the lightest neutralino is still ≈ 72 GeV. The SUSY cross section for this point is quite the same with the one at point 4 (~ 32 pb).

(a)   (b)

Figure 7.15: *Point 'minus': Dilepton invariant mass distributions for SUSY events containing OS-SF lepton pairs (full histogram), OS-OF lepton pairs (dashed histogram), and for t$\bar{t}$ events containing OS-SF pairs (dashed black histogram), for an integrated luminosity of $3 \cdot 10^4$ pb^{-1}, for (a) PYTHIA 6.158 and (b) PYTHIA 6.160. In both Figures again, the SUSY background consisting of opposite-sign same-flavour lepton pairs is indicated (dashed grey histogram)*

P1	1191. ±		29.10
P2	52.78 ±		0.3970
P3	15.68 ±		0.2868

(a)

P1	1913. ±		54.06
P2	66.58 ±		0.2511
P3	9.370 ±		0.2478

(b)

Figure 7.16: *Point 'minus':The dilepton invariant mass distributions of Figure 7.15 fitted with the function (7.11) for (a) PYTHIA 6.158 and (b) PYTHIA 6.160.*

Another point similar to that of point 4 but differing only in the $tan\beta$ value is the following:

$$m_0 = 800 \, \text{GeV} \quad m_{1/2} = 200 \, \text{GeV} \quad A_0 = 0 \quad tan\beta = 2 \quad \mu > 0$$

At this point though the branching ratio for the decay $\tilde{\chi}_2^0 \rightarrow \tilde{\chi}_1^0 l^+ l^-$ is negligible (as can be seen also in Figure 7.14c). Therefore no dilepton mass distribution of OS-SF lepton pairs containing a sufficient number of pure signal events could be reconstructed.

Trying to explore more the parameter space with this topology, we changed also the value of the m_0 parameter. Therefore the modified point where we could finally reconstruct the invariant mass spectrum of the relevant lepton pairs is:

$$m_0 = 300 \, \text{GeV} \quad m_{1/2} = 200 \, \text{GeV} \quad A_0 = 0 \quad tan\beta = 2 \quad \mu > 0$$

The results are shown in Figures 7.17 and 7.18 and they are quite similar for both versions of PYTHIA. The number of expected OS-SF SUSY events is ~ 15000 (integrated luminosity of $3 \cdot 10^4$ pb^{-1}). The SUSY cross section is about three times larger than the one at point 4 (~ 104 pb), $\tilde{q}\tilde{g}$ production dominates, while the mass of the sleptons is about 300 GeV.

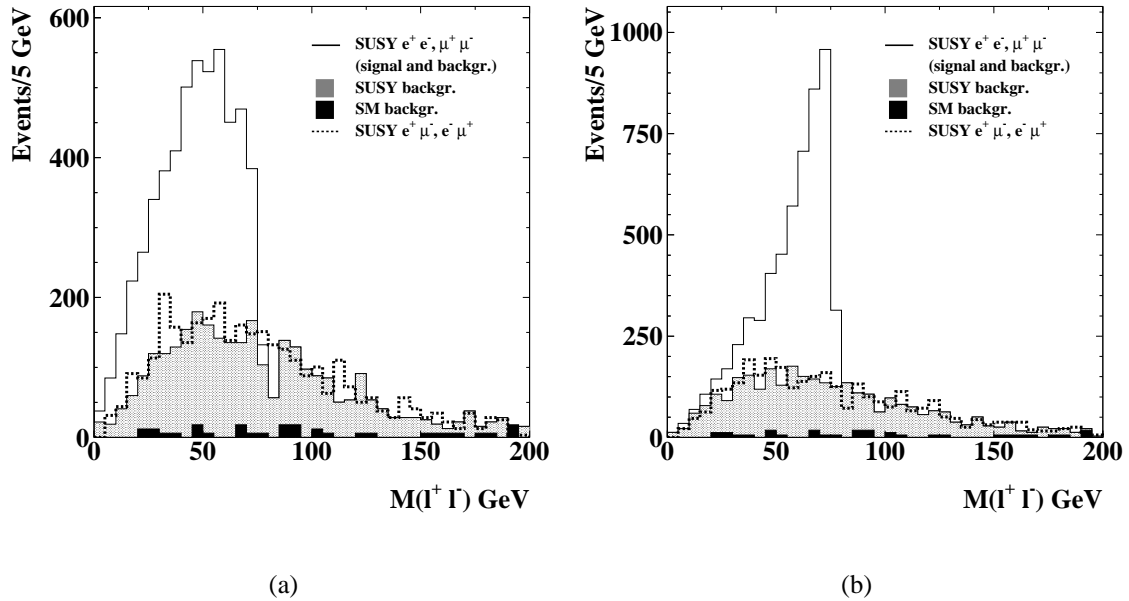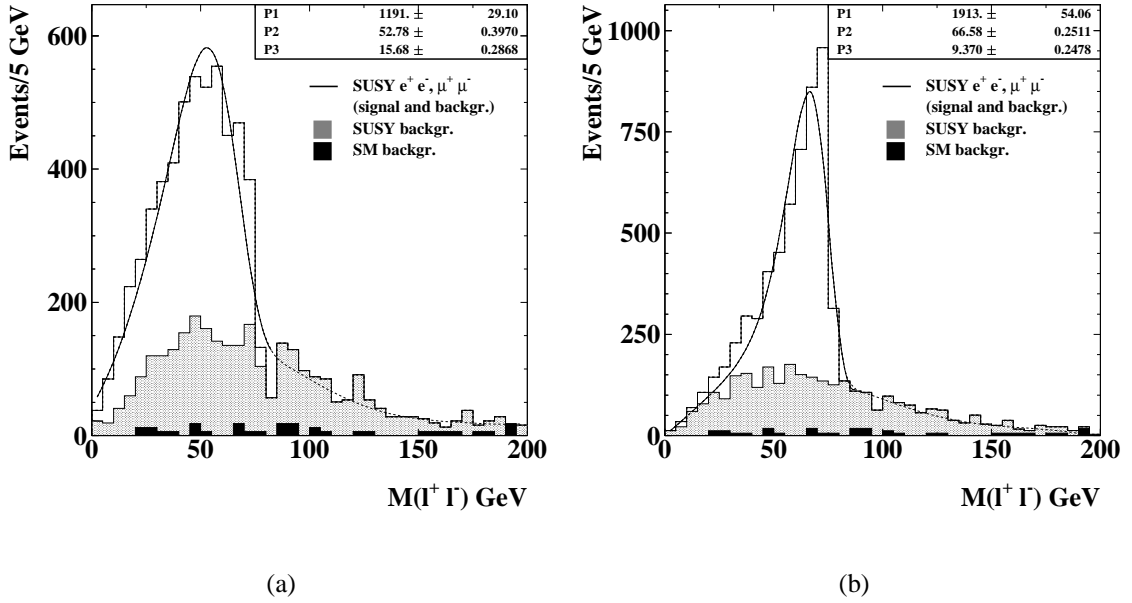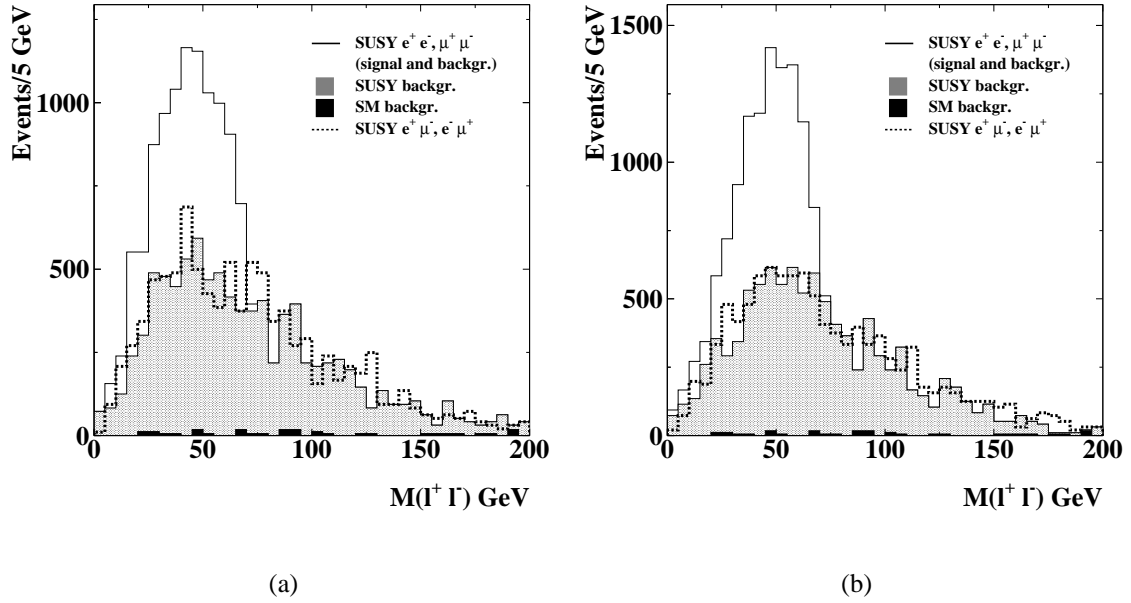Figure 7.17: *Point with $\tan\beta = 2$, $m_0 = 300$ GeV, $\mu > 0$: Dilepton invariant mass distributions for SUSY events containing OS-SF lepton pairs (full histogram), OS-OF lepton pairs (dashed histogram), and for $t\bar{t}$ events containing OS-SF pairs (dashed black histogram), for (a) PYTHIA 6.158 and (b) PYTHIA 6.160.*
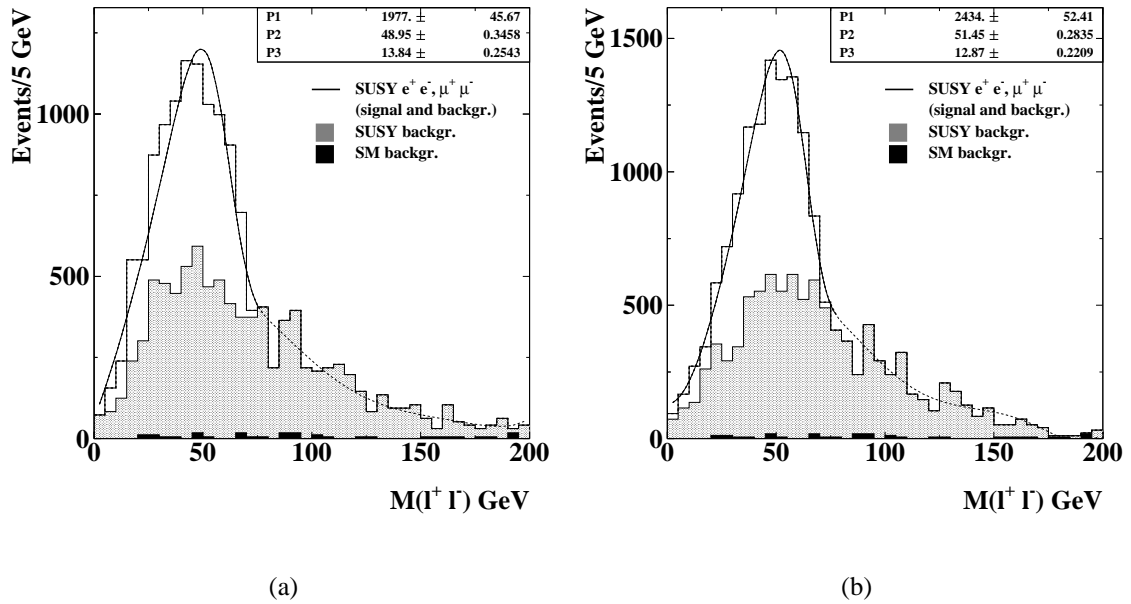

Figure 7.18: *Point with $\tan\beta = 2$, $m_0 = 300$ GeV, $\mu > 0$:The dilepton invariant mass distributions of Figure 7.17 fitted with the function (7.11) for (a) PYTHIA 6.158 and (b) PYTHIA 6.160.*

Finally the $sign(\mu)$ was changed to negative while $tan\beta = 2$. As demonstrated in Figure 7.14d, at the point

$$m_0 = 800\,\text{GeV} \quad m_{1/2} = 200\,\text{GeV} \quad A_0 = 0 \quad tan\beta = 2 \quad \mu < 0$$

our decay channel has vanishing branching ratio, even for smaller values of m_0.

7.6 Summary

A very motivated extension of the Standard Model(SM) is Supersymmetry (SUSY). A gravity-mediated model of SUSY breaking is the Minimal Supergravity model (mSUGRA). In the mSUGRA approach, the MSSM-124 parameter freedom is sharply reduced to 23: 18 of them are the SM parameters and the remaining five are the following: m_0, $m_{1/2}$, A_0, $tan\beta$ and $sign(\mu)$.

The LHC Committee selected in 1996 five mSUGRA points for detailed studies. A sixth point with large $tan\beta$ value was added later by ATLAS.

At point 4 of the mSUGRA parameter space, the next-to lightest neutralino ($\tilde{\chi}_2^0$) has three body decay ($\tilde{\chi}_2^0 \rightarrow \tilde{\chi}_1^0 l^+ l^-$). This decay, gives an interesting signature for point 4, which should allow not only the observation of a SUSY signal, but also the measurement of some parameters of the theory such as the mass difference between the second lightest and the lightest neutralino. Since the sleptons are heavy at this point of mSUGRA, the decay of the $\tilde{\chi}_2^0$ occurs through a virtual Z* with a branching ratio of 5%.

For our studies, SUSY signal events for point 4 were generated using two versions of the Monte Carlo generator PYTHIA (namely PYTHIA 6.158 and 6.160). The supersymmetric extension of PYTHIA (SPYTHIA) that can simulate particle production and decay in mSUGRA (approximately), is implemented already in the above mentioned versions of PYTHIA. In version 6.158, the decays of the sparticles are purely phase space treated, while in the version 6.160 the spin-averaged matrix element is included in these decays, thus taking into account the spin of the neutralinos, as well as the propagator (Z*). Subsequently these produced events passed through the standard fast detector simulation and physics analysis program ATLFAST.

The invariant mass of opposite-sign same-flavour lepton pairs was reconstructed at point 4. These events are required to fulfill stringent transverse missing energy and large jet multiplicity selection criteria in order to suppress the SM background. The specific shape of this dilepton mass distribution can be used as evidence for discovery of SUSY through $\tilde{\chi}_2^0$ production. A comparison between the results of the two versions of PYTHIA not only at point 4 but also at other points of the mSUGRA parameter space , showed that in general it is possible to distinguish between a phase space decay

and a spin-averaged matrix element neutralino decay. The channel $\tilde{\chi}_2^0 \rightarrow \tilde{\chi}_1^0 l^+ l^-$ can be successfully used for SUSY studies in large regions of the parameter space.

Chapter 8

Summary

In order to obtain the required momentum resolution ($\Delta p_T/p_T \approx 1 \times 10^{-4} \times p/\text{GeV}$ for $p_T > 300$ GeV), the ATLAS Muon Spectrometer should fulfill stringent requirements. One of the most crucial mechanical requirements is the fact that the MDT chambers must be constructed with 20 μm mechanical accuracy (r.m.s of the relative distance between the wires of the drift tubes). This demanding precision is an essential ingredient of the MDT concept and needs to be continuously confirmed during the production phase after each chamber assembly.

We have developed a wire calibration method for the ATLAS MDT chambers, that needs no external reference system. The main principal of this method is based on the fact that when a tube wire is displaced, the distribution of the residuals versus the drift distance for tracks which traverse the tube right from its wire is not symmetric with the one for tracks which traverse the tube left from its wire. For the determination of the relative wire positions, the positions of two tubes (one on each multilayer) are kept fixed, while the y coordinates (perpendicular to the tracks' direction) of the twelve surrounding tubes are moved till the distributions of their residuals left and right from their wires become symmetric.

This method was applied for the first time (1998) on a group of 14 tubes (called 'a flower pair') of one of the first full scale prototypes of MDT chambers. The prototype was constructed at MPI, Munich and tested at a high energetic muon test beam at CERN while it was filled with the former ATLAS baseline gas $\text{Ar}/\text{N}_2/\text{CH}_4$ (91/4/5). The relative wire positions (in the direction perpendicular to the muon tracks) for the tubes of this flower pair, were found using our calibration method. The results were compared with those given by the X-ray tomograph (a very precise device placed at CERN, dedicated to scan 10% of the MDT chambers) revealing an accuracy of our method better than 10 μm. The success of these studies was repeated the following year by finding the wire positions of fifty-one tubes of the same prototype chamber; this time the chamber was filled with the new baseline gas Ar/CO_2 (93/7).

Simulation studies of the application of the calibration method along the whole width of a chamber were performed. For a simulated chamber filled with Ar/CO_2 (93/7) and having wire displacements of 20 μm rms in the y direction, muon tracks perpendicular to the chamber using a GEANT based simulation program were produced. The energy of the muons produced was 180 GeV. It should be mentioned that the chamber consists of 70 overlapping flower pairs. By using 25000 tracks per pair, the accuracy of the method in measuring wire displacements in the y direction within each flower pair (local accuracy) is 5 μm. This precision is by a factor two better than the one we obtained using the testbeam data. The reason is that the t_0 parameter was kept equal to zero in the simulation. This parameter expresses the TDC response for a null drift path for each tube. It is different for each channel and is determined by the delays of the signal cables and the front-end electronics. By introducing Gaussian distributed t_0 offsets of an rms of 200 and 300 ps to the drift time spectra of the tubes, the local uncertainty increases to 8 and 9 μm respectively.

By combining the information of the 70 flower pairs we acquired the absolute wire positions within the whole chamber with respect to the first central wires within each multilayer. These absolute wire positions that we obtained in the case where the drift time spectra had Gaussian distributed t_0 offsets of an rms of 200 ps, were measured with an accuracy of 20 μm (global accuracy). Assuming though random and uncorrelated wire displacements, to get the absolute wire positions with respect to the whole chamber, only a small surrounding of each wire is needed. Therefore by slightly modifying the combination procedure of all the 70 flowers the global accuracy improves to 10 μm ($\sigma(t_0) = 200$ ps).

In order to make full use of the potential of this wire calibration method, a total number of more than 10000 tracks per flower pair should be used. This conclusion derived from the statistical studies of the method.

The wire calibration method can be used successfully in determining wire displacements of chambers placed in muon test beams where the muons have an energy of 180GeV or more. The method discussed, can provide a very accurate test of the mechanical accuracy of MDT chambers, being able at the same time to identify and correct the positions of wires that have large displacements.

Another application of the method will be its use in the data analysis of the ATLAS cosmic ray set-ups that have been prepared for the commissioning and calibration of the chamber production at different ATLAS production sites. Finally, this calibration method could offer a possibility for online calibration of the wire positions of the MDT chambers in the final set-up of the ATLAS detector.

The Supersymmetry (SUSY) discovery potential of the ATLAS detector through the production of the next-to lightest neutralino ($\tilde{\chi}_2^0$) was also studied. Within the Min-

imal Supergravity model (mSUGRA) of SUSY, five parameters are used in order to determine the masses and the couplings of the particles: m_0 the common scalar mass, $m_{1/2}$ the common gauginos and Higgsinos mass, A_0 the trilinear Higgs-sfermion-sfermion couplings, $tan\beta$ the ratio of the two Higgs vacuum expectation values and $sign(\mu)$ the sign of the Higgsino mass parameter. At one of the six points of mSUGRA selected by the LHC Committee and the ATLAS Collaboration for detailed studies, namely point 4 characterized by

$$m_0 = 800\,\text{GeV} \quad m_{1/2} = 200\,\text{GeV} \quad A_0 = 0 \quad tan\beta = 10 \quad \mu > 0\,,$$

the $\tilde{\chi}_2^0$ has a three body decay ($\tilde{\chi}_2^0 \rightarrow \tilde{\chi}_1^0 l^+ l^-$) through a virtual Z^* with a branching ratio of 5%.

This decay and its potential SUSY and SM backgrounds were studied. Two versions of the Monte Carlo generator PYTHIA were used: PYTHIA 6.158 and PYTHIA 6.160. In both of these, the supersymmetric extension of PYTHIA (SPYTHIA) that can perform simulations in mSUGRA is implemented. The main difference between the two versions is that although in 6.158 the decays of sparticles are purely phase space treated, in 6.160 the spin-averaged matrix element is included in these decays, thus taking into account the spin of the neutralinos, as well as the propagator (Z^*).

The generated events were passed through the standard fast simulation of the ATLAS Collaboration, ATLFAST. For an integrated luminosity of $3 \cdot 10^4$ pb^{-1}, we reconstructed the invariant mass of opposite-sign same-flavour (OS-SF) lepton pairs at point 4, as well as at three other points of the $(m_0, m_{1/2})$ space (where the mass difference between the two lightest neutralinos is the same as at point 4, $M_{l^+l^-}^{max} = M_{\tilde{\chi}_2^0} - M_{\tilde{\chi}_1^0} \simeq$ 72 GeV). The same procedure was followed for a few more points of the mSUGRA parameter space where we changed also the $tan\beta$ and the $sign(\mu)$. After applying stringent selection criteria in the distributions obtained and comparing them, we concluded that in general it is possible to distinguish between a phase space decay and a spin-averaged matrix element neutralino decay. The channel $\tilde{\chi}_2^0 \rightarrow \tilde{\chi}_1^0 l^+ l^-$ can be successfully used for SUSY studies in large regions of the parameter space.

Bibliography

[ALE99a] M. Aleksa: *Performance of the ATLAS Muon Spectrometer,* PhD Thesis, CERN, 1999.

[ALE99b] M. Aleksa: *Rate Effects in High-Resolution Drift Chambers,* CERN-EP/99-101, 1999, NIM A 446/3 (2000), pp. 435-443.

[ALI95] ALICE Collaboration: *ALICE Technical Proposal,* CERN/LHCC/95-71, 1995.

[AMA91] U. Amaldi, W. de Boer and H. Fürstenau: Phys. Lett. **B260** (1991) 447.

[ATL94] ATLAS Collaboration: *ATLAS Technical Proposal,* CERN/LHCC/94-43, 1994.

[ATL97] ATLAS Muon Collaboration: *ATLAS Technical Design Report,* CERN/LHCC/97-22, 1997.

[ATLb97] ATLAS Collaboration: *Barrel Toroid Technical Design Report,* CERN/LHCC/97-19, 1997.

[ATLc97] ATLAS Collaboration: *Central Solenoid Technical Design Report,* CERN/LHCC/97-21, 1997.

[ATLcl96] ATLAS Collaboration: *Calorimeter Performance Technical Design Report,* CERN/LHCC/96-40, 1996.

[ATLe97] ATLAS Collaboration: *End-Cap Toroids Technical Design Report,* CERN/LHCC/97-20, 1997.

[ATLi97a] ATLAS Collaboration: *Inner Detector Technical Design Report, Volume 1* CERN/LHCC/97-16, 1997.

[ATLi97b] ATLAS Collaboration: *Inner Detector Technical Design Report, Volume 2* CERN/LHCC/97-17, 1997.

[ATLl96] ATLAS Collaboration: *Liquid Argon Calorimeter Technical Design Report,* CERN/LHCC/96-41, 1996.

[ATLm97] ATLAS Collaboration: *Magnet System Technical Design Report,* CERN/LHCC/97-18, 1997.

[ATLp98] ATLAS Collaboration: *Pixel Detector Technical Design Report,* CERN/LHCC/98-13, 1998.

[ATLt96] ATLAS Collaboration: *Tile Calorimeter Technical Design Report,* CERN/LHCC/96-42, 1996.

[ATL98] E. Richter-Was et. al.: *ATLFAST 2.0: a fast simulation package for ATLAS,* Atlas Note ATL-PHYS-98-131, CERN, 1998.

[ATL99] ATLAS Collaboration: *ATLAS Detector and Physics Performance Technical Design Report,* CERN/LHCC/99-15, 1999.

[BAE95] H.Baer et. al.: Phys. Rev. **D52** (1995) 2746.

[BAR94] S. Baranov et al.: *Gamma Sensitivity of Pressurized Drift Tubes,* ATLAS Note ATL-MUON-94-036, CERN, 1994.

[BAT98] R. Battiston: *The Alpha Magnetic Spectrometer (AMS): search for antimatter and dark matter on the International Space Station,* Nucl.Phys.Proc.Suppl.65:19-26, 1998.

[BER98] J. Berbiers et al.: Nucl. Instrum. Methods **A419** (1998) 342-350.

[BLU94] W. Blum, L. Rolandi: *Particle Detection with Drift Chambers,* Springer Verlag, 1993.

[BNL73] *Common base preamplifier IO354-2 ans shaping amplifier IO532-01,* Instrumentation Division, Brookhaven National Laboratory, Upton(NY), 1973.

[BOS98] V. Bartheld et al.: *Construction of the Full-Scale Prototype of a BOS MDT chamber,* ATLAS Note ATL-MUON-98-256, CERN, 1998.

[CHE93] A. Cheplakov et al.: *Muon Rates in ATLAS,* ATLAS Note ATL-MUON-93-21, CERN, 1993.

[CHL93] G.A. Chelkov et al.: *Investigation of spectral efficiency of pressurized drift tubes for detection of neutrons in the energy range between 5 eV and 200 keV,* ATLAS Note ATL-MUON-93-31, CERN, 1993.

[CHO98] S. Chouridou et al.: *Protvino Drift Tubes for BML-98. Test Results,* ATLAS Note ATL-MUON-98-247, CERN, 1998.

[CHO00] S. Chouridou et al.: *Construction and Test of MDT Chambers for the ATLAS Muon Spectrometer,* Nucl. Instrum. Methods **A461** (2001) 17-20, ATLAS Note ATL-COM-MUON-2000-008, CERN, 2000.

[CMS94] CMS Collaboration: *CMS Technical Proposal,* CERN/LHCC/94-38, 1994.

[COL67] S. Coleman and J. Mandula: Phys. Rev. **159** (1967) 1251.

[CRE97] P. Creti et al.: *Testbeam results from the Calypso MDT chamber,* ATLAS Note ATL-MUON-97-196, CERN, 1997.

[DEI98] M.Deile et al.: *MDT Track Fitting with the Maximum Likelihood Method,* ATLAS MUON-98-240, CERN, 1998.

[DEI99] M.Deile et al.: *ODYSSEUS: a Silicon Telescope for Test Beam Experiments,* ATLAS COM-MUON-99-015, CERN, 1999.

[DEI00] M.Deile: *Optimization and calibration of the Drift-Tube Chambers for the ATLAS Muon Spectrometer,* PhD thesis, Munich, 2000.

[DEN90] D. Denegri: *Standard Model Physics at the LHC (pp Collisions),* published in [JAR90], Vol.I, 56-117, 1990.

[DRA97] D. Drakoulakos et al.: *The High-Precision X-Ray Tomograph for quality control of the ATLAS MDT Muon Spectrometer,* CERN-OPEN-97-023, 1997.

[ELL83] J. Ellis, D.V. Nanopoulos and K. Tamvakis: Phys. Lett. **B121** (1983) 123.

[ELL91] J. Ellis, S. Kelley and D. V. Nanopoulos: Phys. Lett. **B260** (1991) 131.

[FAB97] F. Gianotti: *Precision SUSY measurements with ATLAS: SUGRA 'Point 4',* ATLAS Note ATL-PHYS-97-110, CERN, 1997.

[GEA93] *GEANT, CERN Program Library Long Writeup,* W5013, 1993.

[GSC00] E. Gschwendtner: *Benchmarking the Particle Background in the LHC Experiments,* PhD thesis, CERN, 2000.

[HES98] N.P. Hessey: *The Precision Drift Chambers for the ATLAS Muon Spectrometer,* Nucl. Instrum. Methods **A419** (1998) 326-330.

[IBA82] L. Ibanez: Phys.Lett. **B118** (1982) 73.

[INO82] K. Inoue et. al.: Prog. Theor. Phys. 68 (1982) 927.

[JAR90] G. Jarlskog and D. Rein (editors): *Proceedings of the Large Hadron Collider Workshop,* CERN/90-10, 1990.

[KEK] KEK, National Laboratory for High Energy Physics, Japan

[KOR98] O. Kortner: Private Communication.

[KOR00] O. Kortner: *MTGEANT-3, the previous version of MTGEANT-4- The Mu-nich Test-Stand Simulation Programme,* ATLAS Note ATL-MUON-2000-021, CERN, 2000.

[KRO00] H. Kroha et al.: *Analysis of the X-Ray Tomograph Data of the BOS MDT prototype Chamber,* ATLAS Note ATL-MUON-2000-015, CERN, 2000.

[LAN81] P. Langacker: Phys. Rep. **72** (1981) 185.

[LEP99] ALEPH 99-007 CONF-99-003, DELPHI 99-8 CONF-208, L3 Notes 2382 and 2383, OPAL PN382.

[LEP01] The LEP Higgs Working Group: ALEPH 2001-66, DELPHI 2001-113, L3 Note 2699, OPAL PN479, LHWG Note/2001-03.

[LHCb98] LHCB Collaboration: *LHCb Technical Proposal,* CERN/LHCC/98-4, 1998.

[MRE01] S. Mrenna: Private communication.

[OHM94] P. Ohmann, V. Barger and M.S. Berger: Phys. Rev. **D49** (1994) 4908.

[PDG00] D.E. Groom et al.: *Particle Data Group,* Eur. Phys. J. **C15** (2000) 1.

[PRI88] J.R. Primack et al.: Ann.Rev.Nucl.Part.Sci. **38** (1988) 751.

[RAU01] F. Rauscher: *Test von Driftkammern mit kosmischen Myonen: Bau der ersten Ausbaustufe des Teleskops und Untersuchung seiner Leistungsfaehigkeit,* Diploma thesis, Munich, 2001.

[RIE97a] W. Riegler: *MDT Efficiency, Double Track Separation,* ATLAS MUON-97-173, CERN, 1997.

[RIE97] W. Riegler: *Limits to Drift Chamber Resolution,* PhD thesis, CERN, 1997.

[RIE99] W. Riegler et al.: *Resolution Limits of Drift Tubes,* CERN-EP/99-99, 1999, NIM A 443/1 (2000), pp.156-163.

[SAU77] F. Sauli: *Principles of operation of mutliwire proportional and drift cham-bers,* CERN 77-09, 1977.

[SM61] S. Glashow: Nucl.Phys. **22** (1961) 579;
        S. Weinberg: Phys.Rev.Lett. **19** (1967) 1264;
        H.D. Politzer: Phys.Rev.Lett. **30** (1973) 1346.

[SMI97] I. Smirnov: *HEED, program to compute energy loss of fast particles in gases,* Version 1.01, CERN, 1997.

[SPE98] M. Spegel: *On the Lifetime of Proportional Counters,* PhD thesis, CERN, 1998.

[SPY96] S. Mrenna: *SPYTHIA: A Supersymmetric Extension of PYTHIA 5.7,* ANL-HEP-PR-96-63, 1996.

[SUS71] P. Ramond: Phys.Rev. **D3** (1971) 2415;
J. Wess and B. Zumino: Nucl. Phys. **B78** (1974) 39;
H. P. Nilles: Phys. Rep. **110** (1984) 1;
H.E. Haber and G.L. Kane: Phys. Rep. **117** (1985) 75.

[VEN95] S. Veneziano et al.: Nucl. Instrum. Methods **A367** (1995) 418-421.

[VIE96] G. Viehhauser: *Detector Physics of the ATLAS precision muon chambers,* Ph.D thesis, Technical University of Vienna, 1996.

Acknowledgements

First of all I would like to thank Prof. Dorothee Schaile for her continuous guidance and support for my work. I can still feel the joy I experienced the moment she informed me that she will support my application for a Marie Curie fellowship. Her determination and strength have always been an inspiration to me. I thank her also for the wonderful rafting excursions she organized for our group!

I am very grateful to Prof. Chris Fabjan, maybe the first person who encouraged me so much to follow a career in particle physics. I thank him for having always the time to listen to my usual report for my work every time I was at CERN and discuss with me my results. His precious advice guided me many times and he always gave me the feeling that working for particle physics is one of the most beautiful things in the world.

I would also like to thank my teacher and a very good friend; Stefan Schael. He not only taught me most of the things I know in programming and data analysis but he was always there to encourage me and help me to find solutions in the problems of my work. Working with him it has always been a pleasure.

Many thanks go to Michael Treichel who gave me the idea to make a PhD in Munich and supported me in difficult moments.

I am grateful to Raimund Ströhmer and Thomas Trefzger for their wonderful data analysis ideas, for introducing me in the particle physics simulation techniques and for their help in overcoming difficulties with my analysis. I am also thankful to Prof. Arnold Staude, Oliver Kortner, Mario Deile, Günter Duckeck and Madjid Boutemeur for fruitful discussions and exchanging ideas. It was a pleasure working with Nigel Hessey during the test beam periods and learning from him so many hardware techniques. He always managed to keep me calmed even when our BOS chamber was 'sick'. Many thanks to Andrei Ostapchuk for his help and the time he spared to discuss with me my results.

It would be an omission if I wouldn't thank Mrs. Herta Franz, our secretary. She would always be there to help me and even make herself many phone calls for bureaucratic matters on behalf of me as my German were never that good. Many thanks go also to Mr. Otto Schaile for his quick assistance in computing problems.

I would like to thank Meta Binder with whom I shared the office. We became very good friends and we did not only spend hours of talking about physics but also had great time while drinking wine and forgetting a bit the every day problems of the

work. Many thanks to Axel Leins for the 'thousands' options for Linux commands that he showed me.

I would like to thank my Austrian friends (the Austrian gang as I call them), Edda, Helmut, Petra, Christoph, Axl, Werner and Martin. Every time I was at CERN they kept me a great company, they made me laugh and I never felt alone there. With the last two of them I had also 'business discussions'(about tubes and wires of course) and I am thankful to them for that.

I would like at this point to thank some more friends who supported me during the years of my thesis. They made me believe in myself and were always there when I needed them, even if it was for only a glass of beer! A big Thank you then to Andrea, Christina, Martina, Marcella, Nils, Kostas, Babis, Norman, Stavros, Christos, Sofia, Orly and Dimitris.

I am grateful to the European Commission which gave me this Marie Curie Grant and I was able to make my thesis. Many thanks to my friends from the Marie Curie Association for the wonderful time we had during our regular Stammtisch.

I would like to thank with all my heart my family; my parents, my brother, my sister and my sister-in-law. Without their continuous encouragement, support and love I could never have made it. My mother who taught me to have confidence in myself spend a fortune in telephone bills and always gave me courage to continue my work in which she was always interested. My father would love to read this little book I wrote but unfortunately he left recently from this world. I still remember the endless discussions I had with him about physics. I have to admit that I agree with him and not with Einstein: there is finally a speed faster than this of the light; the speed of the mind.

Finally, I thank God for giving me the chance to study the mysteries of His wonderful world.

Curriculum Vitae

24 May 1971	Born in Serres, Greece.
09/77 - 06/83	Primary School in Thessaloniki, Greece.
09/83 - 06/89	High School in Thessaloniki.
June 1987	First Certificate in English of the University of Cambridge.
10/90 - 10/96	Study of Physics at the Aristotle University of Thessaloniki. Diploma thesis on ' *Studies of the ATLAS MDTs Properties for Different Gas-mixtures and Effect of the Operating Parameters on their performance'*.
June 1993	Certificate of Proficiency in English of the University of Cambridge.
06/95 - 09/95	Summer Student at CERN.
04/96 - 06/96	Erasmus student at the University of Geneva, Switzerland. Work carried out at CERN on the prototype of the ATLAS X-ray tomograph.
06/97 - 12/97	Max Planck Institute for Physics in Munich, Germany.
1/98 - 1/02	Doctoral thesis at the Ludwig Maximilians University (LMU) in Munich, supported by a Marie Curie Fellowship of the European Commission (contract N^0 ERBFMBICT 972519).
01/98 - 06/98	German courses in Munich.
September 1999	CERN School of Computing in Stare Jablonki, Poland.
July 2000	5th Workshop of Marie Curie Fellows at the University of Bonn, organized by the European Commission.
August 2000	PSI Summer School on Phenomenology of Gauge Interactions, in Zuoz, Switzerland.